NOTICE

The quality of this microform is heavily dependent upon the quality of the original thesis submitted for microfilming. Every effort has been made to ensure the highest quality of reproduction possible.

If pages are missing, contact the university which granted the degree.

Some pages may have indistinct print especially if the original pages were typed with a poor typewriter ribbon or if the university sent us an inferior photocopy.

Reproduction in full or in part of this microform is governed by the Canadian Copyright Act, R.S.C. 1970, c. C-30, and subsequent amendments.

AVIS

La qualité de cette microforme dépend grandement de la qualité de la thèse soumise au microfilmage. Nous avons tout fait pour assurer une qualité supérieure de reproduction.

S'il manque des pages, veuillez communiquer avec l'université qui a conféré le grade.

La qualité d'impression de certaines pages peut laisser à désirer, surtout si les pages originales ont été dactylographiées à l'aide d'un ruban usé ou si l'université nous a fait parvenir une photocopie de qualité inférieure.

La reproduction, même partielle, de cette microforme est soumise à la Loi canadienne sur le droit d'auteur, SRC 1970, c. C-30, et ses amendements subséquents.

ISBN 0-315-56384-2

EXPERIMENTS
IN
LOW REYNOLDS NUMBER FLOWS

by

BRAHIM CHEBBI

A thesis
presented to the University of Ottawa
on January, 1989
in partial fulfillment of the
requirement for the degrec of
MASTER of APPLIED SCIENCE
in
MECHANICAL ENGINEERING

UNIVERSITÉ D'OTTAWA
UNIVERSITY OF OTTAWA

Abstract

Abstract

An experimental facility and instrumentation for low Reynolds number flows have been developed.

Flow visualization results and measurements of velocity components inside and above asymmetric cavities using an LDA system are presented. A recirculation region is present even at small Reynolds numbers. The size of the vortex and the distance between its center and the vertical wall of the cavity increases when increasing the Reynolds number. Increasing the angle of attack at low Reynolds number causes a slight increase of the recirculation vortex size.

The variation of the pressure coefficient, determined by pitot-static tubes for the low range of Reynolds numbers is investigated. The results agree reasonably well with theoretically determined values for cylinders.

The disturbance of the flow by the pitot tube presence is also investigated by measuring the velocity profiles around the pitot tube.

Acknowledgements

I express gratitude and appreciation to Professor S. Tavoularis for his motivating guidance, encouragement and permanent availability for discussions. His quick and careful editing of the text helped immensely in the compilation of this thesis.

The financial support, provided by the Scientific Mission of Tunisia and the Natural Sciences and Engineering Research council of Canada, is greatly appreciated. Thanks are due to the machine shop staff for providing assistance when needed. I would also like to thank my colleagues Sadok Guellouz and Gordon Holloway for their valuable discussions.

To my family, friends and colleagues I am greatly indebted for the support they have given me during my research.

Contents

List of Tables

List of Plates

List of Figures

Nomenclature

Nomenclature

a	calibration factor
C_D	drag coefficient
C_L	lift coefficient
C_p	pressure coefficient
d	particle diameter
d_f	distance between two fringes
d_m	diameter of focussed laser beam
D	diameter of laser beam defined to $\frac{1}{e^2}$ of maximum intensity
D_e	external diameter of pitot tube
f	focal length of lens
f_D	Doppler frequency
f_s	frequency shift
Δf	frequency bandwidth
h	Plank constant
h_m	height of measuring volume
H_V	height of center of vortex wrt to inside corner of cavity
l_m	length of measuring volume
L	length scale, also used as a characteristic distance for flow reattachment

L_V	distance from center of vortex to vertical wall of cavity
m	index of refraction
n	number of fringes
P	pressure
P_0	total pressure
P_s	static pressure
r_0	particle radius
Re	Reynolds number
SNR	signal to noise ratio
t	time, also used for wall thickness in section 5.4
X_S	scattering cross section of particle
y	distance from inside wall of test section
U	velocity component on plane formed by the two laser beams
U_F	fluid velocity
U_P	particle velocity
U_s	velocity of fringes
V	total velocity
V_T	terminal velocity of particles
W_0	laser power
W_S	power of scattered light

Greek letters

α	angle of attack
Γ	solid angle aperture of receiving optics
Δ	beam separation
θ	angle of intersection of the two laser beams

λ	laser wavelength
Λ	ultrasonic wavelength
μ	dynamic viscosity
ν	kinematic viscosity
ρ	fluid density
ρ_P	particle density
τ	time constant
υ	optical frequency o laser
ϕ_B	Bragg angle
ψ	streamfunction
Ψ	nondimensional streamfunction
ω	vorticity
Ω	nondimensional vorticity

Suffixes

$(\ )^*$	nondimensional quantities
$(\ )_\infty$	quantities evaluated at free stream

Chapter 1

Introduction

1.1 Motivation for the Present Investigation

Flows at low Reynolds numbers have been investigated by a large number of researchers due to their frequent occurrence in biological and industrial systems. As O'Neil (1981) has stated, "the motion of small particles in viscous medium impinges on our world and our lives to such an extent that it would be no exaggeration to say that the phenomenon is ubiquitous ...".

Red cell motion in capillary blood flow, suspension and polymer rheology, continuum mechanics and diffusive transport processes in suspensions of Brownian particles, distortion of flows in tubes and ducts caused by boundary irregularities and swimming of microscopic organisms are but a few examples of phenomena involving low Reynolds number flows.

The theory of very slow motion of particles in viscous fluid was founded by Stokes (1851) who derived the well-known formula for the drag force acting on a rigid sphere translating with a uniform velocity through quiescent fluid. Although the mathematical formulation of low Reynolds number flows is relatively well established, flow patterns revealed by recent experimental and analytical studies can be rather complicated and often beyond intuitive explanation. For complex

geometries, experimentation appears to remain more reliable than direct computation. In any case, computations should be tested versus experimental results, at least with respect to some of their crucial features.

On the other hand, the development of high quality experimental facilities and instrumentation that are suitable for low Reynolds number flows is more difficult than it may appear at first glance, because the required length scales, velocities and/or fluid viscosities are outside the ranges encountered in most applications. The present thesis explains, at first, the design and testing of an apparatus that can be used for generating steady and periodic flows past various objects in the low Reynolds number range; the development of suitable flow visualization procedures as well as of low velocity and pressure measurement techniques was also a necessary part of this study.

Subsequently, the research focuses on two particular problems involving low Reynolds number flows : a) flow past asymmetric cavities on a surface b) the performance of pressure tubes in the low Reynolds number range.

The study of flows over asymmetric cavities was motivated by Nachtigall's (1967) observation that scales on certain butterfly and moth upper wing surfaces appear aerodynamically advantageous, since their removal results in decrease of the lift without any significant change of the drag. Another motive of studying flow past cavities is that they usually occur as unwanted drag, increasing gaps between segments of aircraft skin as well as in slots between moveable parts of wings and control surfaces. Uncovered cavities on vehicles necessary to house optical or other instruments, slotted walls used in transonic wind tunnels, cavities of ship hulls and static pressure measurement slots (where information about the internal flow pattern is needed to determine the hole pressure error) provide other

examples of applications requiring the study of cavity flows.

Pressure tubes, such as pitot (or total head), static and pitot-static tubes, are used extensively as measuring instruments, due to their simplicity of construction and ease of operation. Bernoulli's equation is normally used in incompressible flows to determine the flow velocity from the impact pressure. However, in low Reynolds number flows, this approximation is no longer valid because the viscosity effects become significant. It is also expected that the flow velocity and the impact pressure are strongly dependent on the geometrical shape and dimensions of the tube. Tube readings may be significantly influenced by viscous effects in the following situations: wake surveys behind compressor and turbine cascades using very small pitot tubes; velocity profile determination in boundary layers using very small flattened pitot tubes close to the wall; velocity measurements in very narrow channels and slits; impact pressure measurements in very viscous liquids (e.g. in blood streams with small pitot tubes); and impact pressures in air flow at hypersonic speeds, where the air density and consequently the Reynolds number is very small.

1.2 Objectives

The first objective of this thesis was to put in function the liquid channel, whose early form was designed by Tittley (1985), and to develop and test the necessary equipment, including a Laser Doppler Anemometer system with optical and electronic frequency shifting, in order to create a reliable facility for experimental research in low Reynolds number flows. The second objective was to contribute to the study of the specific problems of flow past asymmetric cavities and pressure tubes in the low Reynolds number regime.

Previous investigations on flow over cavities do not report direct measurements of velocities inside the cavities. It is intended to obtain such results with the present facility. The use of Laser Doppler Anemometry (LDA) presents the advantage of not disturbing the flow and the ability to measure very low velocity and reversing flow. These results are intended to be used to explain the aerodynamic advantage of the presence of scales on the butterfly wing. The data can also be used to check the accuracy of the different methods of calculation of low Reynolds number flows. The results obtained from LDA along with flow visualization will also be used to study separation and reattachment of flow in asymmetric cavities.

The disturbance of the flow due to the insertion of a Pitot tube will be studied by measuring the velocity field around the tube. A comparison of the velocity measured by the Laser Doppler Anemometer and the one evaluated using the Pitot tube reading will provide directly the error of Pitot tubes in low Reynolds number flows. Variation of the pressure coefficient with the Reynolds number will also be studied.

It is anticipated that the present study will lead to further use of the facility in research involving low Reynolds number flows in biological and industrial systems. Another possible use could be in simulations of the viscous sublayer of turbulent boudary layers, especially in connection with drag reduction devices.

Chapter 2

Mathematical Description of Low Reynolds Number Flows

2.1 Governing Equations

Two different types of motion can be identified as low Reynolds number flows : creeping motions, where the velocity is very small or the kinematic viscosity of the fluid is very high, and the motion of very small objects, such as particles in Brownian motion, minute swimming organisms and electrically charged particles in colloidal suspensions.

The general set of equations that describe the motion of a Newtonian, incompressible fluid include the continuity equation

$$\nabla.\vec{V} = 0 \tag{2.1}$$

and the momentum (Navier-Stokes) equation

$$\frac{D\vec{V}}{Dt} = -\frac{1}{\rho}\nabla P + \nu\nabla^2\vec{V} \tag{2.2}$$

where $\vec{V}$ is the velocity vector, $\frac{D}{Dt}$ is the total acceleration, P is the pressure, ρ is the density and ν is the kinematic viscosity of the fluid. For a convenient order of magnitude analysis, it is customary to nondimensionalize all terms in the

above equation by using some representative velocity scale, U, length scale, L, and pressure Po. In terms of the dimensionless variables $\vec{V}^* = \frac{\vec{V}}{U}$, $t^* = \frac{Ut}{L}$, $\vec{X}^* = \frac{\vec{X}}{L}$ and $P^* = \frac{P-Po}{\rho U^2}$, equations (2.1) and (2.2) can be rewritten as

$$\nabla^* . \vec{V}^* = 0 \tag{2.3}$$

$$\frac{D\vec{V}^*}{Dt} = -\nabla^* P^* + \frac{1}{Re}\nabla^{*2}\vec{V}^* \tag{2.4}$$

where Re is the Reynolds number $\frac{\rho VL}{\mu}$. For a steady flow, if the Reynolds number is much smaller than unity, then the last term on the r.h.s. of equation (2.4), representing the viscous stress, becomes much larger than the l.h.s. which represents inertial forces per unit mass. As Re vanishes, the l.h.s. of equations (2.4) and (2.2) can be neglected and these equations are reduced to the simpler forms

$$\nabla P = \mu \nabla^2 \vec{V} \tag{2.5}$$

$$\nabla^* P^* = \frac{1}{Re}\nabla^{*2}\vec{V}^* \tag{2.6}$$

Equation (2.5) is usually known as the Stokes equation. The Stokes equation is free of inertial effects. By taking the divergence and the curl of equation (2.5), it is possible to show using vector calculus that

$$\nabla^2 P = 0 \tag{2.7}$$

$$\nabla^2 \vec{\omega} = 0 \tag{2.8}$$

Where $\vec{\omega} = \nabla \times \vec{V}$ is the vorticity vector. Equations (2.7) and (2.8) imply that P and $\vec{\omega}$ are harmonic functions in Stokes flow.

In a two-dimensional flow parallel to the (x,y) plane, the stream function ψ is defined as $u = \frac{\partial \psi}{\partial y}$, $v = -\frac{\partial \psi}{\partial x}$, where u and v are the velocity components in the

cartesian coordinates x and y. It can be shown that the vorticity, which reduces in this case to a single component, $\omega_z = \frac{\partial v}{\partial x} - \frac{\partial u}{\partial y}$, relates to ψ by

$$\omega = -\nabla^2 \psi \tag{2.9}$$

Substituting (2.9) into (2.8) one gets an equation for low Reynolds numbers two-dimensional flows as

$$\nabla^4 \psi = 0 \tag{2.10}$$

From equation (2.8) it can be seen that for a given boundary the streamlines would be the same if the flow direction is reversed, since a change in sign for the velocity does not affect the Stokes equation.

When the Reynolds number is small but not vanishing, Oseen proposed to simplify the Navier-Stokes equation into a form in which inertial terms appear as convection by the free stream velocity. For a steady flow the Oseen's equations are

$$\nabla . \vec{V} = 0 \tag{2.11}$$

$$U_\infty (\frac{\partial \vec{V}}{\partial X}) = -\frac{\nabla P}{\rho} - \nu \nabla^2 \vec{V} \tag{2.12}$$

2.2 Analytical and Numerical Solutions for Low Reynolds Number Flow

In solving the system of equations (2.7) and (2.8), Lamb (1932) showed that if

$$P = \Sigma P_n \tag{2.13}$$

where n can be any positive or negative integer except for -1, then the velocity may be written as

$$\vec{V} = \Sigma [\nabla \phi_{n+1} + \vec{r} \times \nabla \chi_n + \frac{1}{\mu} \frac{1}{2n(n+1)} \times ((n+2) r^2 \nabla P_{n-1} - 2(n-1) P_{n-1} \vec{r})] \tag{2.14}$$

where ϕ_n and χ_n are harmonic functions.

Stokes solved equation (2.9) for the flow past a sphere of radius a in spherical coordinates (r, θ, λ). In terms of the Stokes stream function, ψ_s,which for axisymmetric flows is defined as

$$v_r = \frac{1}{r^2 \sin\theta} \frac{\partial \psi_s}{\partial \theta} \qquad v_\theta = -\frac{1}{r \sin\theta} \frac{\partial \psi_s}{\partial r}$$

equation (2.9) reduces to

$$D^4 \psi_s = 0 \tag{2.15}$$

Where D^2 represents the operator $\frac{\partial^2}{\partial r^2} + \frac{(1-c^2)}{r^2} \frac{\partial^2}{\partial c^2}$, with $c = \cos\theta$. The Stokes stream function which satisfies this equation is

$$\psi_s = \frac{1}{2} V a^2 \sin^2\theta (\frac{r}{a} - 1)^2 (1 + \frac{1}{2}\frac{a}{r}) \tag{2.16}$$

where $\theta = 0$ is defined at the forward stagnation point. Since ψ is symmetrical about the plane $\theta = \frac{\pi}{2}$, the streamline pattern is symmetrical about an axial plane normal to the free stream and therefore shows no wake. This is due to the fact that, in Stokes solution, the inertia terms were discarded. The pressure can be shown to be

$$P = P_\infty - \frac{3}{2} \mu V a r^{-2} \cos\theta \tag{2.17}$$

where P_∞ is the free stream pressure, assumed to be uniform. From this equation it can be seen that the stress on the surface of the sphere has a streamwise component, which when integrated provides a total viscous drag on the sphere equal to $6\pi\mu V a$. It follows that the drag coefficient is given by

$$C_D = \frac{24}{Re} \tag{2.18}$$

The above equation agrees well with experimental results for $Re < 1$ but underestimates the drag as Re approaches and exceeds 1.

Equation (2.10) was also solved for the flow past a circular cylinder of radius a in plane polar coordinates (r, θ) (see Rosenhead, 1963). The streamfunction which satisfies this equation is given by

$$\psi = A \sin\theta[(\frac{r}{a}) \ln(\frac{r}{a}) - \frac{1}{2}\frac{r}{a} + \frac{1}{2}\frac{a}{r}] \tag{2.19}$$

where A is a constant to be determined by the flow conditions. Then the drag can be shown to be

$$F - D = 4\pi\mu\frac{A}{a} \tag{2.20}$$

Taylor (1960) solved equation (2.10) using a series expansion of the form $r^n f(\theta)$. For the case n=1 this solution represents the flow of a viscous fluid pushed by a scraper on a flat sheet and can be expressed as

$$\psi = r(A\cos\theta + B\sin\theta + C\theta\sin\theta + D\theta\sin\theta) \tag{2.21}$$

where the constants A,B,C and D are to be determined by the boundary conditions.

Amara and Destuynder (1981) developed a numerical method for solving the biharmonic equation

$$\begin{cases} \nabla^4 u = f & \text{on } \omega \\ u = \frac{\partial u}{\partial x} & \text{on } \gamma \end{cases} \tag{2.22}$$

where ω is an open set of $\Re^2$ with a boundary γ. They considered a perturbed formulation of (2.22), and ended up with a linear matricial equation which can be solved for U (U being a matricial representation of u).

Moffat (1963) solved equation (2.10) in polar coordinates for the flow near a sharp corner. He imposed different boundary conditions on the two planes forming the corner and expressed the solutions in the form

$\psi = Ar^\lambda f_\lambda(\theta)$, where λ is a real or complex number and A is a nondimensional constant. It was shown by Moffat's analysis that when the angle of the corner is

less than 146 deg in value, the flow very close to the corner consists of a sequence of counter rotating eddies of decreasing size and rapidly decreasing intensity. The relative dimensions and intensities of successive eddies were determined.

Burggraf(1965) investigated the viscous structure of a separated eddy analytically and numerically. The analytical solution, obtained for an eddy bounded by a circular streamline, was based on a linearized model. He expressed the Navier-Stokes equation in terms of the stream function and the vorticity in cylindrical coordinates, considering the nondimensional variables $r^* = \frac{r}{a}$, $u^* = \frac{u}{\Omega a}$, $\psi^* = \frac{\psi}{\Omega a^2}$ and $\omega^* = \frac{\omega}{\Omega}$, where a is the radius of the circle and Ω is a characteristic angular velocity on the boundary surface. Then the nondimensional Navier-Stokes equations are reduced to

$$\nabla^2 \psi^* = -\omega^* \tag{2.23}$$

$$\nabla^2 \omega^* = \frac{Re}{r^*}\left[\frac{\partial \psi^*}{\partial \theta}\frac{\omega^*}{\partial r^*} - \frac{\partial \omega^*}{\partial r^*}\frac{\partial \omega^*}{\partial \theta}\right] \tag{2.24}$$

where Re is the Reynolds number, equal to $\frac{\Omega a^2}{\mu}$. The basic flow is defined by $u_\theta^* = r^*$, $u_r^* = 0$, $\psi^* = \frac{1}{2}(1 - r^{*2})$, $\omega^* = 2$. The Navier-Stokes equation was simplified to obtain the simple equation

$$\nabla^2 \omega^* = Re\frac{\partial \omega^*}{\partial \theta} \tag{2.25}$$

The above equation was solved using the separation of variables method for the general case of any Reynolds number and the obtained solutions were expressed in terms of a Fourier series. To obtain the solution for small Reynolds numbers, Burggraf took the limit of the obtained expressions for ψ and ω as $Re \to 0$. The so obtained solutions are

$$\psi^* = \frac{1 - r^{*2}}{2}\left(A_0 + \sum_{n=1}^{\infty} A_n r^{*n} e^{in\theta}\right) \tag{2.26}$$

$$\omega^* = 2(A_0 + \sum_{n=1}^{\infty}(n+1)A_n r^{*n} e^{in\theta}) \tag{2.27}$$

The change of the eddy structure as the Reynolds number increased was in agreement with previous investigations such as the work done by Batchelor (1954). It was shown that a completely viscous eddy, which is present at low Reynolds numbers, develops to an inviscid rotational core at high Reynolds numbers.

A numerical solution of the full Navier-Stokes equation for a square cavity was also carried out by Burggraf (1965). He solved the Navier-Stokes equation written in terms of the vorticity and the stream function, using a rectangular mesh. X and Y are the coordinates normalized with respect to the width of the cavity, L, ($X = x/L$, $Y = y/L$), Ψ and Ω are nondimensional stream function and vorticity ($\Psi = \frac{\psi}{LV}$, and $\Omega = \frac{\omega L}{V}$). Then the Navier-Stokes equations are expressed as

$$\nabla^2\Psi = -\Omega \tag{2.28}$$

$$\nabla^2\Omega = R[\frac{\partial\Psi}{\partial Y}\frac{\partial\Omega}{\partial X} - \frac{\partial\Psi}{\partial X}\frac{\partial\Omega}{\partial Y}] \tag{2.29}$$

The solutions were carried out by a relaxation procedure on a digital computer. At higher values of R, an inviscid core develops, but secondary eddies are present in the bottom corners of the square at all R.

Shen and Floryan (1985) analyzed numerically low Reynolds number flow over cavities. They approximated (2.27) and (2.28) using the central difference method. At the vicinity of the corners the expected sequence of eddies (Moffat, 1963) could not be predicted by the central difference method, so that for the two grid points next to each corner the local solutions presented by Gupta et al. (1981) were used. These solutions express Ψ and Ω in terms of power series in Re

$$\Psi = \Psi^{(0)} + R\Psi^{(1)} + R^2\Psi^{(2)} + ... \tag{2.30}$$

$$\Omega = \Omega^{(0)} + R\Omega^{(1)} + R^2\Omega^{(2)} + ... \tag{2.31}$$

Oseen (1910) used Green's theorem to solve his equation for the velocity and pressure at any point in the fluid in terms of the values of these quantities on the surface bounding the fluid, while Imai(1954) used complex variables and conformal mapping to obtain solutions of Oseen's equations for plane flow.

Floryan (1983) developed a conformal-mapping based coordinate generation method for channel flows. This method was successfully used by Tavoularis, Goldman and Floryan (1985) for analyzing low Reynolds number flows on asymmetric cavities.

An important analysis initiated by Kaplun (1957) led to the improvement of low Reynolds number theory . His method consisted of the use of inner and outer expansions. in which the Stokes flow is in the inner expansion and it is matched to the Oseen's flow at the outer region.

For the flow past a sphere, Kaplun's method provides the drag coefficient as

$$C_D = \frac{24}{Re}[1 + \frac{3}{16}Re + \frac{9}{160}Re^2 \ln Re + O(Re^2)] \tag{2.32}$$

and the drag coefficient for the flow past a circular cylinder as

$$C_D = \frac{8\pi}{ReS}(1 + \sum_{2}^{\infty} \frac{a_n}{S}) \tag{2.33}$$

where a_n is a constant and S is a function of Re.

Chapter 3

Literature Review

3.1 Flow past Butterfly Wings or Wing Models

Nachtigall (1967) performed experiments on butterflies and moths to investigate the aerodynamic effects of the scales found on the wings of most of these insects. After an observation that, when the scales are scraped off, butterflies take off with a great difficulty and some times do not take off at all, Nachtigall measured the lift L and the drag D for 10 different butterflies and moths, with and without scales. In some experiments, the dead insect with outstretched wings was positioned in front of a nozzle giving velocities from 1.35 to $2.30ms^{-1}$. The insect was linked to a sensitive system for measurement of the lift and drag (see Figure 1), and could be turned at angles of attack varying from $-15°$ to $+60°$with $1°$ increment. For most of the insects the aerodynamic advantage of the scales was obvious. For example, Figure 2, shows the results for an Agrotis moth. Figure 2(a) shows that removing the scales caused an increase in the lift with no noticeable change in the drag. Figure 2(b), representing the lift-drag polar curves demonstrates that for a given drag, the lift is higher when scales are not removed. Nachtigall also compared the lift-drag polar for a Drosophila butterfly to that for an airfoil and a locust (see Figure 3). It was observed that the maximum lift coefficient of the

butterfly wing, although lower than that of the airfoil, occurred at a critical angle $\alpha_{crit} = 50°$, much larger than the airfoil critical angle, $\alpha_{crit} = 19.5°$. It was also observed that,unlike the lift-drag polar curve for an airplane wing which drops dramatically for angles larger than the critical angle, this curve for the butterfly remains relatively flat after the critical angle. This means the butterfly wing has the advantage of being more stable than the airplane wing if the critical angle is exceeded.

Hoover (1977) designed a terraced wing sailplane and studied its performance. His design was motivated by studies and experimentation done by Lippish (1971), who found that the air flow on a terraced wing glider remains attached to the wing at larger angles of attack than it is on a conventional smooth airfoil. The designed sailplane which was called Vill Doo stalled on high-start but recovered nicely with down trim back in giving increased lift with little noticeable change in drag. Also on a duration flight the Vill Doo stayed in the air longer than all other sail planes.

Christopher (1975) did measurements of lift and drag forces acting on corrugated airfoils. He used stainless steel scale models of a wing section of the hover fly Syrphus balteatus. The aerodynamic properties of the corrugated model were compared with those of a smooth model of the same aspect ratio. The lift and drag of these models were measured using force balances in a closed circuit fluid flow channel filled with an aqueous sucrose solution. Measurements were carried out at Reynolds numbers of 450, 800 and 900. Chirstopher found that the lift and drag coefficients of corrugated and smooth airfoils are similar. He concluded that corrugated wings have the advantages of low mass, high stiffness and low membrane stresses in bending without any obvious aerodynamic disadvantage by comparison with smooth profile wings.

Tavoularis et al. (1985) studied separation and reattachment in flows over asymmetric cavities at small Reynolds numbers using flow visualization. A plexiglas model consisting of four saw tooth-type steps, which were crude two-dimensional models of the scales on the upper surface of the Monarch butterfly wing, was towed in a transparent towing tank. Flow visualization at various Reynolds numbers was performed using aluminium dust. Photographs of streaklines in and above the third step showed a stationary recirculating vortex. The size of the vortex increased with increasing Reynolds number. A numerical simulation using conformal mapping was also performed and provided results compatible with flow visualization results.

Newman et al.(1977) conducted experiments to obtain quantitative information on the aerodynamics of the dragonfly wing and to determine whether some of the wing characteristics have an aerodynamic significance. A wing model of Aeshna Cynea was built and used for flow visualization, and a model glider having the same wing section was flown indoors. Photographs were taken using stroboscopic illumination with long exposure to give flight speed, altitude and angle of attack. The model was mounted in a smoke tunnel, the flow was studied at various angles of attack and at Reynolds number of about 10^4. At 0° a trapped vortex was observed in the first valley of the section. At 12° the flow was fully separated near leading edge and reattached at about 2/3 chord from the leading edge as a turbulent boundary layer. At 15° the flow was fully separated. Free flight tests of the glider were made indoors to reduce the ambient turbulence. Two model gliders were constructed, designed to fly at typical Reynolds numbers of 10^4 and 4×10^4 respectively. The first model had interchangeable wings so that the Dragonfly wing performance could be compared with that of a curved plate airfoil.

The models were launched from a height of about 5.5 m above the gymnasium floor. Test data were obtained by panning the gliding model with stroboscopic illumination and two cameras were used to determine the flight altitude, flight path angle β, and flight speed U_{inf}. From these data the lift and drag coefficients of the wing were calculated . Plots of C_L vs α ,C_D vs α and C_L vs C_D showed that the Dragonfly wing section is aerodynamically very efficient and comparable to a very high performance low Reynolds number airfoil fitted with an artificial turbulator. The effects of the turbulator are to increase the drag slightly and to increase the lift considerably at a given α before stall. With the turbulator in place the first stall occurs at a higher C_L. It is probable that the actual dragonfly wing, which contains several small features not present on the test models, has an even higher performance. Some of these features may be observed from the electron microscope pictures of a small Libellua. The form of the spurs was clearly seen and the height above the diaphragm was $55\mu m$. Other pictures of Aeshna Interrupta were taken and the spurs height was found to be $90\mu m$ to $100\mu m$. They also had an orientation of about + or-10^0. It was found that the height of the spurs is proportional to the wing chord. The height of the spurs was also found to be less then the maximum roughness which renders the surface aerodynamically rough. The pictures also showed the presence of hairlets; the author explained their role as to sense the airflow and to keep the stagnation point exactly at the leading edge. They may also monitor the rate of incidence or camber change, which is mainly controlled by muscles attached to the leading edge ribs, to ensure that the lift is maintained and the drag does not become unduly high.

Buckholz (1986) studied the role of irregularities on butterfly wings in the Reynolds number range 10^2 to 10^3. His study consisted of a two-dimensional flow

visualization on two different wing sections; one of them was a sheet metal model with geometry matching that of a butterfly wing, and the other was an thicker plexiglas wing, corrugated on the upper surface. He then measured the reduction in pressures on the corrugated upper wing surface. Experiments were performed in a low speed wind tunnel. The flow visualization results were obtained using a smoke wire method. Static pressures along the wing section were sequentially measured using an electronic manometer capable of measuring pressure differences of 0.0025 mm of water. The smooth and corrugated wing sections were subjected to the same flow at identical angles of attack. Flow visualization on the butterfly airfoil model showed a large laminar recirculation bubble in the wing corrugation fold just behind the leading edge. Laminar reattachment occurred after the separation bubble. It was observed that the size of the recirculation zone changes with Reynolds number and angle of attack. Photographs of streaklines near the corrugation of the upper surface of the corrugated surface plexiglas airfoil showed trapped vortices inside these corrugations. From this experiment no stall delay due to wing surface corrugation occurred.

3.2 Separation of Low Reynolds Number Flows and Flow in Cavities

Taneda (1979) studied separating viscous flows using glycerine and silicone oil as the working fluid, and aluminium powder and glass beads for flow visualization. He investigated flows around bodies placed in a uniform flow, flows past bodies placed near a plane wall and flows past wall irregularities such as corners, cavities and steps. He found that for a flow past a semicircular arc ($Re = 3.1 \times 10^{-2}$ based on arc diameter), a vortex pair was formed within the concavity of the

arc. The distance between the two vortex centers was 0.52 times the diameter. The streamline patterns was not altered when the flow was reversed. For two equal spheres or cylinders placed streamwise, with the Reynolds number equal to 1.3×10^{-2} and 1.0×10^{-2}, the flow pattern depended on the ratio of the gap ϵ between the two spheres or cylinders to their diameter d. For the two spheres, when $\epsilon/d = 1$ separation of the flow does not occur, but when $\epsilon/d = 0.7$ and, 0, the flow separates from the spheres and vortex rings are formed in the gap. For the two cylinders, when $\epsilon/d = 1.5$ flow separation does not occur, but when $\epsilon/d = 1.0$ two vortex pairs appear, and when $\epsilon/d = 0$ or 0.5 the two vortex pairs merge into one vortex pair. For two equal circular cylinders facing the flow side by side, with a Reynolds number equal to 1.1×10^{-2} based on the cylinder's diameter, separation occurs for values of ϵ/d greater than or equal to 0.2. For a circular cylinder placed near a plane, it was observed that linear flow was established on the flat plate up to a height 6 times the cylinder diameter. When $\epsilon/d = 0.6$ flow separation does not occur, but when $\epsilon/d = 0.25, 0.1$ and 0 the flow separates (ϵ is the gap between the plane and the cylinder and d is the diameter of the cylinder). The Reynolds number was equal to 1.1×10^{-2} based on the cylinder diameter. For the flow past a vertical fence one large vortex was formed in the corner. The distance between the vortex center and the corner point was 0.54 times the fence height. The streamline patterns remained unaltered even when the direction of motion was reversed, and the angle of the fence with the flat plate was changed. The Reynolds number was equal to 1.4×10^{-2} based on fence height. For a square bank on a plane a large vortex is formed within the corner. The distance between the vortex center and the corner is 0.46 times the bank height. The Reynolds number was equal to 2.0×10^{-2} d based on bank height. For the flow past a step,

the flow pattern was unaltered even though the direction of motion was reversed. A large vortex was formed within the corner. The distance between the vortex center and the corner point was 0.47 times the step height. The Reynolds number was equal to 1.0×10^{-2} based on step height.

For the flow past a rectangular cavity the flow depended on the aspect ratio b/h (where b is the width of the cavity and h its height). For b/h=0.5,1 and 2 a single vortex was formed in the cavity. For a $b/h = 3$ a double vortex was formed. The dividing streamline was not coincident with the mouth of the cavity. The Reynolds number was equal to 1.0×10^{-2} based on cavity depth. For the flow past a sharp corner induced by a rotating cylinder, a large vortex was produced by the rotating cylinder and a smaller vortex induced by it and having opposite direction of rotation was observed. The Reynolds number was equal to 1.7×10^{-1} based on corner depth. From his investigation Taneda concluded that the streamline pattern is reversible independent of the Reynolds number when the Reynolds number is lower than about 0.1, and that the time taken for the steady flow to be established is negligible.

Munson et al. (1985) studied low Reynolds number circular Couette flows past a wavy wall theoretically and experimentally. They showed that it is possible to obtain flow separation or reverse flow for low Reynolds number shear flow past a wavy wall. It was found that the region of reverse flow depends on the amplitude of the wall waves and on the gap width.

Shen and Floryan (1985) investigated the low Reynolds number flow over rectangular cavities. They used a numerical analysis to simulate the towing tank experiment of Taneda. The N.S equation was approximated using the central difference method. The boundary conditions were generated from conditions of no

slip and no penetration at the solid boundaries, and conditions at the free stream. They particularly analyzed the effects of the cavity's aspect ratio on the structure of the flow field, the location of the separating point and the shape of the separating streamline. They found that the dividing streamline separates from the cavity side wall below the upper corner. The separation point moved upward when the aspect ratio decreases. The flow structure inside the cavity was found to be strongly dependant on the aspect ratio. Only corner vortices existed in a cavity of aspect ratio w/h=4.0 and a decrease of the aspect ratio caused enlargement and eventual merger of these vortices. A single vortex was formed at an aspect ratio of 2.0. Further decrease of the aspect ratio results in formation of new corner vortices, their enlargement and their eventual merger. At an aspect ratio of 0.5 two central vortices were observed. Below this aspect ratio additional central vortices were created.

Weiss and Florsheim (1965) developed an approximate solution for low Reynolds numbers flow fields in rectangular cavities. In this approximate solution the vorticity convection term was neglected. The flow was assumed to separate and reattach at the cavity corners connected by a straight streamline . Consequently the flow outside the cavity was not affected by the cavity presence. They found that a single recirculation cell exists as long as the aspect ratio H/L does not exceed a certain value between 1 and 2 (H is the height of the cell and L its width). When that value is exceeded a new cell is formed at the wall. The size of the new cell increases as H/L increases. At H/L=4.0 a third cell appears. They also found that the strength of each new cell formed is reduced compared to the previous one. Weiss and Florsheim then conducted experiments on wall cavities at a Reynolds number of 150 and confirmed the prediction of double celled cavity. They con-

cluded that the zero Reynolds number solution has an extensive range of validity in flows with closed streamlines.

Takematsu (1966) has examined analytically a shear flow past a cavity on infinite depth using the Stokes approximation and has shown that separation and reattachment of the flow does not occur at the entrance edge of the wall cavity, and that the outer flow penetrates to a considerable depth into the cavity.

Ratkowsky and Adorotem (1968) developed an approximation model for a closed streamline flow in a rectangular cavity. They used the boundary conditions of constant shear stress over the open side of the cavity. They found that for very small aspect ratios, ϵ, the location of the vortex center is at a distance d=$\epsilon/3$ from the open side of the cavity and that for $\epsilon \geq 1$ the position of the main vortex center and the value of the inner stream function remain practically unchanged.

Sturge (1986) examined analytically the Stokes flow in a two dimensional cavity with moving end walls. They found that for an aspect ratio less then 1 the flow patterns consist of a single eddy that fills the entire cavity. As the aspect ratio increases the eddy pinches off in the center, forming two small eddies. Then, small eddies form at the center of the side walls, grow toward the center and finally coalesce into a central counterrotating eddy.

Pan and Acrivos (1966) investigated the steady flow in a rectangular cavity where the motion is driven by the uniform translation of the top wall. They obtained numerically the creeping solution for cavities having aspect ratios from 0.25 to 5 using a relaxation technique. They found that for an aspect ratio less than or equal to 1 a single vortex fills the cavity and small vortices are formed at the corners. For an aspect ratio equal to 2, two counterrotating vortices are formed. As the aspect ratio is increased more vortices are induced. Values for the height

of the vortices and the location of their centers were obtained. An experimental study was then carried for Reynolds numbers varying from 20 to 4000. Flow visualization was used to determine the flow patterns. They concluded that for finite cavities, the viscous and inertia effects have comparable magnitudes even for higher Reynolds numbers in that range.

O'Brien (1982) used a finite difference analysis to investigate the viscous flow in an annulus with a sector cavity. She concentrated on the location of the dividing streamline and found that the stagnation points of the dividing streamline fall inside the cavity, that the dividing streamline is not confined within the cavity but may be located partially in the shear flow region, and that the velocity and vorticity vary along the dividing streamline and both go to zero at the walls.

3.3 Low Reynolds Number Flow past Pitot Tubes

Barker (1922) was the first to perform an experiment to determine the pressure difference between a pitot and a static tubes when placed in a low velocity fluid. She mounted a pitot tube of circular cross-section, 0.10 cm in diameter in the center of a brass pipe 70 cm long and 1.10 cm in diameter. The pipe was placed in a trough of water with a stop-cock at the end regulating the flow. A hole on the side of the pipe opposite to the mouth of the pitot tube was connected to one side on a chattock tilting gauge and the pitot tube to the other. Nitro benzene of density 1.207 was used as the heavy liquid in the chattock tilting gauge. Velocity of the water in the pipe was measured by the discharge, and was kept below $0.2cm/s$ in order to be in the laminar flow range. Results of the experiment (see Figure 4) showed that for values of $Re < 60$ the viscosity caused the relation between pressure difference and the velocity to deviate from Bernoulli's equation and that

the measured value of the pressure coefficient Cp exceeded unity. For values of $Re > 60$ the pressure difference between the pitot tube and the static tube was proportional to the velocity squared and the pressure coefficient Cp, was found to be approximately unity. It was not clear if the Reynolds number was based on the external or internal diameters of the pitot tubes. Barker suggested that repeating the experiment using a fluid 5 times heavier than water would lead to more accurate results.

Homman (1952) determined theoretically and experimentally the intensity of impact pressure on cylinders and spheres in viscous flows. His theoretical work was based on the thin boundary layer theory and his results were expressed in terms of C_p and Re as

$Cp = 1 + \frac{6}{Re + 0.45 Re^{\frac{1}{2}}}$, (Sphere)

$Cp = 1 + \frac{4}{Re + 0.45 Re^{\frac{1}{2}}}$, (Cylinder)

where Re was based on the radius of the cylinder or sphere. The experiments performed over the range of Re between 2 and 120 were in good agreement with the theoretical results as shown in Figure 5.

Experiments were made by Hurd et al. (1953) to determine the effect of viscosity on the pressure rise recorded by a blunt-nosed impact tube in incompressible flow. A circular towing tank having a mean diameter 3048 mm and a rectangular cross section 203 mm wide and 254 mm high was used in the experiment. A variable speed motor was used to advance the pitot tube around the center axis of the towing tank. The circular pitot tube had an outside diameter of 1.83 mm and an inside diameter of 1.35 mm, and a square nose cut. Velocities at the tip of the pitot tube could be calculated from the known angular velocity of the motor. The impact pressure was measured using a manometer. The results were presented in a

graph of the pressure coefficient Cp vs the Reynolds number based on the diameter of the cylindrical portion of the pitot tube (see Figure 6). For Reynolds numbers higher than 1000 there was no effect of viscosity and Cp was equal to unity. For Re between 50 and 1000, Cp was slightly less then unity. For $Re < 60$, Cp was always greater then unity. For $Re < 1$ the pressure coefficient was independent of the fluid density and could be approximated by $Cp \cong 5.6/Re$.

An experiment was made by Macmillan (1954 a) to determine the viscous effect on the pressure in a circular blunt-nosed pitot tube. He used pitot tubes of different sizes mounted on the center line, near the entry of a vertical pipe. A suction fan was used to regulate the air flow in the pipe. A null reading inclined tube manometer was used to measure the small pressure differences between a static hole and the pitot tube. A flowmeter placed downstream from the pipe entry was used to measure flow velocities. The Reynolds number based on the external diameter of the pitot tube varied between 15 and 1000. Macmillan compared his results to those obtained by Hurd et al. (1953). He found that the value of Cp did not fall below unity at any value of Reynolds number. He explained the decrease of Cp below unity found by Hurd et al. to methodological errors. He also found that when his results were expressed in terms of Reynolds number based on the inner diameter of the pitot tube, the differences with those obtained by Hurd et al. were reduced and He concluded that the viscous effects on pitot tubes are better correlated with the internal diameter.

In a second experiment Macmillan (1954 b) repeated the previous work using flattened, blunt nosed pitot at Reynolds numbers between 13 and 1000 based on the external height of the pitot tube. He presented his results in graphs of Cp vs Re for different ratios W/H of the pitot tubes. (where W is the width of the

pitot tube and H is its height) as shown in Figure 7. He found that for $W/H = 1$, (circular pitot tubes) the value of Cp never falls below unity. For W/H different from 1 the value of Cp falls slightly below 1 for a certain range of Reynolds numbers depending on the value of W/H (for $W/H = 11$ Re varied from about 12 to1000).

Mikhailova and Repik (1975) investigated the dependence of the value of Cp obtained from a pitot tube in a viscous flow on the value of $\beta = d/D$ (d is the inner diameter of the pitot tube and D is its outer diameter). A series of pitot tubes with different values of β were mounted in an experimental facility similar to the one used by Macmillan. From the results of the experiment the authors concluded that the effect of viscosity is greater for tubes with thick walls (small β) than for tubes with thin walls (large β). The authors explained the divergence of the results of Hurd and Macmillan according to this observation. For pitot tubes with $\beta = 0.6$, which are among the most commonly used in practice, Mikhailova and Repik suggested the relation $Cp = Re/(1.07Re - 3.7)$ for $6 < Re < 30$, where Re is based on D. For some values of β, a decrease of Cp below unity was found within a certain range of Re. Mikhailova and Repik postulated that the decrease in Cp values below unity within certain range of Re was the result of a lowering of stagnation pressure in the pitot tube due to a suction of liquid out of the internal cavity of the tube, and promoted by the action of the viscous flow around it.

Chapter 4

Experimental Facilities And Instrumentation

4.1 The Liquid Channel

A closed return liquid channel (see the reports by Tittley,1985, and Aubrey, 1986, for design details) was used to generate the flow field. The channel, shown in Figure 8, was made of plexiglas to permit optical access and observation of the flow in different parts. Water and glycerine were used as the working fluids in this channel. Figure 9 shows that at the usual range of indoor temperature the glycerine has the highest viscosity compared to the other fluids; using this fluid will permit reaching very low Reynolds numbers at convenient flow speeds and model sizes. The fluid flow around a closed circuit is created by a viscous pump, consisting of two sets of meshing disks and similar to the one designed by Odell and Kovaszany (1971). The pump is driven by a 0.5 hp, 1725 rpm motor, through a 15:1 gear speed reducer. Pulley trains having different transmission ratios can be connected to the disk pump giving different rotational velocities and therefore different free stream velocities inside the test section. For water flow, a 50mm diameter pulley was connected to the motor and a 200mm pulley to the pump shaft. When the

water channel was filled with glycerine the torque needed to drive the pump was much higher than that for water. A reduction system, consisting of two additional pulleys of diameters 64mm and 152mm was used between the motor and the pump, reducing the rpm of the pump and increasing the torque exerted on it.

The liquid entered to the pump through the inlet diffuser. To avoid separation and formation of large eddies due to the adverse pressure gradient in the diffuser, a flow divider was inserted into the diffuser. The flow divider permitted a gradual increase of the effective cross sectional area in the diffuser as well as directed the fluid towards the active sections of the pump. The fluid streams from the two sides of the pump merged after passing through a contraction including a flow divider in order to reduce flow nonuniformity and possible turbulence.

A settling chamber was installed before the test section to improve the flow conditions. It consisted of three sections, the inlet diffuser, the parallel section and the contraction. Two valves located on the channel bottom before the inlet diffuser and after the test section, could be used for filling and emptying the channel with the working fluid. Water from the city supply was filtered before entering the channel. Vents were also used to evacuate air from water channel while filling it, and to maintain a slight overpressure inside the liquid channel. The liquid channel and the motor were mounted such that vibration of the system was minimal. The test section was 200mm long, 150mm high, and 150mm wide. The side walls were made of glass, while plexiglas was used in the remainder of the channel.

4.2 Laser Doppler Anemometry

The Laser Doppler Anemometry system used is shown in Figure 10. It consisted of a laser, an optical unit, a Bragg cell, a photomultiplier tube, a signal tracker

and a frequency shifter.

A Helium-Neon laser (Spectra-Physics model 120) with an output power of is 5.0 mW and a wave length of 632.8 nm was available for most measurements. This was later replaced by a 10.0 mW Helium-Neon laser (Spectra-Physics model 106.1).

The optical unit (DISA 55L01) contains a biprism, an adjustable surface mirror, and a beam adjuster. The biprism and the adjustable surface mirror constitute the beam splitter. The surface mirror can be moved using a micrometer permitting variation of the beam separation between 18 and 54 mm. The beam adjuster consisted of two micrometers, used to obtain perfect intersection of the beams at the point of measurement.

The laser beam separation had to be maintained fixed at 30 mm in order to allow the two beams to pass through the two holes of the Bragg cell. The Bragg cell (DANTEC 55X29) was mounted in front of the optical unit as shown in Figure 11. The Bragg cell is an acousto-optical device which permits a 40 MHz upshifting or downshifting of one of the laser beams which pass through it. The power input to the Bragg cell is supplied from the LM exciter, which is an integral part of the frequency shifter (DANTEC 55N10).

Lenses with either a 130 or a 600 mm focal length were mounted in front of the Bragg cell to focus the two laser beams on the point of measurement. As shown in Figure 11, shifted beams at different angles come out from the Bragg cell. A mask is mounted in front of the lens to block the unwanted beams, and to allow only the first order diffracted beam to pass.

A photomultiplier section (DANTEC 55X08) used in connection with photomultiplier optics unit (DANTEC 55X34), was used to collect the scattered light

from the measuring volume and to provide an alternating current whose frequency is proportional to the Doppler frequency.

A Doppler frequency tracker (DANTEC 55N20) was used for processing of the Doppler signal and determination of the corresponding velocity. The tracking frequency range was 1KHz to 10MHz. The frequency tracker has a modular construction, containing the following modules :

-The 55N21 tracker main unit, comprising the main frame, the power supply and the tracker IEEE-488 Interface.

-The 55L97 high voltage supply, used to supply the photomultiplier tube with high voltage.

-The 55N24 display module; this module is used for displaying mean velocity during a time interval determined by front panel control setting.

A 55N10 frequency shifter was also used in connection with the frequency tracker. The combination of optical frequency shifting obtained by the Bragg cell and the electronic frequency shifting obtained by the 55N10 frequency shifter extends the applications of the system to include measurements at very low velocities and reversing flows. The frequency shifter consists of the following main block units :

-Frequency shift generator unit

-Fixed divider board

-LM exciter

-Mixer unit

-Power supply.

The photomultiplier is connected to the mixer input, 'PM IN' of the 55N10 frequency shifter. The output of the mixer, 'MIXER OUT' is connected to 'PHO-

TODETECT IN' of the frequency tracker. The LM exciter supplies power to the Bragg cell as shown in Figure 11.

Setting the wanted frequency shift is accomplished using the front panel. The frequency shift, namely the combination of the electronic and optical frequency shifts, is transferred from the frequency shifter to the frequency tracker in digital form, by using a digital cable connecting FREQUENCY SHIFT DIGITAL OUT on the frequency shifter and RANGE OF FREQUENCY SHIFT on the frequency tracker.

A KIKUSUI DSS 6521 oscilloscope was used for adjusting the processing equipment and monitoring the Doppler signal.

The laser, the optical unit, the Bragg cell and the photomultiplier tube were mounted on an optical bench by means of adapters. Translating each component on the optical bench was possible without losing alignment with others.

4.3 Traversing System

The traversing system, shown in Figure 12, consists of an optical jack (OPTIKON) mounted on a supporting table. The jack ensures vertical displacement of a table holding the optical bench. The optical bench can be moved horizontally by means of trapezoidal lead.

The supporting table can be levelled by means of four supporting screws. The jack ensures a 100mm vertical displacement with a precision of 50 μm and is capable of supporting a 50 kg weight. The actual weight supported by the jack, namely the weight of the horizontal traversing system, the optical bench and the laser system components mounted on the optical bench was, estimated to be 35 kg.

4.4 Pressure Instrumentation

At first, a Validyne DP108 variable reluctance , diaphragm pressure transducer was used for measuring the pressures. It was connected to a Validyne CDC-23 demodulator. A height gauge and a vertical column were used to provide a known pressure head for calibration. No trustable measurements could be made with this transducer, so a two-liquid manometer shown in Figure 13 was built and used for the measurement of the pressure difference of the pitot tubes. Red gauge oil, having specific gravity of 0.826, was used as the light liquid and glycerine, having specific gravity of 1.254, was used as the heavy liquid. An inclined glass tube was used to produce a larger deviation of the meniscus. A cathetometer having a precision of 0.1mm was placed at the same angle as the inclined tube to measure the deviation of the meniscus when a pressure difference was applied to the manometer.

4.5 Flow Visualization Equipment

A NIKON FE2 camera was used for photography of flow visualization. A cylindrical lens mounted in front of a 10mW Helium-Neon laser provided a laser sheet for illumination.

Chapter 5

Experimental Procedures And Accuracies

5.1 Basics of Laser Doppler Anemometry

The Laser Doppler Anemometry (LDA) permits measurement of the instantaneous velocity in a flow. It is based on the Doppler effect, which states that the frequency of a light scattered by a moving particle is shifted with the frequency of the oncoming light. The frequency change is proportional to the particle velocity. For a workable measuring process the light beam to be used has to be monochromatic, coherent and having a high intensity. The laser satisfies these requirements.

The basic LDA system (Fig 10) consists of a laser, an optical unit to split the laser into two beams and focus them on the measuring volume, a photodetector, which senses the frequency shift and then gives an alternating current having a frequency equal to the frequency shift, and a signal processor to analyze the signal from the photodetector and give the value of the velocity.

The two commonly used modes of operation of LDA are the reference beam mode and the differential Doppler mode. In the reference beam mode, light scattered from one of the laser beams heterodynes in the photodetector with light from

a reference beam. In the differential Doppler mode, two laser beams intersect at the measuring point. The scattered light can be picked up over a wide angle since the differential Doppler frequency is independent of the direction of detection. This mode of operation is also called the fringe mode, because the two incident beams form a fringe system as shown in Figure 15. In the present investigation the differential Doppler mode is used. Its advantages are that it has a good signal to noise ratio for low scattered light intensity and it does not require alignment of the photodetector with the optical unit.

The relationship between the Doppler frequency shift and the velocity of the particle passing through the control volume is given by

$$f_D = U\frac{\sin\frac{\theta}{2}}{\frac{\lambda}{2}} \quad . \tag{5.1}$$

where U is the velocity component (on the plane formed by the two laser beams and perpendicular to the bisector of their angle) of the particle passing through the control volume, θ is the angle of intersection of the two laser beams and λ is the wavelength of the laser beam.

5.1.1 Photomultiplier signal

The signal from the photomultiplier has the form indicated in Figure 14(a) for a single particle passing through the control volume and the form indicated in Figure 14(b) for several particles passing through the control volume in the same time. The concentration of particles in the present experiments are such that several particles are present in the control volume in the same time. The low frequency signal variation corresponds to the pedestal component caused by the passage of particles through one or both light beams, and the higher frequency

signal contained within the envelopes to the velocity of individual particles passing through the region of beams intersection. The frequency of the signal contained in one burst (individual particle's signal) is normally constant due to the very short time required for the particle to pass through the measuring control volume. In most cases a high-pass filter is used to remove the low frequency component. If the required signal frequency is close to the pedestal signal, setting the high-pass filter may be very critical.

5.1.2 Signal processing

The two most commonly used signal processing techniques are the frequency tracking technique and the counting technique.

In a frequency tracker a voltage controlled oscillator provides a continuous signal which is mixed with the Doppler signal. A discriminator provides frequency to voltage conversion and the voltage is proportional to the instantaneous velocity.

In the counting technique, the frequency is determined by counting the number of zero crossings in a certain time interval.

5.1.3 Frequency shifting

For a basic LDA system, the velocity-Doppler frequency graph is shown in Figure 16. Positive and negative velocities having equal absolute values correspond to the same Doppler frequencies. Also the signal processor has a certain frequency range (fmin,fmax) over which Doppler frequencies can be processed. The frequency tracker used in the present experiments can process frequencies in the range 1KHz to 10MHz). Therefore, low velocities corresponding to Doppler frequencies less than 1KHz and flow reversal cannot be detected.

Frequency shifting permits shifting of the velocity-Doppler frequency graph as shown in Figure 18 so that negative and low velocities can be measured.

There are two types of frequency shifting, optical frequency shifting and electronic frequency shifting. The optical frequency shifting consists of applying a frequency shift f_s to one of the laser beams (see Figure 17). This results in a movement of the fringes in the control volume at a velocity

$$U_s = f_s.d_f \tag{5.2}$$

where d_f is the distance between two fringes. A stationary particle within the illuminated volume thus produces a signal of frequency equal to the frequency shift f_s. Movements in the same direction as the fringes decrease the signal frequency and movements in the opposite direction increase it. Different methods have been used to produce optical frequency shifting. The simplest method makes use of the Doppler shift on scattering from a surface moving with uniform velocity. A rotating disk is usually used for this purpose. This method has been successfully applied but it has the disadvantage of introducing random amplitude and phase fluctuations of the shifted laser beam. Another technique is based on the fact that Doppler shift of a laser beam can also be obtained by reflection or diffraction from moving objects. For this purpose moving mirrors or prisms are used. This technique has the disadvantage that the shift is interrupted as the moving mirror or prism reaches the end of its possible movement. There are several other methods of producing an optical frequency shift which makes use of electro-optic materials. In these methods a rotating electric field is generated in the electro-optic cell (containing the electro optic material) and the incident circularly polarized light beam is either accelerated or decelerated depending on the direction of rotation,

thus causing shifting of the outgoing laser beam.

The most popular frequency shifting technique involves the use of acousto-optic cells. This technique is based on the Debye-Sears effect by which a light beam passing through an acousto-optic cell is divided into several beams with different frequencies and directions.

If the angle between the light beam and acoustic wave satisfies the so known Bragg condition:

$$\sin \phi_B = \frac{1}{2}\frac{\lambda}{\Lambda} \tag{5.3}$$

where ϕ_B is the Bragg angle, λ is the wave length of the laser and Λ is the ultrasonic wavelength, reflections from successive wave fronts are reinforced. Acousto-optic cells generally make use of this effect to enhance the efficiency and are often known as Bragg cells.

In the present work a Bragg cell is used; it permits an optical shifting of the laser beam by 40MHz.

For many applications of LDA, the 40MHz frequency shift is too large and above the range of some processing equipment. Electronic shifting, which is mixing the PM signal with a variable frequency shift generator signal, yields downshifting of the signal before processing.

Another advantage of using frequency shifting is the pedestal removal. The pedestal signal has a frequency band which often lies outside the band of Doppler signals, and the Doppler and pedestal signals can in these cases be separated by filtering. As the mean velocity tends towards zero or as the turbulent intensity increases, removal of the pedestal signal becomes more difficult. Light frequency shifting can increase Doppler frequencies without altering the pedestal signal fre-

quency. So the removal of the pedestal signal becomes easier.

5.2 Methodology of Velocity Measurements

5.2.1 Mounting and adjustment of optics

Laser and optical unit

The laser is mounted on the optical bench and power is applied to it. The height of the laser head is adjusted so that the laser beam is parallel to the optical bench's top. The optical unit is mounted in front of the laser, at a distance from the measuring point equal to the focal length of the lens to be used. As will be pointed out in section 5.3 position of the beams' intersection changes due to the difference in refractive indices of air, glass and water or glycerine through which the laser beams should pass. The laser beam intersection is directly focussed on the point of measurement so no correction for this change is needed. The height of the optical unit is adjusted above the optical bench until the laser beam hits the biprism and comes out from the Bragg cell hole. The mirror reflecting the other laser beam is adjusted so that the reflected laser beam comes out from the center hole of the Bragg cell. The optical unit can be rotated depending on which component of the velocity is to be measured.

As shown in Figure 11, the beam coming out from the center hole of the Bragg cell is the one shifted by 40MHz, while the other laser beam passes through a glass rod. The glass rod ensures that the shifted and the unshifted laser beams have the same optical length.

Bragg cell adjustment

To facilitate the adjustment of the Bragg cell, the front lens of the optical unit is dismounted. The two laser beams are projected on a black screen approximately 1m in front of the optical unit. The Bragg cell is connected to the 40MHz output socket of the frequency shifter and power is applied to the frequency shifter.

On the black screen for the laser beam passing through the Bragg cell different beams at different beams at different angles are observed simultaneously. To distinguish the nondiffracted laser beam (zero order) from the diffracted beams, the frequency shifter is switched off and only the nondiffracted beam will be present. The Bragg angle is adjusted through the Allen screw shown in Figure 11 when the zero order beam has the maximum intensity, an the neutral position of the Bragg cell has been reached. The correct angle to be used is the angle corresponding to one of the two first order beams which is closest to the nondiffracted zero order beam on each side of the neutral position. To get a +40MHz frequency shifting the allen screw is turned clockwise from the neutral position until the first order beam appears. To get a -40MHz optical shifting, the Allen screw is turned counter clockwise until the first order beam appears.

The lens is then mounted in front of the optical unit and a mask is mounted on the optical bench to allow only the diffracted first order beam to pass as shown in Figure 11.

In the optical unit the laser beam is split up, one beam is shifted at an angle ϕ_B through the Bragg cell and the other passes through a glass rod. The two beams are focussed at the focal point of the lens. During the experiments two lenses having focal lengths of 600mm and 150mm were used. The 600mm focal length

lens permits better spatial resolution and signal to noise ratio. But a better access to points of measurement is permitted by the 150mm focal length lens, since the angle of intersection of the two beams is smaller. In the following the use of the 600mm lens will be referred to as case(a) and the use of the 150mm lens will be referred to as case(b). The two beams must intersect perfectly and in order to ensure this, a test objective is placed at the focal point to project the intersection volume on a screen. Two glass wedge plates permit changing the direction of the nonshifted beam. When these two plates are adjusted correctly, the picture of the beam, intersection on the screen will show two overlapping spots with interference stripes as shown in Figure 19.

Alignment of the laser beams relative to the test model is accomplished by adjusting the four screws of the traversing system's supporting table.

Adjustment of the photomultiplier

The photomultiplier is mounted on the optical bench at a distance equal to the focal length of its front lens. The optical axis of the photomultiplier is aligned to intersect the measuring volume. Since scattered light from any direction can be collected by the photomultiplier, the direction of alignment is not critical. The pinhole center is moved to the image center of the beam intersection point, using the two PM pinhole adjustment while looking at the pinhole in the magnifying glass. Focussing is accomplished by rotating the close-up lens. A click in the knob indicates correct focussing.

5.2.2 Adjustment of electronics

Connections of optical equipment and the processing electronics are shown in Figure 11. Adjustment of the electronics is greatly simplified if the input signal is displayed on an oscilloscope. The oscilloscope helps also to readjust the photomultiplier and the beam intersection.

Having an idea about the range of velocities to be measured, the frequency range is set on the front panel of the frequency tracker and the frequency shift is set on the front panel of the frequency shifter.

The frequency shift f_s should be chosen so that the relation between the measured velocities and corresponding frequencies is linear. The high voltage supplied to the photomultiplier and the gain of the frequency are adjusted for amplification of the input signal. A better signal to noise ratio is obtained when the gain of the frequency tracker is low and the gain of the photomultiplier related to the high voltage supply is high. The high voltage should be adjusted such that the anode current of the photomultiplier does not exceed a certain limit. When making measurements in turbulence, the filter cutoff frequency should be chosen higher than the turbulence frequencies under investigation. In the present experiments, since no turbulence is involved, the lowest cut off frequency was chosen.

5.3 Relation between Particle Velocity and Fluid Velocity

Since it is the particle velocity which is measured, the relationship between the particle and fluid velocities as well as the dynamic response of the particles are two important factors.

The motion of particles suspended in a moving fluid is affected by the particle shape, the particle size, the relative density of particle and fluid, the concentration of suspension and the body forces.

The equation of Basset (1880) describes the motion of particles in the fluid. It is a very complex equation. Assuming an incompressible fluid, an infinite extent of the flow, no slip between fluid and particle, a small relative Reynolds number, a steady particle motion and a rigid particle, The Basset's equation reduces to the first order linear equation

$$\frac{dU_P}{dt} = \frac{1}{\frac{\rho_P d^2}{18\nu}}(U_F - U_P) \tag{5.4}$$

Where U_P is the particle velocity, U_F is the fluid velocity, ν is the dynamic viscosity of the fluid, ρ_P is the density of the particle, ρ is the density of the fluid and d is the diameter of the particle. $\tau = \frac{\rho_P d^2}{18\mu}$ is the time constant and represents the time response of the particle motion to the fluid motion. If one assumes a density of the particle $\rho_P = 1600 Kg/m^3$, a diameter $d = 5\mu m$ and at temperature of $29.0°C$ the kinematic viscosity of glycerine is $\nu = 775 \times 10^{-6}$ and its density is $\rho = 1256 Kg/m^3$ then $\tau = 0.0036s$. This shows that the particle responds to changes of the fluid flow almost instantaneously.

The gravity effect also causes sinking or rising of the particle. The terminal sink or rise velocity of particles is given by

$$V_T = \frac{(\frac{\rho_P}{\rho} - 1)gd^2}{18\nu} \tag{5.5}$$

For example a particle in the free stream having a velocity of $4.0 cm/s$ sinks $7.22 \times 10^{-3} m$ when it travels a distance of 6 cm, (the length of one cavity), or, inside the cavity in the recirculation region where the velocities are very low, if we

approximate the fluid velocity to be $0.5 \times 10^{-4} m/s$ along a pathline of length 23 mm then the particle will sink about $2.2 \times 10^{-6} m$.

5.4 Position Change of Laser Beam Intersection

When the two laser beams are focused on the measuring point in the test section, they pass through three media of different refraction indices, namely air then glass then water or glycerine. As shown in Figure 20, the intersection position changes due to the difference in refractive indices. Taking the inside surface of the test section wall as reference, the following formula gives the expression of the new intersection point position

$$y' = \left(y + t(1 - \frac{\cos\frac{\theta}{2}}{\sqrt{(\frac{m_2}{m_1})^2 - \sin^2\frac{\theta}{2}}}) \right) \frac{1}{\cos\frac{\theta}{2}} \sqrt{(\frac{m_3}{m_1})^2 - \sin^2\frac{\theta}{2}} \qquad (5.6)$$

where m_1, m_2 and m_3 are the refractive indices of air, glass and water or glycerine respectively, θ is the angle of laser beam intersection, y is the distance from the inside wall of the test section to the intersection point, if the laser passes through media with the same refractive indices, y' is the new position of laser intersection point due to the difference of refractive indices and t is the thickness of the glass wall of the test section. We have $m_1 \simeq 1.0$, $m_2 \simeq 1.5$ and $m_3 \simeq 1.3$ for water and 1.47 for glycerine. The thickness of the wall is $t = 4mm$.

For the 600 mm focal length lens $\frac{\theta}{2} = 1.43°$ giving $y' \simeq 1.3y + 1.73$ for water, and $y' \simeq 1.47y + 1.95$ for glycerine. For the 150 mm focal length lens, $\frac{\theta}{2} = 5.71°$ giving $y' \simeq 1.3y + 1.47$ for water and $y' \simeq 1.47y + 1.97$ for glycerine. The above distances are given in mm.

5.5 System Parameters Calculation

The velocity expressed in terms of the Doppler frequency shift is

$$U = af_D \tag{5.7}$$

The proportionality constant or calibration factor a should be calculated and programmed in the frequency tracker to have direct display of the instantaneous value of the velocity. a is a function of the optical arrangement and is given by

$$a = \frac{\lambda}{2\sin\frac{\theta}{2}} \tag{5.8}$$

In the present system, a is in m/s per MHz, λ is in μm,f_D is in MHz and U is in m/s. Since the beam separation $\Delta$is fixed to be 30 mm for the system used, the angle θ and therefore the calibration factor a depends only on the focal length of the lens used. Two lenses are used throughout the experiment. A130 mm focal length lens giving a value of a equal to 2.76 m/s per MHz, and a 600 mm focal length lens giving a value ot equal to 12.66 m/s per MHz.

The light intensity is not constant across the laser beam, but has a roughly Gaussian profile. The diameter D of the beam, before passing through the transmitting lens, is usually defined as the distance between points with intensity $\frac{1}{e^2}$ of the maximum intensity.

The two equal intensity laser beams form the probe volume or the measuring volume at their intersection. The probe volume is assumed to have an ellipsoidal shape, as shown in Figure 21, where

d_m is the diameter of the focussed laser beam,

$$d_m = \frac{4f\lambda}{\pi D} \tag{5.9}$$

where f is the focal length of the lens.

l_m is the length of the measuring volume

$$l_m = \frac{d_m}{\sin\frac{\theta}{2}} \tag{5.10}$$

h_m is the height of the measuring volume

$$h_m = \frac{d_m}{\cos\frac{\theta}{2}} \tag{5.11}$$

d_f is the spacing between the fringes

$$d_f = \frac{\lambda}{2\sin\frac{\theta}{2}} \tag{5.12}$$

It can be noticed that d_f is equal to the calibration factor a since the velocity of a particle crossing the control volume is equal to the distance between two fringes divided by the time period or multiplied by the frequency.

The number of fringes in the control volume can be estimated by dividing the height of the control volume h_m by the distance d_f between two fringes, as

$$n = \frac{4}{\pi}\frac{\Delta}{D} \tag{5.13}$$

As can be seen from the above expression, the number of fringes depends only on the beam separation Δ and the beam diameter D.

For the 130 mm focal length lens $d_m = 0.161mm$, $l_m = 1.406mm$, $h_m \simeq d_m = 0.161mm$ and $d_f = 2.76\mu m$. For the 600 mm focal length lens $d_m = 0.744mm$, $l_m = 29.77mm$, $h_m \simeq d_m = 0.744mm$ and $d_f = 12.66\mu m$.

The number of fringes obtained by both lenses is $n = 29$.

5.6 Signal to Noise Ration Estimation

The quality of velocity measurement using an LDA system depends mainly on the signal to noise ratio (SNR). The signal from the photodetector consists of three

distinct signal components

$$e(t) = e_P(t) + e_D(t) + e_N(t) \tag{5.14}$$

where $e_P(t)$ is the pedestal component, $e_D(t)$ is the Doppler component oscillating at the Doppler frequency and $e_N(t)$ is the total noise signal. The pedestal component is removed, as mentioned in section 5.1.3 by the use of the frequency shifting . A usual way of estimating the SNR is accomplished by taking the ratio of the power of the Doppler signal to the power of the noise signal (Adrian and Early (1976)). The total noise signal is the summation of the random shot noise generated in the photodetector by the light scattered from the signal producing particle, the random shot noise generated in the photodetector by background illumination, e.g. room lights, light scattered from other particles etc., spurious heterodyne signals generated at the photodetector by laser reflections, flare or scattered light heterodyning together, the random noise generated by photodetector electronics, e.g. Johnson noise, semiconductor surface noise etc..., and radio frequency pick-up usually from Bragg-cell oscillators and from radio stations.

When estimating the SNR it is common to assume that the photodetector can be operated such that the random shot noise is the most dominant one and the others can be neglected. This gives a peak value of SNR. The peak SNR is calculated using the Mie scattering theory and is affected by the characteristics of the light scattering particles in flow, the laser power, the optics configuration and the photomultiplier characteristics (Drain (1980)). So the signal to noise ratio can be expressed as

$$(SNR)^2 = \frac{\eta}{h\upsilon\Delta f} W_s \tag{5.15}$$

where η the quantum efficiency of the photomultiplier, is equal to 0.14 for a red

laser beam and to 0.2 for blue or green laser beams. Δf is the electronic bandwidth, equal to 100 MHz, h is the Plank constant, equal to 6.63×10^{-34} js, v is the optical frequency of the laser and W_s is the power of the scattered light reaching the photomultiplier. W_s can be estimated by

$$W_s = \frac{2W_0}{\pi r_0^2} X_s f_s(\theta) \Gamma \tag{5.16}$$

where W_0 is the laser power, r_0 is the radius of the laser beam (to $\frac{1}{e^2}$ intensity points), X_s is the scattering cross section of the particle, $f_s(\theta)$ is the angular scattering factor, and Γ is the solid angle aperture of the receiving optics. As a typical example, one may assume the particles in the flow to be spherical with an index of refraction equal to 1.43 and a diameter of $1\mu m$. The power of the laser used is 10 mW. The scattering cross section is obtained from the Mie scattering theory, (Drain (1980)), as $X_s = 3.2 \times 10^{-12}$ and the scattering angle factor is determined to be $f_s(\theta) = 2.0$ for the 600 mm focal length lens used and 1.9 for the 150 mm focal length lens. The solid angle aperture of the receiving optics is obtained from the focal length of the lens used for the photomultiplier and the diameter of the aperture. The diameter of the aperture being 48 mm, a value of 9.14° is found for the 300 mm focal length lens and 18.2_o for the 150 mm focal length lens.

Then calculation yields $SNR = 16.5$ for case (a),, and $SNR = 22.7$ for case (b).

5.7 Influence of System Parameters on LDA Performance

5.7.1 Laser beam intersection

The cross section of a focussed laser beam has a Gaussian intensity distribution characterized by the beam waist. The waist, which is the narrowest part of the beam, must be located in the probe volume. For laser beams not intersecting at their waist, a set of diverging fringes is generated as shown in Figure 22 Two particles passing through the probe volume with the same velocities but at different locations will produce different Doppler signal frequencies. A careful adjustment of the distance between the laser and the transmitting lens is needed to obtain parallel fringes (Durst, 1981). For measurements of mean velocity, the resulting error may be reduced when the signals produced by particles passing at different locations are averaged. However for turbulence measurements the error produced may be critical. In new LDA systems a Beam Waist Adjuster is used to focus the beam waist on the probe volume.

5.7.2 Transmitting lens

It was shown that the 600 mm focal length lens gave a bigger probe volume than the 150 mm focal length lens. This results in better spatial resolution for smaller focal length lenses. Also it was shown that the smaller focal length lens gives a better signal to noise ratio. However large focal length lenses have the advantage that more points, especially in the vicinity of the walls are accessible for measurements due to the small intersection angle of the laser beams.

5.7.3 Scattering particles

Increasing the particle size generally increases the intensity of scattered light received by the detector, however, when the particle's diameter becomes large compared with the fringe spacing, it covers light and dark bands of a fringe pattern and thus averages out the variation of light intensity.

5.8 Methodology of Pressure Measurements

The pitot tube was connected to the two-liquid manometer as shown in Figure 13 an the cathetometer was placed at the same angle as the inclined glass tube. After the meniscus stabilizes for the non-flow condition a reference reading on the cathetometer was taken. When the flow was established inside the channel,the deviation of the meniscus was monitored until it reached a steady position, then another reading was taken with the cathetometer. During operation the room temperature had to be held constant to eliminate the effects changing of the shape and position of the meniscus due to the temperature dependance of surface tension.

5.9 Methodology of Flow Visualization

The camera was placed on a tripod in front of the test section and the laser was placed above the test section to provide a thin vertical laser sheet for illumination of the cavity. All the other light sources were turned off. Sufficient number of particles were contained in the flow medium. However, aluminium powder particles were injected occasionally with a syringe inside the cavity.

Chapter 6

Measurements

6.1 Experimental Conditions

The channel was first filled with water, then with glycerine. The temperature inside the test section reached a value of about $25°C$ for both glycerine and water during operation. The specific gravity of glycerine was evaluated using a hydrometer to be 1.256. Using the specific gravity and the temperature of glycerine, from the appropriate tables, the concentration of glycerine and its kinematic viscosity were determined to be 99% and $775 \times 10^{-6} m^2/s^2$ respectively. In order to set the frequency range for the frequency tracker of the LDA system the range of the velocity to be measured needed to be determined. Using a chronometer to record the time spent by certain visible particles to travel a certain distance a crude estimate of the velocity range inside the test section was determined. The vertical and transversal velocity profiles for glycerine flow and the vertical velocity profile for water flow inside the empty test section are shown in Figures 24 and 25. The measurements for glycerine were more consistent and the flow was more steady than for measurements with water. This is probably due to the fact at the higher Reynolds numbers corresponding to water flow some instability might occur in the pump or diffuser sections.

6.2 Cavity Flows

Figure 23 shows a sketch of the plexiglas model which was $15cm$ wide and consisted of four sawtooth-type steps which were crude two-dimensional models of the scales on the upper surface of the monarch butterfly wing. The Reynolds number based on the vertical height of the cavities and the free stream velocities was equal to about 624 for water flow and to about 0.62 for glycerine flow.

6.2.1 Flow visualization results

Photographs of the flow inside and above the second cavity were taken when the liquid channel was filled with glycerine.

Some photographs taken by Tavoularis et al. (1985) in a towing tank for the same wing model at small Reynolds numbers are included in this thesis for analysis and comparison of the two facilities.

Plate 1a shows the flow field inside and above the cavity. In addition to the small impurities suspended in the mixture, aluminium powder mixed with glycerine was occasionally injected inside the cavity using a syringe in order for the vortex to be seen more clearly. Plates 2 and 3 show some photographs taken in a towing tank by Tavoularis et al. (1985) for several values of Reynolds numbers.

In these experiments, vibrations of the towing carriage at high Reynolds numbers resulted sometimes in unsteady vortex shedding. For lower Reynolds numbers, a stationary recirculating vortex is observed. The size of this vortex and the distance between its center and the vertical wall of the cavity decreased with decreasing Reynolds number.

To check the reversibility of the flow at the low Reynolds number range the

wing model was reversed and some photographs of the flow inside and above the second cavity were taken. Plate 1 compares the flow for both directions relative to the cavity. From these photographs it can be seen that the flow patterns are very similar for both directions.

The reversibility was also checked by Tavoularis et al. (1985) by towing the model backwards. The similarity of the flow patterns was less obvious in this case because the quality of the photograph was poorer.

The wing model was then placed at different angles relative to the flow and photographs of the flow inside the second cavity were taken to investigate the effect of changing the angle of attack.

Plate 4 shows the flow field for some positive and negative angles of attack.

6.2.2 Horizontal velocity profiles

Horizontal velocities were measured inside and above the first, the second and the third cavities.

Figures 26, 27 and 28 show the horizontal velocity components for the first, the second and the third cavities respectively.

From each of these figures it can be seen that for glycerine (Re=0.62) the flow reattachment occurs at a closer distance from the vertical wall of the cavity than for water (Re=624). Also, the velocity gradients were higher for water than for glycerine.

Due to the difference in magnitude between velocities above the cavity and inside it, the profiles inside cavities cannot be seen clearly from these graphs. Table 1 provides the values of the measured velocities.

The flow reattachment occurs at a larger distance for the first cavity than for

the second and third. This can be explained by the periodicity of the flow. In fact the flow inside the second and third cavities have similar upstream conditions, namely the presence of another cavity, in contrast with the flow inside the first cavity which is effected by the leading edge of the wing model.

Due to the similarity between results for the second and third cavities, further measurements will be made only for the first and second cavities.

6.2.3 Total velocities inside and above cavities

Measurements of the vertical component of velocities inside and above the first and second cavities, along with the measured horizontal velocities were used to obtain the total velocities and map the flow pattern for these cavities.

Figures 29 and 30 show the flow for the first and second cavities respectively.

6.2.4 Detailed flow inside cavities

To have more details about the flow inside the cavity, a fine grid was used to measure the horizontal and vertical components of the velocities at different points.

Figures 31 shows the detailed flow inside the first cavity for glycerine and water respectively.

Figures 32 shows the detailed flow inside the second cavity for glycerine and water respectively.

The presence of a vortex inside the cavities is obvious from these figures. For water, the size of the vortex is much larger than for glycerine. The flow reattachment occurs at a larger distance from the vertical wall of the cavity, about three times, for water than for glycerine.

Some velocities near the inside corner of the cavity for water flow suggest the

presence of a counterotating vortex. The existence of counterotating vorticities was proved numerically by Moffat (1963) for triangular symmetric cavities and by Shen and Floryan (1985) for rectangular cavities.

6.2.5 Reversibility of low Reynolds number flows

As the Reynolds number tends to zero, the flow pattern should remain unchanged, regardless which direction the flow takes. To test the reversibility of the flow, the wing model was reversed inside the test section when the channel was filled with glycerin. The horizontal and vertical velocities were measured for the second cavity.

Figure 33 shows the flow field inside and above the second cavity and Figure 34 shows the detailed flow for both directions of the flow relative to the cavity.

From these figures it can be seen that the flow patterns are very similar for both directions of the flow relative to the cavity.

6.2.6 Flow at the leading edge

The flow around the leading edge of the wing model was also investigated by measuring the two components of the velocity.

Figure 35 shows the results obtained for glycerine flow and water flow.

Comparing the two figures it becomes obvious that the viscous effects are more important for glycerine than for water.

6.3 Pitot Tube Response

Three pitot tubes were used for these experiments, having external diameters of 1.5, 3.5 and 4.5 mm. In the following these pitot tubes will be referred to as pitot

tube 1, pitot tube 2 and pitot tube 3 respectively.

6.3.1 Flow disturbance by pitot tube presence

Some velocity profiles were taken inside the test section before and after inserting the pitot tubes. The effects of the pitot tube presence on the velocity profiles are shown in Figure 36 and Figure 37 for pitot tube 2 and pitot tube 3 respectively. Measurements for the pitot tube 1 could not be made because its small size resulted in poor spatial resolution.

As can be seen from these figures flow disturabance is larger for lower Reynolds numbers flows.

6.3.2 Pressure coefficient

Since in the previous investigations, no experimental values of the pressure coefficient Cp for very low Reynolds numbers were reported, the present work focuses mainly on this range. Each one of the pitot tubes was inserted inside the test section when it was filled with glycerine and the total-static pressure difference was measured. The pitot tube was then removed and the velocity at the total pressure point was measured using the LDA. Pressure measurements with the third pitot tube could not be made, probably due to the very small size of its static and total pressure holes. The glass tube of the pressure manometer containing the meniscus was placed at an angle of 10.8° with respect to the horizontal. The measured deviations will then be multiplied by the sinus of the angle to get the vertical deviations of the meniscus. The oblique deviations of the meniscus were 18.3 and 14.9 mm for the second and the third pitot tubes respectively and corresponded to LDA measured velocities of 2.76 and 2.54cm/s respectively.

In addition to measurements with the tubes aligned with the flow, the second pitot tube was placed at angles of 10, 20, and 30° with respect to the flow to check the variation of the pressure coefficient with the yaw angle. The corresponding deviations of the meniscus were 13.8, 8.3 and 3.6 mm respectively. The corresponding velocities at the tip of probe (with the probe removed) were 2.62, 2.46 and 2.3 m/s respectively. Measurements for larger angles of attack were avoided, in view of anticipated errors due to the effect of the wall and to the blockage of the flow by the tube. Measurements with the same tube were performed in a low-turbulence wind tunnel to compare the yaw sensitivity at low and high Reynolds numbers.

Chapter 7

Analysis

7.1 Cavity Flows

7.1.1 Vortex size and position of separation streamline variations with respect to the Reynolds number

From the photographs taken by Tavoularis et al. (1985) in the towing tank, and from photographs taken in the present experiment, some separation streamlines corresponding to different Reynolds numbers are traced in Figure 38. This Figure shows that the flow reattaches at a larger distance from the vertical wall of the cavity when the Reynolds number is increased. The dotted lines represent the portions of the separation lines which could not be seen clearly from the photographs but were extrapolated and are subject to higher uncertainty. From kinematic considerations, the flow should reattach normal to the wall at a point of stagnation. This could not be observed from the photographs. From the photographs it is also clear that the dividing streamline starts below upper the corner of the cavity, especially at the lower Reynolds numbers.This was also observed numerically by Shen and Floryan (1985) and experimentally by Taneda (1979) for rectangular cavities.

In Figure 39 (from Tavoularis et al.(1985)), it can be seen that L_V, the distance

from the center of the vortex to the vertical wall of the cavity, H_V, the height of the center of the vortex with respect to the inside corner of the cavity and L, the distance along the inclined wall of the cavity at which reattachment of the flow occurs, increase with increasing the Reynolds number.

Intuitively, one would expect that, Theoretically as the Reynolds number goes to zero, the flow should not separate but follow the contour of the cavity. However, numerical and experimental evidence point to the formation of a small vortex, even as $Re \rightarrow 0$.

7.1.2 Vortex size and position of separation streamline variation with respect to angle of attack

From the photographs taken for the flow of glycerine past the cavity at different angles of attack, the lines of reattachment for different angles are traced in Figure 40. it is found that H_V, L_V and L decrease for a negative angle of attack and increase for positive angle as shown in Figure 41.

The photographs also suggest that the flow separates further down on the vertical wall for smaller angles of attack.

7.1.3 Streamline determination

From the LDA measurements, an attempt was made to calculate and draw the streamlines for the second cavity. Figure 42 shows these streamlines for Reynolds numbers of 0.62 and 624. Comparing the two figures it is clear that the vortex inside the cavity is bigger for larger Reynolds number. The numbers on each streamline represent the value of the streamfunction, where the value 0 was assigned to the separation streamline and the negative values correspond to the vortex within the cavity.

7.1.4 Influence of scales on wing performance

One of the objectives of this study was to try to explain the reasons of the lift increase by the scales presence on the butterfly's wing. From the obtained results no satisfactory explanation could be found. However, the flow structure inside the cavity at low Reynolds numbers, leads to a wall shear stress orientation as shown in Figure 43 which suggests that the overall resultant shear force on the cavity have an upward vertical component contributing to the lift.

7.2 Performance of Pitot Tubes in Low Reynolds Number Flows

7.2.1 Variation of the pressure coefficient with the Reynolds number

The pressure coefficient is defined as

$$C_p = \frac{P_0 - P_s}{\frac{1}{2}\rho U^2} \tag{7.1}$$

where $P_o - P_s$ is the measured total-static pressure difference for the pitot tube, ρ is the density of the working fluid and U is the velocity measured at the location of the stagnation hole of the pitot tube measured by the LDA after removing the pitot tube from the test section.

The Reynolds number is defined as

$$Re = \frac{UD_e}{\nu} \tag{7.2}$$

where D_e is the external diameter of the pitot tube and ν the kinematic viscosity of the fluid.

The lowest Reynolds numbers for which C_p was determined experimentally was reached by Hurd (1953) who found $C_p = 6.6$ for $Re = 0.9$ and approximated C_p

values for $Re < 1$ by the asymptotic curve $\frac{5.6}{Re}$. In the present investigation we tried to focus our attention on the so far unexplored range of very small Reynolds numbers. The pressure difference sensed by the tow liquid pressure is given by $P_o - P_s = (\Delta\rho)g(\Delta h)$, where $\Delta\rho$ is the density difference between the two liquids used, namely red gauge oil and glycerine, and is equal to $430kg/m^3$. The pressure coefficient C_p was determined for flows at Reynolds numbers of 0.124 and 0.147 to be equal to 30.2 and 29.1 respectively.

Figure 44 shows the results obtained from the present experiments along with the results obtained in some previous experimental and theoretical investigations.

7.2.2 Variation of pressure coefficient with yaw

When pitot tube 2 was yawed relative to the flow direction, it was found that, for a 10° angle, Re=0.118 and $C_p = 25.3$; for a 20° angle, Re=0.111 and $C_p = 17.3$ and for a 30° angle, $Re = 0.104$ and $C_p = 8.6$. The results are shown in Figure 45 along with the results for high Reynolds numbers. These results confirm the well known fact that misalignement of the tube axis with the flow direction causes a decrease in the value of C_p. It is also clear that the effect of misalignement of the tube is much stronger at low Re. This increase of yaw sensitivity is higher than could be attributed to the small decrease in Re due to non-uniformity of the velocity profile in the liquid channel or to blockage.

7.2.3 Disturbance caused by insertion of pitot tube

Figure 46 shows the velocity profiles inside the test section before and after insertion of the pitot tube for one small and one large Reynolds numbers. For lower Reynolds numbers the disturbance is more widespread.

Figures 47 and 48 show two-dimensional "streamline" patterns for two different Reynolds numbers. These "streamlines" might be slightly different from the actual ones representing three-dimensional flow past the tube, because they were computed by integrating the vertical profiles of the velocity, based on the assumption that the flow at the plane of symmetry of the pitot tube is approximately two-dimensional. However, they are included here just for the purpose of comparison for different Reynolds numbers.

These streamlines were determined here from the conservation of mass by integrating the horizontal velocity vectors.

In Figure 49 the velocities are nondimensionalized with respect to the free stream velocities and the resulting streamlines are shown in the same Figure for one low and one large Reynolds numbers. For the lower values of Reynolds numbers it is clear from figures 47, 48 and 49 that the streamlines diverge by a larger distance and the disturbance due to the pitot tube is more critical. It can also be noticed that the streamlines above the pitot tube diverge more than the ones below it. This is due to the blockage caused by the stem. The blockage of the flow by the stem can also be seen in Figure 46 showing the velocity profiles, it is also clear that this effect is more critical for lower Reynolds numbers.

Chapter 8

Conclusions

The main conclusions of the present thesis could be summarized as follows.

(a) The liquid channel and the instrumentation developed and used for this study proved to be very suitable for low Reynolds number experimental investigations.

(b) The obtained flow visualization and LDA measurements for the flow over asymmetric cavities provided substantial qualitative and quantitative information for this type of flow.

(c) Increasing the Reynolds number of the flow causes an increase in the size of the recirculation vortex inside the cavity.

(d) Increasing the angle of attack at low Re causes a slight increase of the recirculation vortex sizes.

(d) The experimentally determined pressure coefficients for the low Reynolds number range agree reasonably well with some of the theoretically previously determined values, for flows past spheres.

(e) Increasing the angle of attack of the pitot tube with respect to the flow, causes the pressure coefficient to decrease. The decrease in pressure coefficient is larger for lower Re than for higher Re.

(f) The disturbance of the flow caused by the insertion of a pressure probe is very critical for low Reynolds numbers flows.

References

Adrian, R.J. and Earley, W.L., 1976 Evaluation of LDV performance using Mie scattering theory. Proc. of the Minnesota Symp. on Laser Anemometry 54, 426.

Amara, M. and Destuynder, P., 1981 A numerical method for the biharmonic problem. Intern. J. Nume. Meth. Eng. 17, 1515.

Aubrey, P., 1986 Design and Construction of a Closed-circuit Tunnel for Low Reynolds Number Tests. Coop Project Report, University of Ottawa, Ottawa, Canada.

Barker, M., 1922 On the use of very small pitot tubes for measuring wind velocity. Proc. Roy. Soc. 97, 413.

Batchelor, G.K., 1954 The skin friction on infinite cylinders moving parallel to their length. Quart. J. Mech. 7, 179.

Buckholz, R.H., 1986 The functional role of wing corrugations in living systems. J. Fluid. Eng. 108, 93.

Burggraf, O.R., 1965 Analytical and numerical studies of the structure of the steady separated flows. J. Fluid Mech. 24, 113.

Christopher, J.C.R., 1975 Aerodynamic properties of an insect wing section and a smooth aerofoil compared. Nature 258, 141.

Drain, L.E.,1980 The Laser Doppler Technique. John Wiley and Sons, Great Britain.

Durrani, T.S. and Greated, C.A., 1977 Laser Systems in Flow Measurement. Plenum Press, New York.

Durst, F., Melling , A. and Whitelaw, J.H., 1981 Principles and Practice of Laser Doppler Anemometry, Second edition. Academic Press, London.

Fleryan, J.M., 1983 Conformal-mapping-based coordinate generation method for channel flows. J. Comp. Phys. 58, 229.

Fox, R.W. and McDonald, A.T., 1985 Introduction to Fluid Mechanics, Third edition. John Wiley and Sons 1985, New York.

Gupta, M.M., Manahar, R.P. and Noble, B., 1981 Nature of viscous flows near sharp corners. Computers and Fluids 9, 379.

Hoover, J.L., 1977 Vill Doo. Model Airplane News. August 1977, 34.

Homman, F., 1952 The effect of high viscosity on the flow around a cylinder and around a sphere. Nat. Advis. Comm. Aeron. Technical Memorandum 1334.

Hurd, C.W., Chesky, K.P. and Shapiro, A.H., 1953 Influence of viscous effects on impact tubes. J. Appl. Mech. 20, 253.

Imai, I., 1954 A new method of solving Oseen's equations and its application to the flow past an inclined elliptic cylinder. Proc. Roy. Soc. A224, 141.

Kaplun, S., 1957 Low Reynolds number flow past a circular cylinder. J. Math. Mech. 6, 595.

Larocque, G.T., 1983 Viscous Effects on Pitot Tubes at Low Reynolds Numbers. Fourth Year Thesis, University of Ottawa, Ottawa, Canada.

Lippish, A.M., 1971 American Aircraft Modeller. October 1971.

Macmillan, F.A., 1954 Viscous effects on pitot tubes at low speeds. J. Roy. Aero. Soc. 58, 570.

Macmillan, F.A., 1954 Viscous effects on flattened pitot tubes at low speeds. J. Roy. Aero. Soc. 58, 837.

Mikhailova, N.P. and Repik, E.U., 1975 Influence of viscosity on the readings of total head tubes with small velocities of the flow. Izvestiya Akademii Nauk SSSR, Mekhanika Zhidkosti i Goza, No. 1, 136.

Moffat, H.K., 1963 Viscous and resistive eddies near a sharp corner. J. Fluid Mech. 18, 1.

Munson, B.R., Rangwalla, A.A. and Man III, J.A., 1985 Low Reynolds number circular couette flow past a wavy wall. Phys. Fluids 28, 2679.

Nachtigall, W., 1967, Aerodynamische Messungen an Tragflü gelsystem segelnder Schmetterlinge. Zeit. Vergl. Phys. 54, 210.

Nachtigall, W., 1974 Insects in Flight. McGraw-Hill, New York.

Newman, B.G., Savage, S.B. and Schatella, D., 1977 Model tests on a wing section of an Aeschna Dragonfly; Scale Effects on Animal Locomotives. Pedley, T. Academic Press, 445.

O'Brien, V., 1982 Viscous flow in an annulus with a sector cavity. ASME J. Fluid Eng. Paper No. 82-WA/FE-5.

Odell, G.M. and Kovaszany, L.S.G., 1971 A new type of water channel with density stratification. J. Fluid Mech. 50, 535.

O'Neil, M.E., 1981 Small particles in viscous medium. Sc. Prog. 67, 149.

Oseen, C.W., 1910 Ueber die Stokessche Formel und über eine verwandte Aufgabe in der Hydrodynamik. Ark. Mat. Astr. Fys. 6, 175.

Pan, F. and Acrivos, A., 1967 Steady flows in rectangular cavities. J. Fluid Mech. 28, 643.

Ratkowsky, D.A. and Rotem, Z., 1968 Viscous flow in a rectangular cut- out. Phys. Fluids 11, 2761.

Rosenhead, L.,1966 Laminar Boundary Layers. Second edition, Oxford University Press 1966, London.

Shen, C. and Floryan, J.M., 1985 Low Reynolds number flow over cavities. Phys. Fluids 28, 3191.

Stokes, G.G., 1851 On the effect of the internal friction of fluids on the motion of pendulum. Trans. Camb. Phil. Soc. 9, 8.

Sturge, L.D., 1986 Stokes flow in a two dimensional cavity with moving end walls. Phys. Fluids 29, 1731.

Takematsu, M., 1966 Slow viscous flow past a cavity. J. Phys. Soc. of Japan 21, 1816.

Taneda, S., 1979 Visualization of separating Stokes flows. J. Phys. Soc. Japan 46, 1935.

Taylor, G.I. 1960 Aeronautics and Astronautics. Hoff, N.J. and Vincenti, W.G., Oxford.

Tavoularis, S., Goldman, A. and Floryan, M.M., 1985 Separation and reattachment in flows over asymmetric cavities at small Reynolds numbers. Proc. Appl. Mech., 10.

Tittley, L., 1985 Design of a Closed Circuit Channel for Low Reynolds Number Tests. Fourth Year thesis, University of Ottawa, Ottawa, Canada.

Weiss, R.F. and Florsheim, B.H., 1965 Flow in a cavity at low Reynolds number. Phys. Fluids 8, 1631.

Table 1: Velocity measurements (in mm/s) for flow in and above cavities.

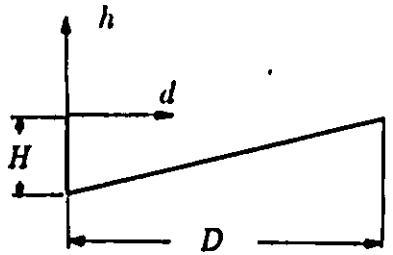

$d^* = \frac{d}{D}$ $h^* = \frac{h}{H}$

Horizontal velocities in cavity 1 for Re=0.62

h^* \ d^*	.04	.07	.11	.15	.19	.22	.26	.30	.33	.37	.41	.44	.48	.52	.56	.59	.63	.67	.70	.74	.78	.81	.85	.89	.93	.96	1.00
3.70			40.0			40.0			40.0			40.0			40.2			39.8			40.2			37.0			40.7
2.95			37.2			37.8			37.5			37.6			38.2			37.3			37.8			33.5			39.0
2.22			32.5			33.2			32.9			32.6			32.7			32.6			33.2			29.0			34.4
1.47			25.5			26.1			26.0			26.0			26.1			25.9			26.9			25.1			28.7
.74			16.0			17.1			17.2			17.6			17.6			17.3			17.0			16.0			19.5
0.00	3.7	3.4	4.3	6.2	6.6	7.3	7.7	8.0	8.1	8.3	8.2	8.3	8.3	8.0	8.0	7.6	7.4	7.2	6.9	6.6	5.6	5.6	5.2	3.4	3.2	3.1	
-.09	1.8	2.3	3.3	4.9	5.5	6.2	6.7	6.9	7.0	7.2	7.1	7.2	7.1	7.0	6.7	6.3	6.1	5.9	5.4	5.0	4.1	4.3	4.6				
-.18	-.71	1.3	2.3	4.0	4.6	5.1	5.6	5.8	5.9	6.0	6.0	6.0	5.9	5.7	5.3	5.0	4.7	4.4	4.4	4.4							
-.28	.31	.73	1.5	2.9	3.5	4.1	4.6	4.9	5.0	5.0	4.9	4.8	4.7	4.5	4.1	4.2	4.1										
-.37	.06	.35	.89	2.2	2.7	3.3	3.7	3.9	3.8	3.9	4.0	3.8	4.0	4.1													
-.46	0.0	.11	.44	1.4	1.9	2.5	2.7	2.9	2.9	3.3	3.6																
-.55	-.12	0.0	.29	.93	1.4	1.8	2.2	2.6																			
-.64	-.05	-.13	-.54	.60	1.2																						
-.74	-.05	-.05																									

Vertical velocities for cavity 1 at Re=0.62

	.04	.07	.11	.15	.19	.22	.26	.30	.33	.37	.41	.44	.48	.52	.56	.59	.63	.67	.70	.74	.78	.81	.85	.89	.93	.96	1.00
3.70			1.3			.14			.30			.60			.90			1.0			1.0			1.0			.96
2.95			1.0			.11			.23			.60			.77			.85			.81			.83			.37
2.22			.46			.34			.10			.39			.83			1.0			.98			.85			.10
1.47			-.63			-.63			-.24			.46			.10			1.3			.12			.93			0.0
0.74			-1.7			-1.1			-.40			.58			.12			1.4			1.9			1.1			.30
0.00	-1.2	-1.6	-1.6	-1.3	-1.1	-.67	-.40	-.13	.10	.31	.52	-.56	.73	.75	.77	.77	.79	.33	.44	.37	.33	.19	0.0	0.0	0.0	0.0	
-.09	-.57	-1.4	-1.5	-1.1	-.86	-.57	-.24	0.0	.21	.42	.52	.60	.64	.69	.71	.60	.60	.29	.21	.15	0.0	-.11	-.11				
-.18	-.18	-.59	-1.0	-.90	-.67	-.36	-.20	0.0	.17	.35	.52	.46	.54	.44	.48	.46	.37	.13	0.0	0.0							
-.28	0.0	-.44	-.61	-.69	-.57	-.30	-.05	0.0	.15	.33	.39	.46	.39	.35	.31	.29	.21										
-.37	.11	-.11	-.36	-.44	-.40	-.20	-.03	0.0	.17	.25	.25	.19	.36	.21													
-.46	.15	.10	-.26	-.36	-.20	-.16	.08	0.0	.11	.21	.21																
-.55	.13	0.0	-.16	-.26	-.11	-.06	.10	.10																			
-.64	0.0	.11	-.11	-.15	0.0																						
-.74	0.0	0.0																									

Table 1 continued ...

Horizontal velocities in cavity 2 for Re=0.62

	.04	.07	.11	.15	.19	.22	.26	.30	.33	.37	.41	.44	.48	.52	.56	.59	.63	.67	.70	.74	.78	.81	.85	.89	.93	.96	1.00
3.70			40.0			40.5			40.2			40.2			40.0			40.2			40.5			40.5			40.0
2.95			37.8			37.5			37.4			37.4			37.4			37.6			37.8			37.6			37.5
2.22			32.9			32.3			32.1			32.1			32.3			32.6			32.9			33.2			32.9
1.47			26.5			26.0			24.7			24.9			26.1			25.4			26.7			26.0			26.3
0.74			16.8			15.6			16.6			16.0			16.1			15.9			15.8			15.3			17.1
0.00	2.3	3.4	4.0	4.7	5.2	5.6	6.0	6.3	6.4	6.6	6.6	6.6	6.4	6.2	5.8	5.6	5.2	4.8	4.3	3.8	3.1	2.5	1.9	1.6	1.6	1.6	
-.09	1.0	2.3	2.9	3.6	4.1	4.6	5.0	5.3	5.4	5.5	5.4	5.3	5.2	4.9	4.6	4.1	3.7	3.2	2.6	2.0	1.4	1.4	1.5				
-.18	.46	.13	2.0	2.8	3.1	3.6	4.0	4.2	4.3	4.3	4.1	4.1	3.9	3.6	3.1	2.8	2.2	1.7	1.7	1.6							
-.28	.21	.77	1.3	1.9	2.4	2.9	3.2	3.4	3.4	3.3	3.2	3.0	2.7	2.4	1.8	1.8	1.7										
-.37	.13	.39	.85	1.3	1.6	2.1	2.3	2.3	2.3	2.3	2.0	2.0	1.8	2.0													
-.46	0.0	.13	.44	.83	1.1	1.4	1.5	1.7	1.4	1.7	1.7																
-.55	-.09	0.0	.23	.42	.66	.94	1.3	1.4																			
-.64	-.05	-.18	0.0	.19	.52																						
-.74	-.01	-.1																									

Vertical velocities for cavity 2 at Re=0.62

	.04	.07	.11	.15	.19	.22	.26	.30	.33	.37	.41	.44	.48	.52	.56	.59	.63	.67	.70	.74	.78	.81	.85	.89	.93	.96	1.00
3.7			3.1			.14			.30			.60			.90			1.0			1.0			1.0			.69
2.95			3.1			.11			.25			.60			.77			.85			.81			.83			.60
2.22			.15			.34			.10			.39			.83			1.0			.94			.85			1.1
1.47			-.94			-.66			-.21			.46			.10			1.39			.12			.93			0.0
0.74			-1.8			-1.3			-.40			.58			.12			1.4			1.9			1.1			.31
0.00	-1.1	-1.6	-1.5	-1.4	-1.1	-.86	-.42	-.18	.11	.31	.44	.64	.71	.67	.60	.56	.56	.68	.50	.42	.37	.23	.05	.11	0.00	-1.56	
-.09	-.51	-1.13	-1.25	-1.11	-.88	-.66	-.40	-.11	.19	.23	.42	.48	.62	.56	.44	.42	.33	.08	.23	.19	0.0	0.0	0.0				
-.18	-.73	-.69	-.90	-.88	-.78	-.49	-.24	0.0	.19	.37	.37	.46	.52	.25	.37	.19	.10	.11	.10	.04							
-.28	-.34	-.34	-.69	-.66	-.53	-.32	-.09	0.0	.10	.23	.33	.42	.31	.33													
-.37	.19	-.18	-.38	-.49	-.42	-.20	-.07	0.0	.19	.25	.31	.31	.27	.25													
-.46	.15	-.15	-.15	-.32	-.15	-.07	0.0	.11	.17	.19	.17																
-.55	.17	0.0	-.05	-.15	-.13	0.0	0.0	.06																			
-.64	-.42	.06	0.0	0.0	-.07																						
-.74	-.06	0.0																									

Table 1 continued ...

Horizontal velocities in cavity 1 for Re=624

	.04	.07	.11	.15	.19	.22	.26	.30	.33	.37	.41	.44	.48	.52	.56	.59	.63	.67	.70	.74	.78	.81	.85	.89	.93	.96	1.00
0.92			57.5			57.1			57.0			56.4			56.2			56.3			58.2			55.8			54.1
0.74			55.8			56.7			59.0			58.8			58.9			54.7			56.4			57.3			52.4
0.55			58.8			58.8			58.0			54.2			57.5			53.4			45.4			52.8			18.4
0.37			58.6			55.1			53.2			47.2			46.7			38.6			43.2			40.0			40.7
0.18			46.7			31.8			26.4			30.3			24.1			20.7			25.1			29.4			30.9
0.00	9.8	8.8	7.6	7.9	8.1	6.9	8.2	6.0	7.5	6.1	6.7	6.3	8.1	6.5	13.2	8.64	6.5	7.8	8.5	10.2	15.1	14.8	17.7	13.3	18.8	20.0	
-.09	.22	.10	-1.4	1.8	1.7	1.6	1.3	1.6	0.0	0.0	2.6	2.4	0.0	2.2	6.8	5.5	1.8	2.5	0.0	4.4	5.9	7.8	15.5				
-.18	-.31	-.75	-.70	-1.1	1.05	-2.7	-1.4	0.0	0.0	-2.1	-3.8	-2.7	-2.9	0.0	0.0	0.0	-2.0	0.0	3.6	1.4							
-.28	-.15	-.27	-1.9	-6.4	-2.6	-8.9	-2.0	-2.9	-1.3	-2.6	-4.4	-3.1	-4.3	-6.4	-2.3	-3.3	-5.5										
-.37	-.29	-.29	-1.0	-1.9	-1.0	-2.5	-4.0	-3.3	-2.0	-1.3	-3.8	-2.6	-1.7	-5.2													
-.46	-.14	-.60	-.68	-.91	-.66	-1.5	-3.5	-2.5	-1.0	-3.1	-2.4																
-.55	-.19	-.64	-.33	-1.7	-1.3	-1.4	-1.6	-1.8																			
-.64	-.19	-.77	-.52	-.95	-.15																						
-.74	0.0	-.23																									

Vertical velocities for cavity 1 at Re=624

	.04	.07	.11	.15	.19	.22	.26	.30	.33	.37	.41	.44	.48	.52	.56	.59	.63	.67	.70	.74	.78	.81	.85	.89	.93	.96	1.00
0.92			-2.8			-1.5			0.0			0.0			1.4			2.2			3.4			1.5			2.5
0.74			-2.7			-1.6			0.0			0.0			1.4			3.4			2.8			2.0			2.3
0.55			-2.4			-1.2			0.0			0.0			0.0			2.0			2.2			3.0			8.3
0.37			-1.73			-.55			0.0			0.0			0.0			3.8			2.8			1.3			0.0
0.18			-.65			-.45			-.23			0.0			0.0			2.07			0.0			0.0			.10
0.00	-1.4	-1.1	-.84	-.93	-.63	-.85	-.67	-.68	-.26	-.34	0.0	0.0	0.0	0.0	0.0	0.0	0.0	1.5	1.8	1.2	0.0	0.0	-.27	-.02	-.57	-.65	
-.09	-1.6	-1.2	-.97	-.71	-.73	-.59	-.39	-.52	-.16	-.20	0.0	0.0	0.0	0.0	0.0	0.0	0.0	0.0	.81	0.0	0.0	0.0	-.55				
-.18	-1.4	-1.1	-.76	-.74	-.72	-.61	-.48	-.34	0.0	-.14	0.0	0.0	0.0	0.0	0.0	0.0	0.0	0.0	.92	.16							
-.28	-1.27	-.80	-.75	-.60	-.50	-.49	-.42	-.25	.14	0.0	0.0	0.0	0.0	0.0	0.0	0.0	0.0										
-.37	-.96	-7.0	-.61	-.44	-.37	-.20	-.06	0.0	.03	0.0	0.0	0.0	0.0	0.0													
-.46	-.66	-.67	-.40	-.24	-.33	-.11	0.0	0.0	0.0	0.0	0.0																
-.55	-.32	-.38	-.28	-.16	-.11	0.0	0.0	0.0																			
-.64	-.35	-.29	-.13	-.01	-.07																						
-.74	-.14	-.20																									

Table 1 continued ...

Horizontal velocities in cavity 2 for Re=624

	.04	.07	.11	.15	.19	.22	.26	.30	.33	.37	.41	.44	.48	.52	.56	.59	.63	.67	.70	.74	.78	.81	.85	.89	.93	.96	1.00
.92			52.7			54.1			51.9			51.8			49.6			50.4			51.3			45.8			45.3
.74			52.7			50.0			46.8			45.1			49.2			46.5			47.2			43.3			45.3
.55			49.7			50.2			43.8			41.9			42.2			41.2			41.5			40.0			11.5
.37			35.1			36.0			40.1			36.9			35.3			36.7			34.0			37.6			41.6
.18			26.6			29.1			33.9			30.9			27.6			24.1			30.9			32.8			35.7
.00	16.2	18.8	19.2	19.7	20.7	22.8	24.8	27.4	22.6	27.1	25.5	27.1	26.4	21.8	23.1	25.3	26.9	26.0	27.7	28.3	28.6	30.0	28.2	30.4	35.6	39.8	
-.09	0.0	1.9	2.5	4.5	10.8	12.7	12.9	16.3	13.0	11.9	11.5	15.6	12.0	17.9	16.9	19.5	18.6	20.0	22.0	22.8	28.9	29.1	30.0				
-.18	1.7	-1.5	0.0	0.0	4.3	5.8	6.8	5.1	6.3	4.7	8.3	6.1	12.1	10.7	13.9	13.0	15.3	17.5	16.6	21.5							
-.28	-2.0	-2.8	-3.6	-2.7	0.0	0.0	0.0	0.0	0.0	0.0	0.0	0.0	4.5	9.1	9.1	11.8	14.2										
-.37	-1.2	-3.8	-2.3	-3.2	-5.0	-4.4	-2.3	-2.6	0.0	0.0	-1.3	0.0	1.3	1.7													
-.46	0.0	-2.3	-2.4	-1.7	-7.0	-5.4	-5.6	-6.4	-7.6	-2.5	-3.0																
-.55	0.0	0.0	-2.3	-1.5	-4.6	-4.1	-8.9	-9.2																			
-.64	.38	0.0	0.0	0.0	-6.7																						
-.74	.32	.21																									

Vertical velocities for cavity 2 at Re=624

	.04	.07	.11	.15	.19	.22	.26	.30	.33	.37	.41	.44	.48	.52	.56	.59	.63	.67	.70	.74	.78	.81	.85	.89	.93	.96	1.00
.92			-3.8			-3.2			-4.1			-4.2			-5.4			-3.8			-2.0			-1.3			-1.3
.74			-1.8			-4.0			-3.6			-5.3			-3.8			-3.3			-1.1			-2.6			-1.4
.55			-3.7			-3.5			-4.0			-5.0			-3.0			-3.1			-1.7			-.99			2.0
.37			-3.2			-3.7			-4.7			-6.1			-3.5			-2.6			-.05			-.81			-.62
.18			0.0			-1.7			-5.9			-3.4			-5.6			-1.9			1.3			.62			1.3
.00	1.3	1.8	2.2	3.9	1.6	1.3	0.0	0.0	0.0	-1.2	0.0	-2.7	0.0	0.0	0.0	0.0	2.9	2.4	3.9	4.7	4.5	4.2	3.8	5.3	6.5	5.5	
-.09	1.0	1.1	0.0	0.0	0.0	0.0	0.0	0.0	0.0	-1.6	-3.0	-2.8	0.0	-.13	0.0	0.0	0.0	4.5	2.9	4.1	4.5	5.8	5.9				
-.18	1.8	1.8	.98	1.0	1.4	0.0	0.0	0.0	-2.2	-1.9	-2.2	-5.0	-2.7	-.90	0.0	0.0	3.3	2.8	2.70	4.17							
-.28	2.5	2.4	2.1	1.9	3.6	0.0	0.0	-3.6	-1.5	-2.4	-2.2	-1.9	0.0	-1.7	6.5	2.2	2.9										
-.37	1.3	2.1	1.6	2.5	2.1	1.4	0.0	0.0	-3.1	-2.4	-3.6	-1.1	-1.1	0.0													
-.46	.34	1.6	1.1	2.2	1.8	1.0	0.0	0.0	-2.9	-2.5	-2.3																
-.55	.32	.36	.73	2.4	1.1	0.0	0.0	-2.3																			
-.64	0.0	.52	.38	.28	.54																						
-.74	0.0	.40																									

Horizontal velocities in cavity 2 reversed for Re=0.62

	.04	.07	.11	.16	.19	.22	.26	.30	.33	.37	.41	.44	.48	.52	.56	.59	.63	.67	.70	.74	.78	.81	.85	.89	.93	.96	1.00
3.70			40.0			46.0			40.1			40.2			40.2			39.6			40.7			40.5			40.2
2.96			37.2			37.6			37.6			37.6			38.2			37.3			37.0			37.6			37.6
2.22			32.6			33.2			32.9			32.6			32.7			32.6			32.6			33.1			33.0
1.47			25.6			26.1			26.0			26.0			26.1			26.9			25.4			26.1			25.9
0.74			16.0			17.1			17.2			17.6			17.6			17.3			16.0			16.6			16.5
0.00	5.1	4.0	4.8	5.3	5.8	6.0	6.4	6.6	6.7	6.7	6.7	6.6	6.6	6.5	6.1	5.8	5.8	6.4	5.0	4.6	4.1	3.8	3.4	3.1	2.7	1.8	
-.09	1.9	2.8	3.7	4.2	4.8	5.1	5.4	5.5	5.7	5.6	5.5	5.5	5.3	5.1	4.8	4.4	4.4	3.9	3.3	2.9	2.7	2.9	2.9				
-.18	.87	1.8	2.7	3.3	3.7	4.1	4.4	4.6	4.6	4.7	4.5	4.3	4.2	4.2	3.8	3.2	3.0	2.5	2.6	2.6							
-.28	3.6	1.1	1.9	2.6	2.8	3.3	3.5	3.6	3.7	3.6	3.4	3.2	2.9	2.8	2.3	2.2	2.6										
-.37	.15	.67	1.2	1.7	2.1	2.4	2.6	2.7	2.7	2.6	2.4	2.1	2.2	2.3													
-.46	0.0	3.1	.79	1.1	1.4	1.6	1.8	1.8	1.8	1.9	2.0																
-.55	-.05	.10	.37	.67	.96	1.1	1.4	1.6																			
-.64	-.03	-.11	.10	.40	.37																						
-.74	-1.1	-1.1																									

Vertical velocities for cavity 2 reversed at Re=0.62

	.04	.07	.11	.16	.19	.22	.26	.30	.33	.37	.41	.44	.48	.52	.56	.59	.63	.67	.70	.74	.78	.81	.85	.89	.93	.96	1.00
3.70			-1.3			-1.1			-.15			-.92			-.80			-.45			-.60			-.70			-.65
2.96			-1.1			-1.0			-.63			-.41			-.17			-.20			-.33			-.66			-.60
2.22			-1.1			-1.0			-.64			0.0			.24			.42			.15			-.40			-.67
1.47			-1.5			-1.2			-.43			.38			.86			.06			.06			.03			-.75
0.74			-2.1			-1.3			-.23			-.67			.96			1.1			1.0			.61			-.62
0.00	2.3	2.0	1.7	1.4	1.1	.73	3.1	0.0	-.18	-.32	-.55	-.63	-.71	-.71	-.75	-.69	-.71	-.61	-.59	-.57	-.47	-.44	-.34	-.20	-.14	-.13	
-.09	1.7	1.7	1.6	1.2	.93	.64	.21	0.0	-.20	-.45	-.49	-.66	-.66	-.66	-.69	-.68	-.69	-.61	-.47	-.44	-.32	-.34	-.20				
-.18	1.1	1.4	1.2	1.0	.76	.62	.13	-.13	-.28	-.47	-.61	-.45	-.49	-.40	-.61	-.47	-.34	-.28	-.36	-.30							
-.28	.62	.10	.95	.83	.64	.37	.11	-.15	-.24	-.32	-.44	-.36	-.44	-.26	-.34	-.22	-.24										
-.37	.33	.79	.79	.56	.39	.27	0.0	-.20	-.16	-.30	-.24	-.26	-.24	-.32													
-.46	0.0	.51	.35	.46	.35	.17	0.0	-.16	-.18	-.26	-.26																
-.55	-.73	.27	.27	.29	.19	.08	-.16	-.15																			
-.64	-.11	0.0	.17	.23	0.0																						
-.74	.06	0.0																									

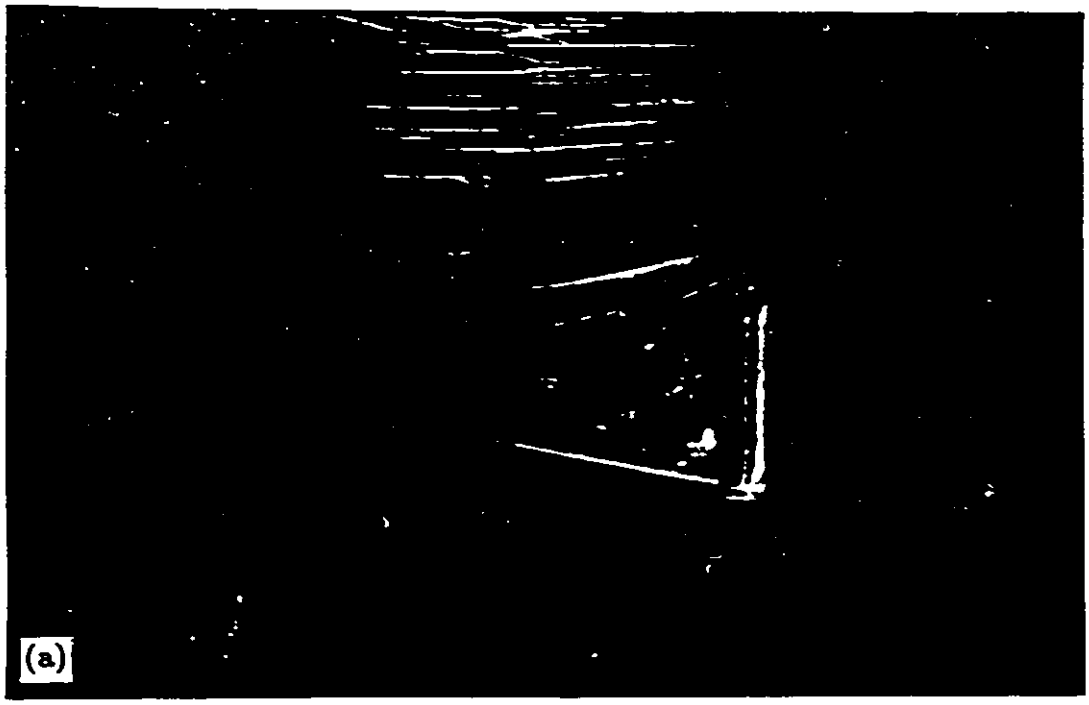

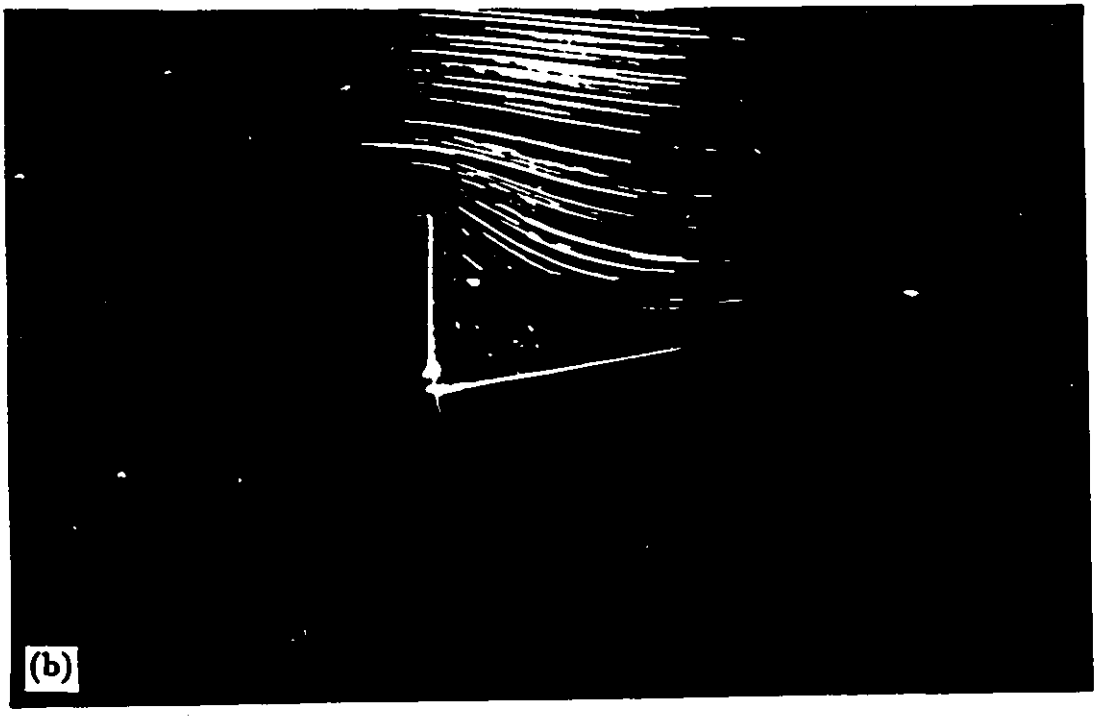

Plate 1

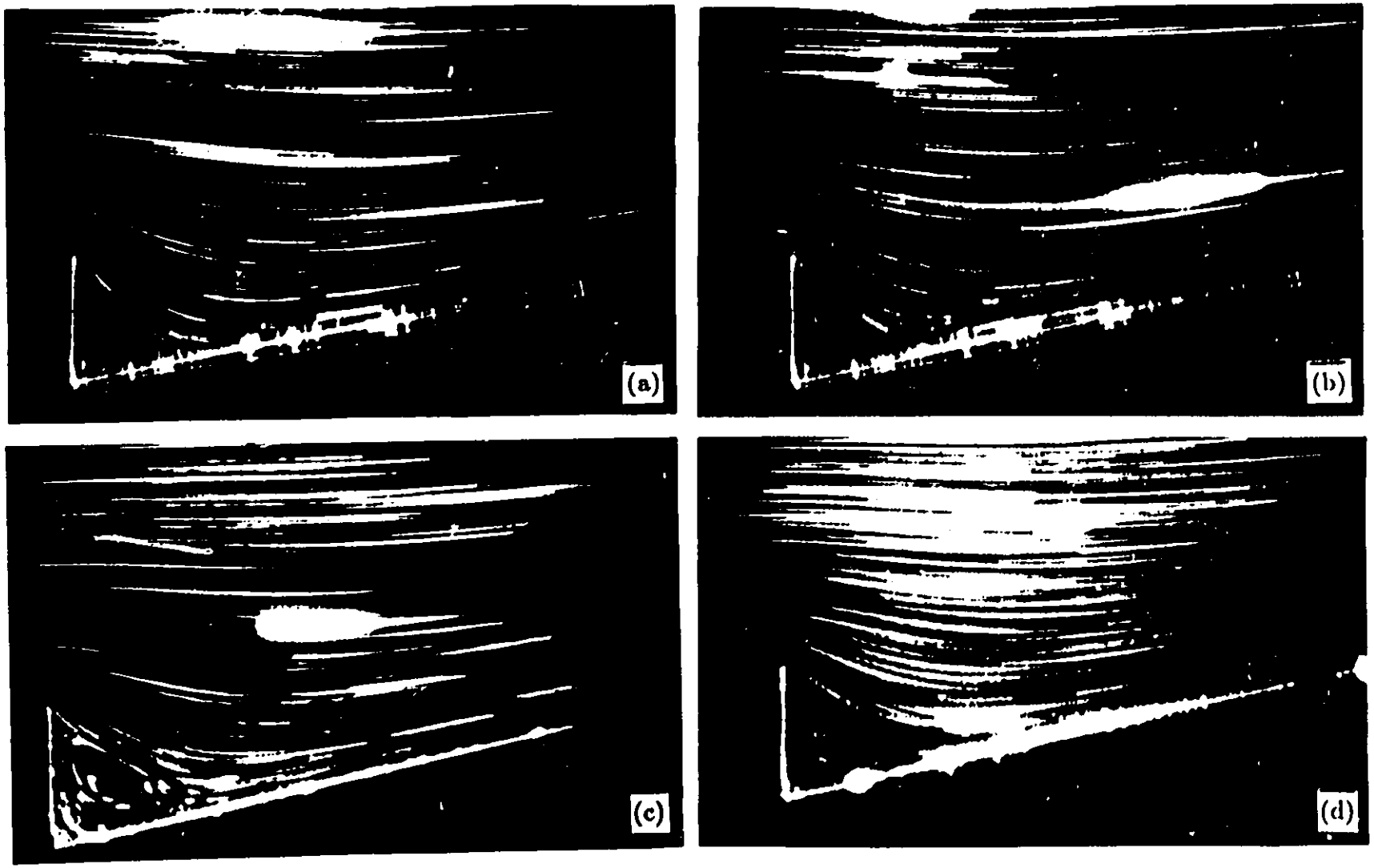

Plate 2

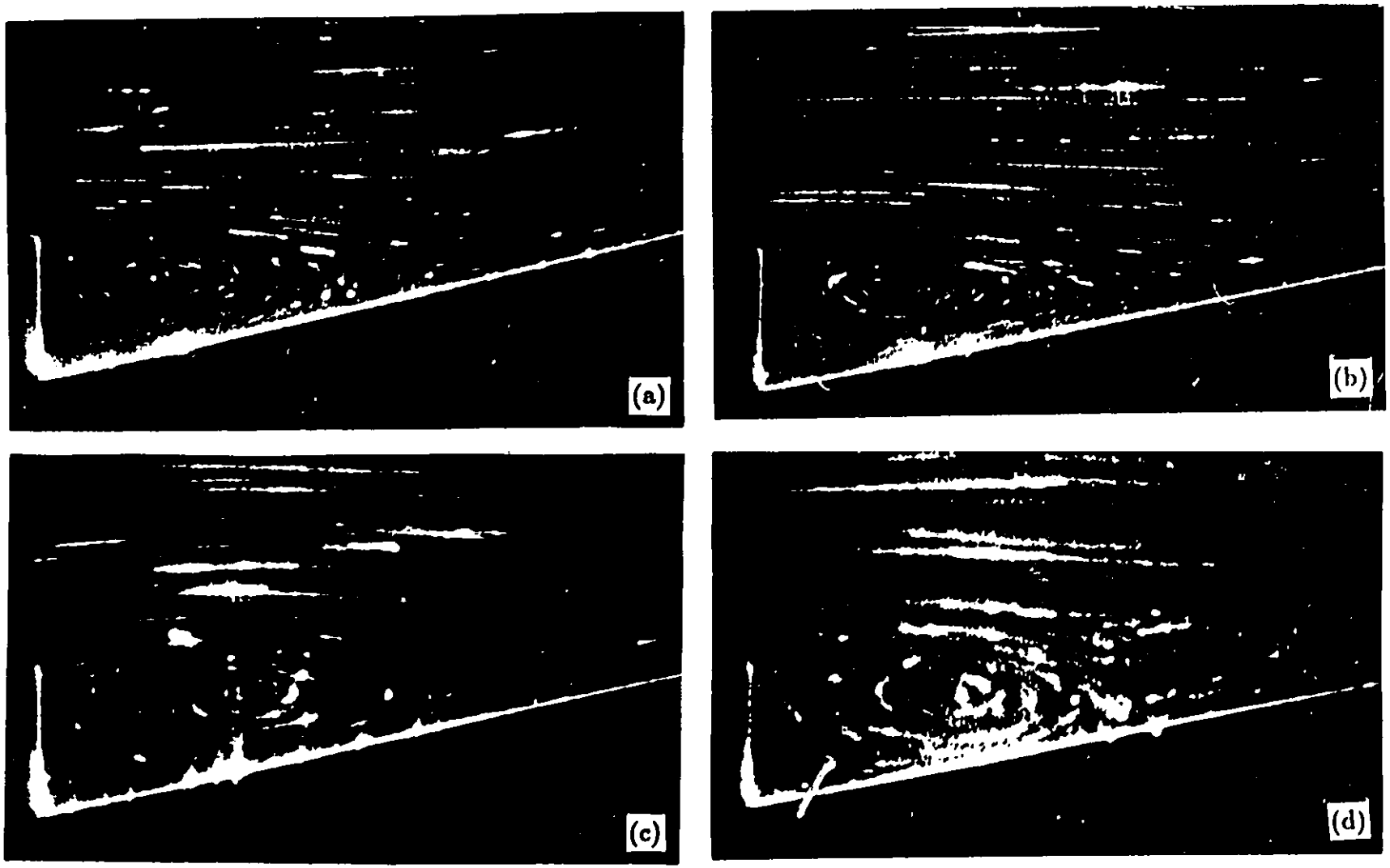

Plate 3

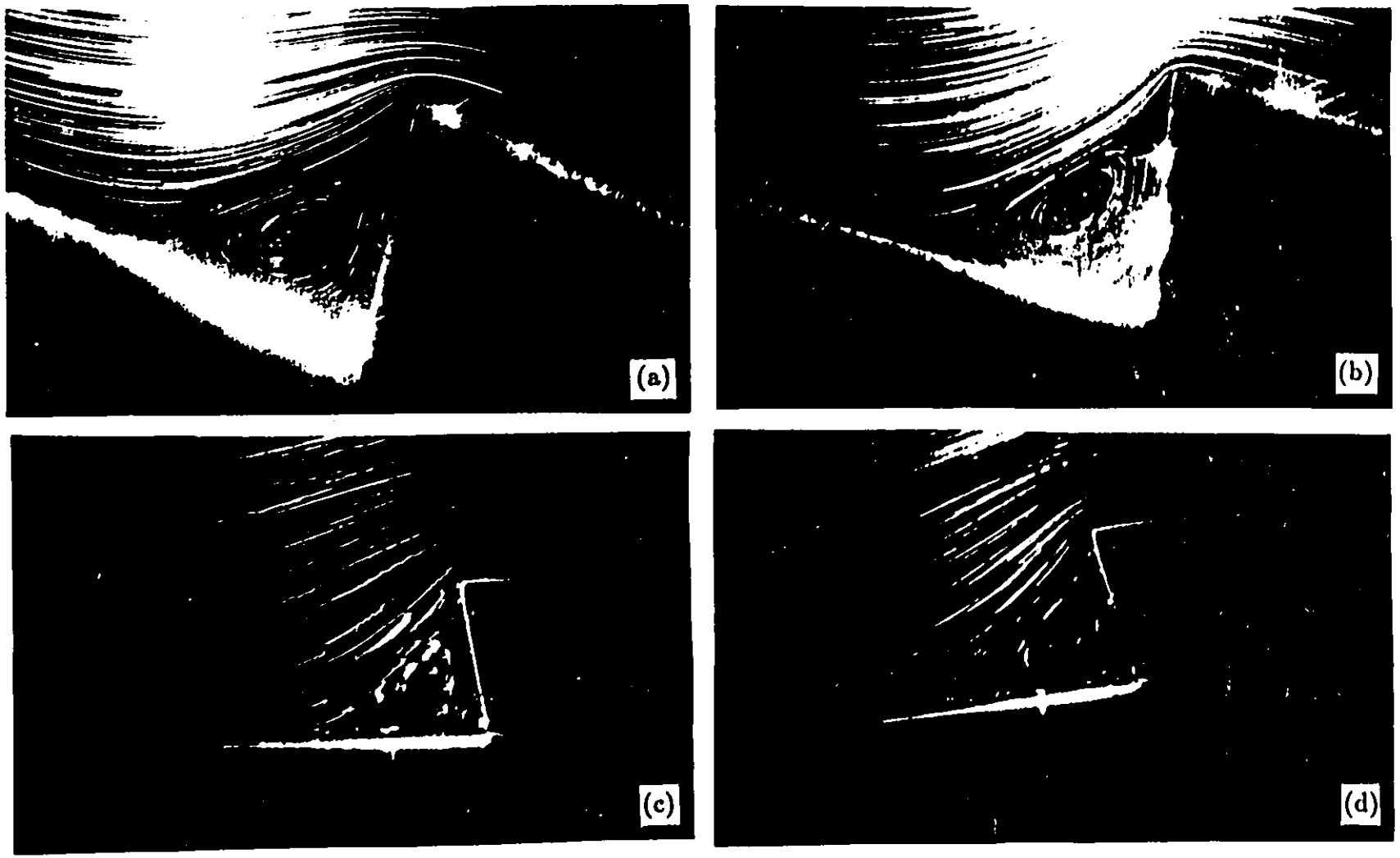

Plate 4

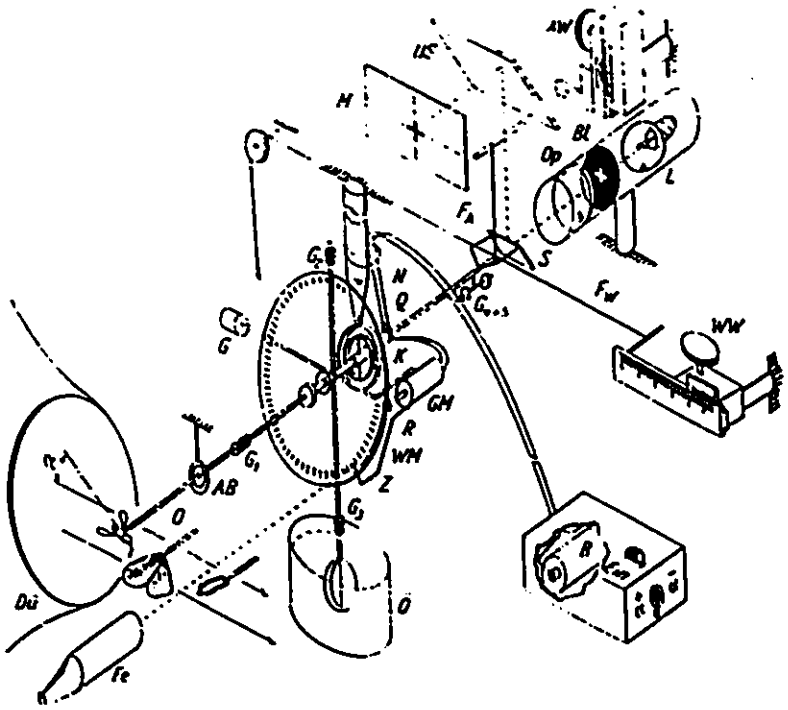

Figure 1: Experimental facility used by Nachtigall(1967) to measure lift and drag on butterfly wings.

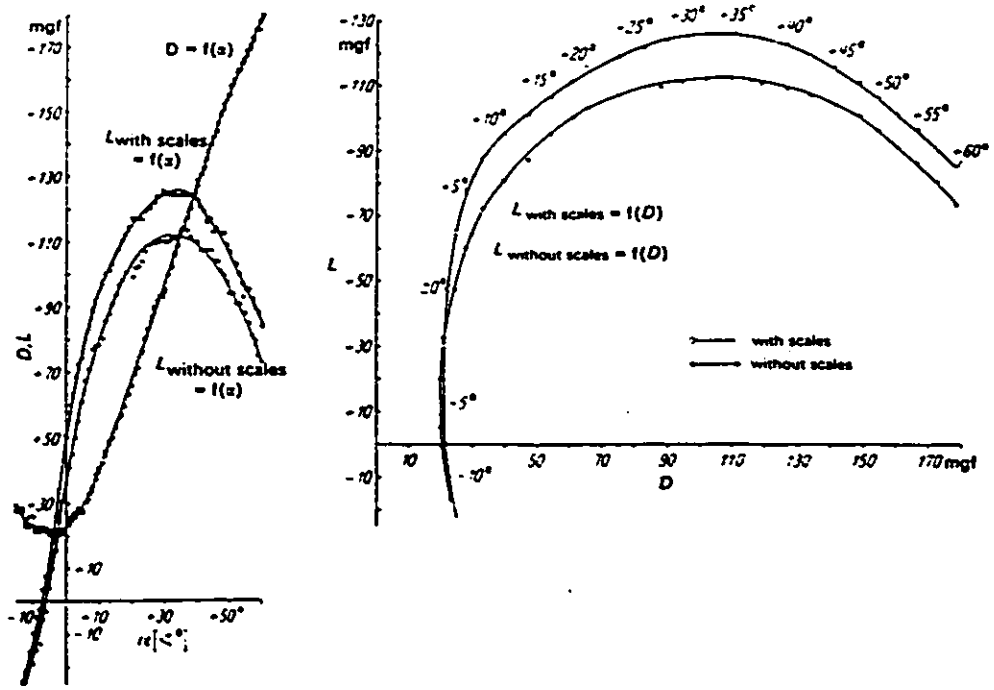

Figure 2: (a)-Lift and drag vs angle of attack measurements for an Agrotis. (b)- Lift and drag polar curves for an Agrotis.(From Nachtigall, 1967).

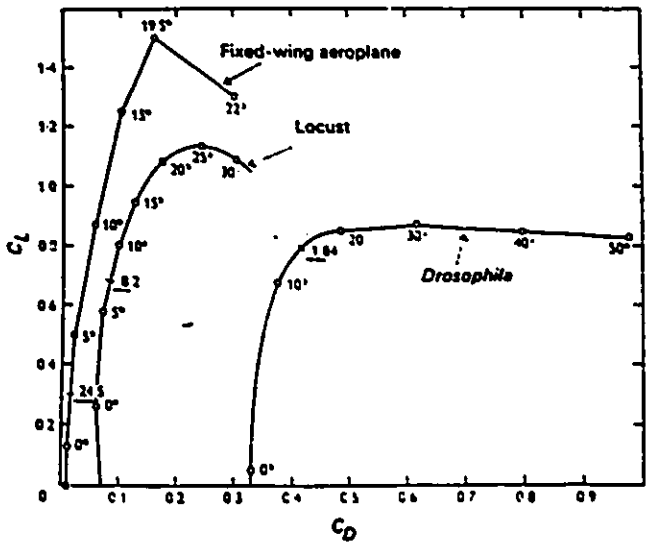

Figure 3: Comparison between lift and drag polar curves for a Drosophila, a locust and an airfoil wing. (From Nachtigall, 1974).

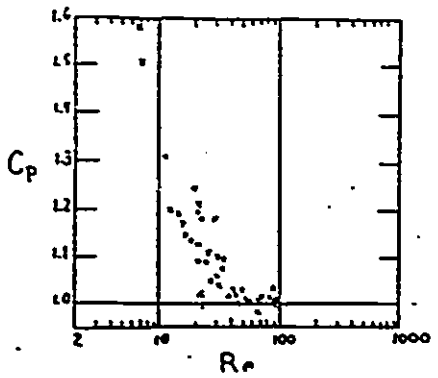

Figure 4: Barker's results.. (From Larocque, 1980).

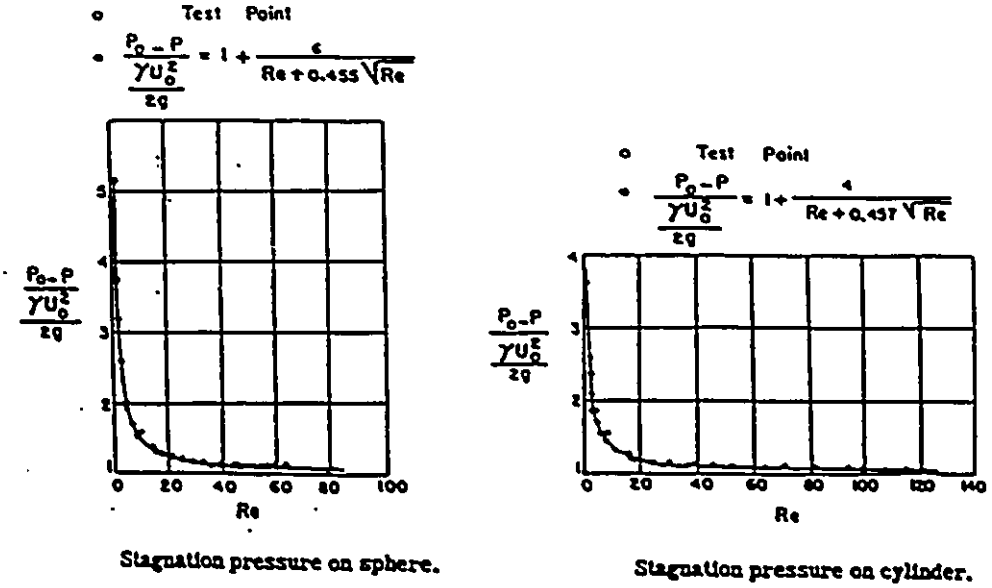

Stagnation pressure on sphere.

Stagnation pressure on cylinder.

Figure 5: Results by Homman (1952).

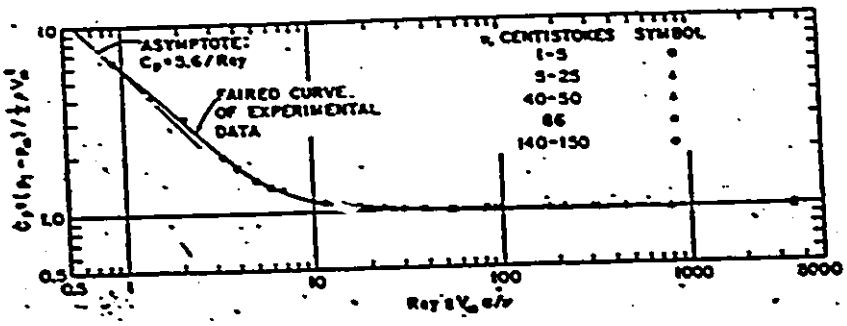

Figure 6: Results by Hurd et al. (1954).

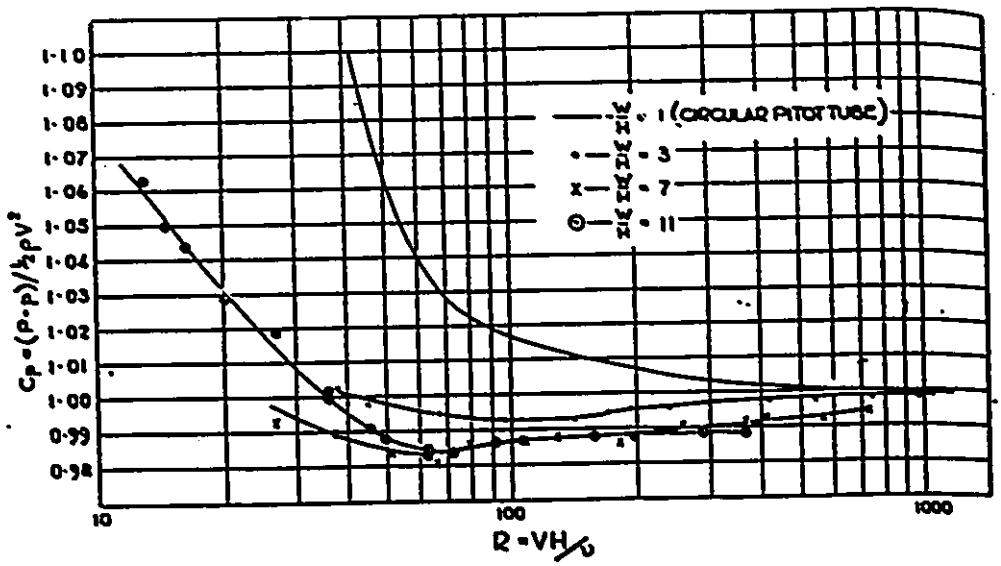

Figure 7: Results by Macmillan (1954 b).

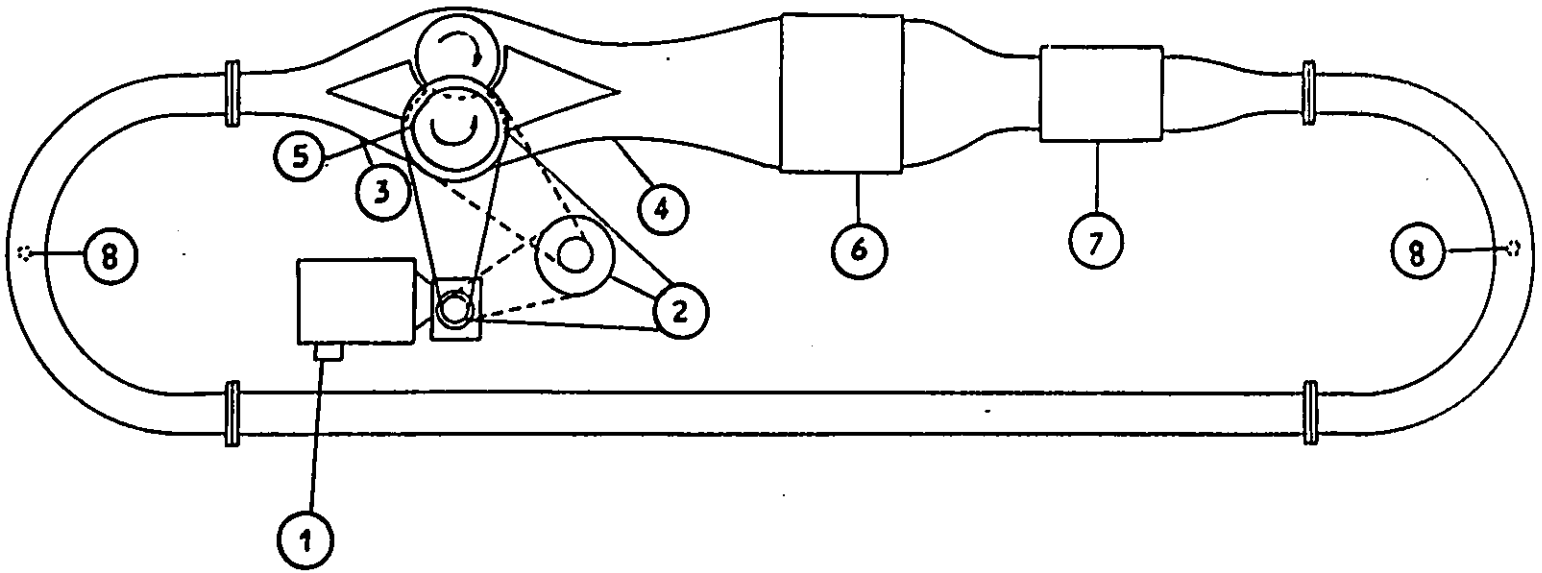

1. motor
2. pulleys
3. inlet diffuser
4. outlet diffuser
5. pump
6. settling chamber
7. test section
8. valves

Figure 8: Liquid channel.

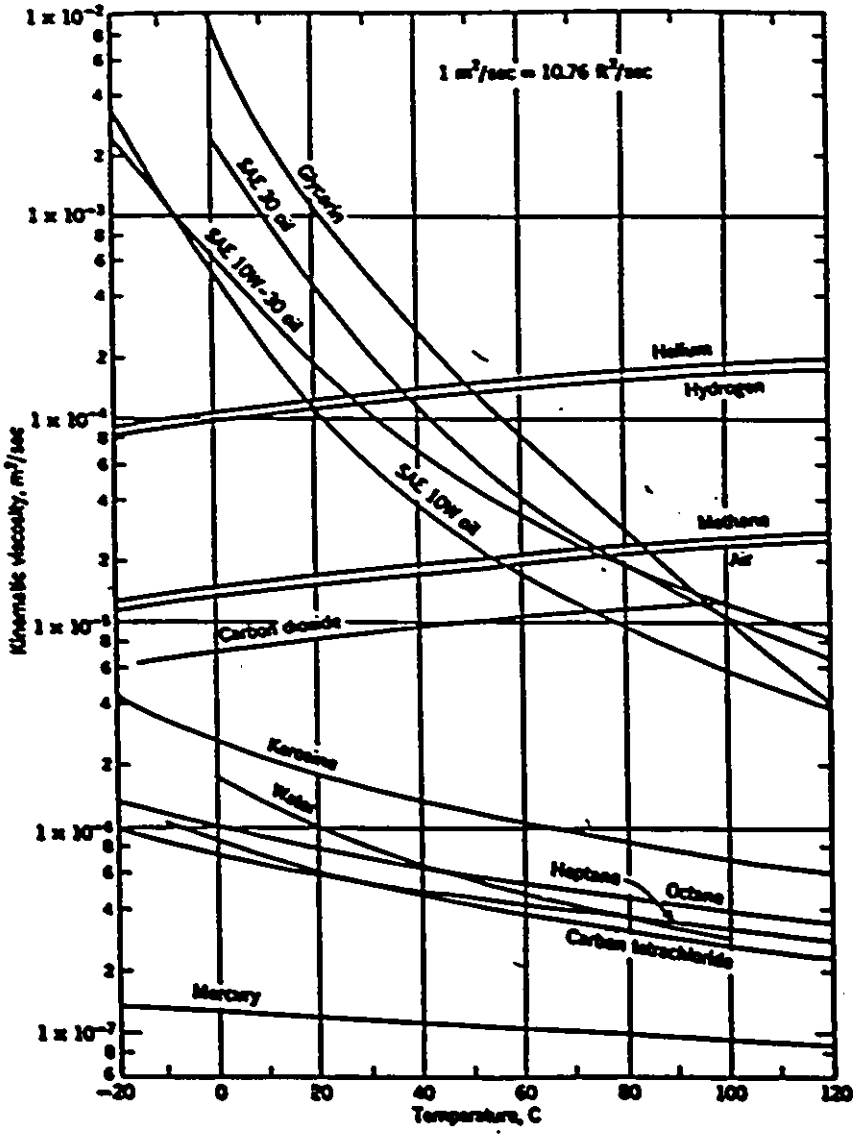

Figure 9: Kinematic viscosity of common fluids (at atmospheric pressure) as a function of temperature. (From Fox and McDonald, 1985).

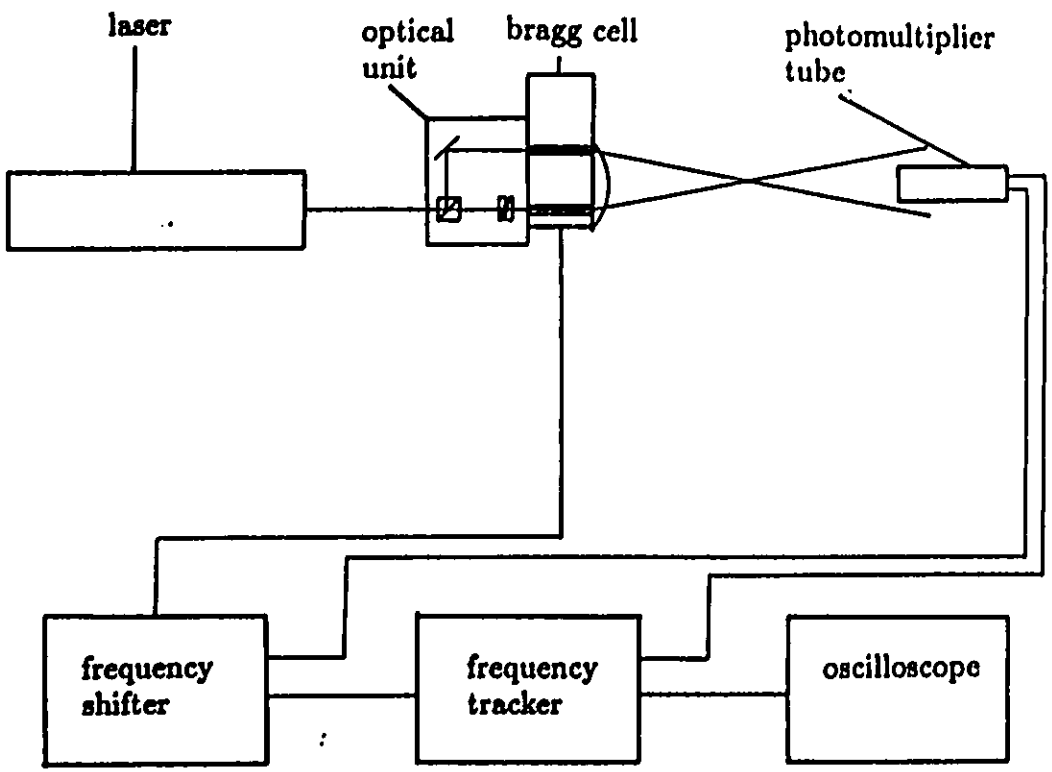

Figure 10: Laser Doppler Anemometry system.

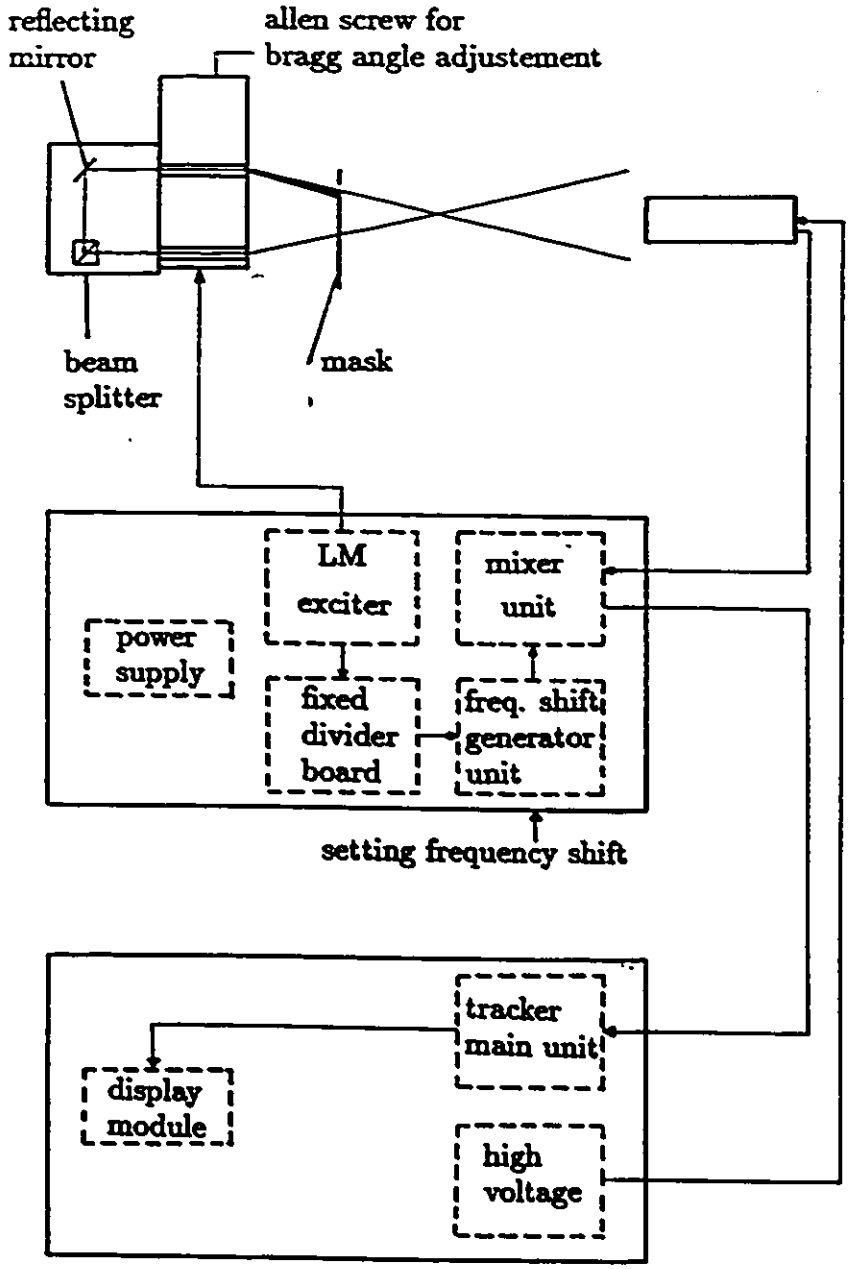

Figure 11: Functional diagram of the LDA.

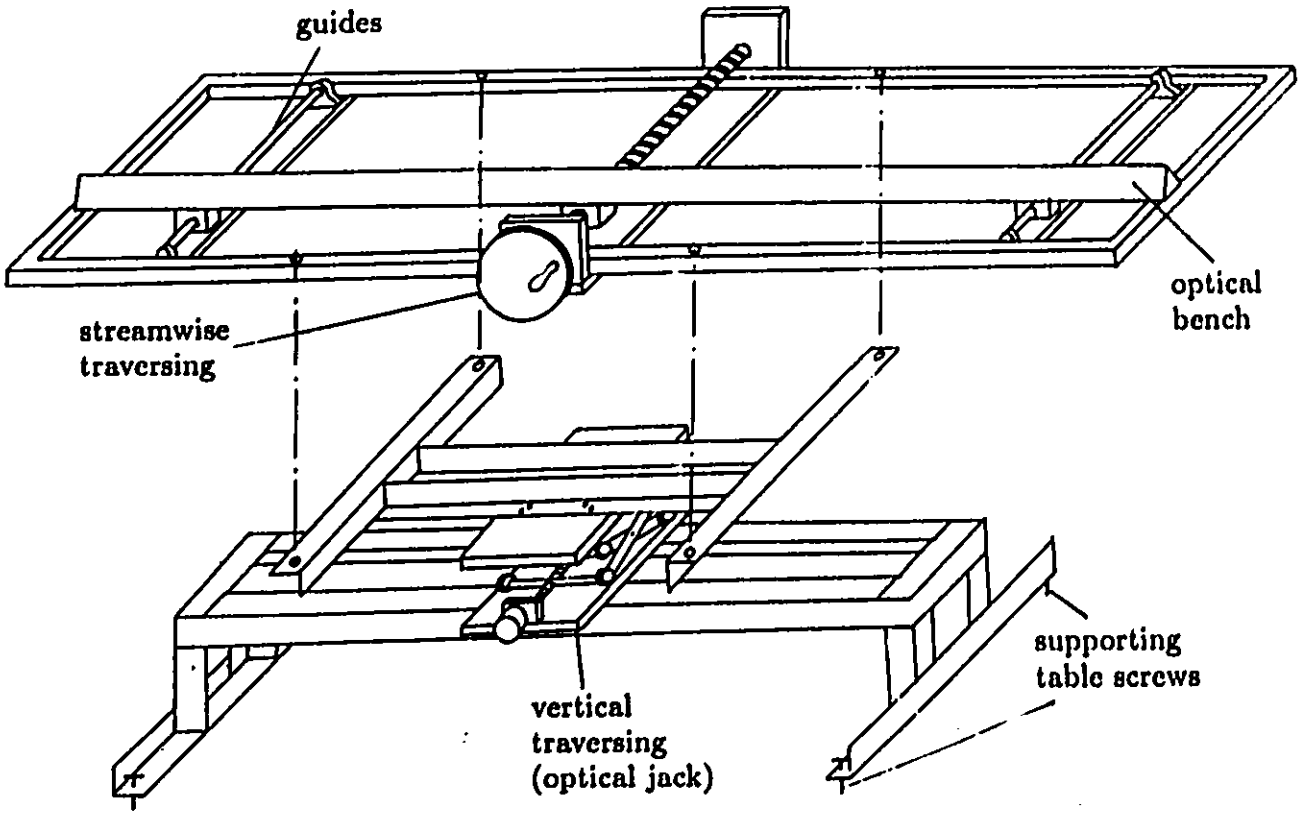

Figure 12: Traversing system.

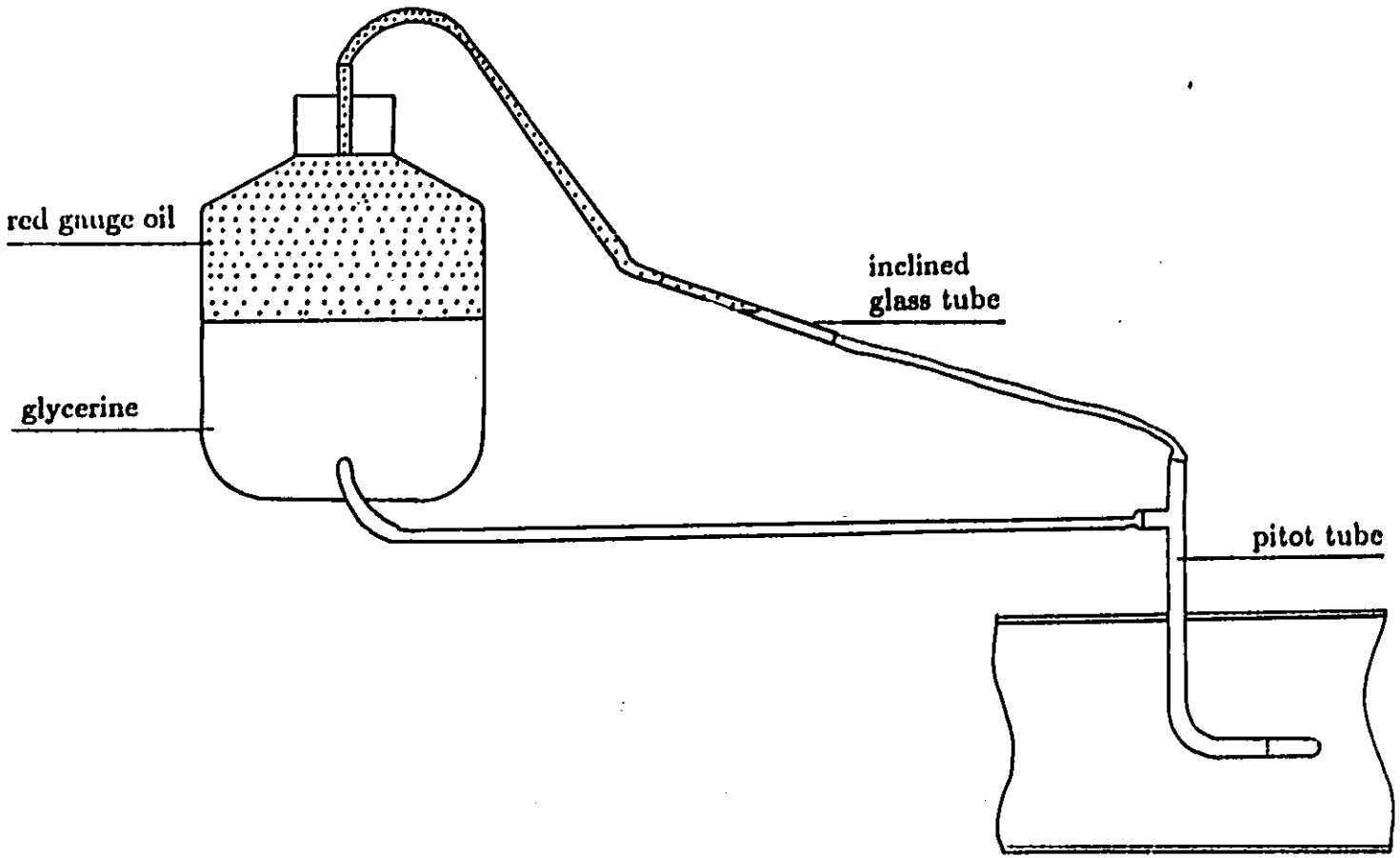

Figure 13:Pressure manometer.

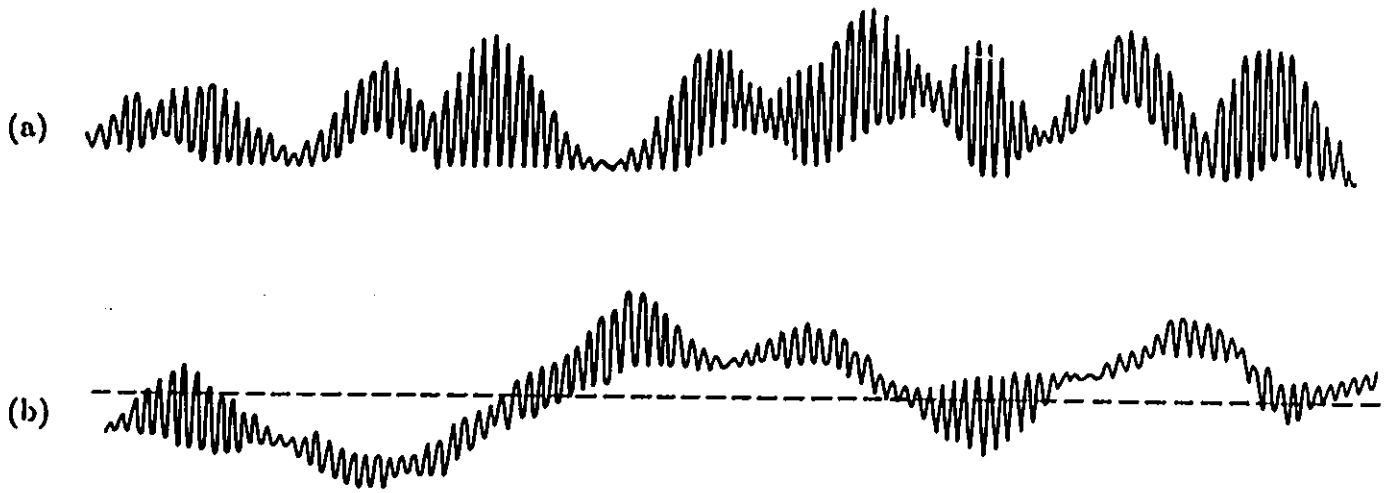

Figure 14: Photomultiplier signal. (a)- One particle present at control volume. (b)- Several particles present at control volume.

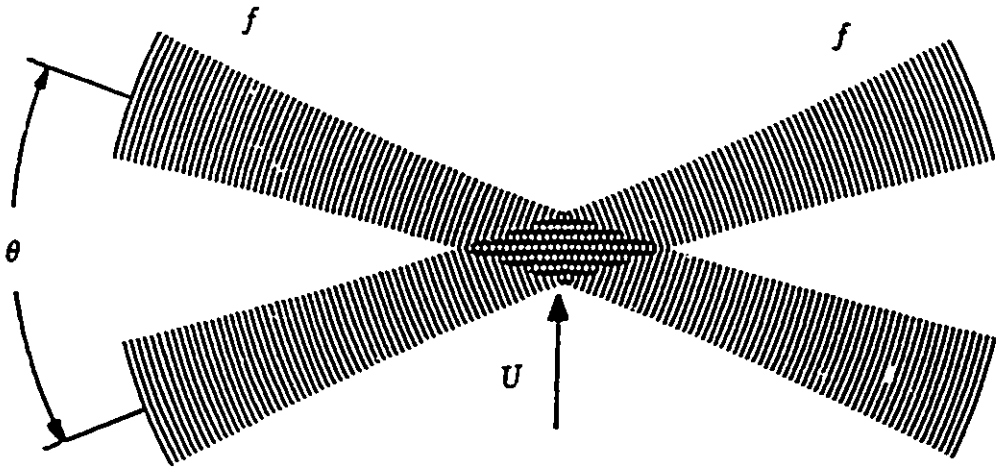

Figure 15: Fringes in beam intersection with no frequency shifting.

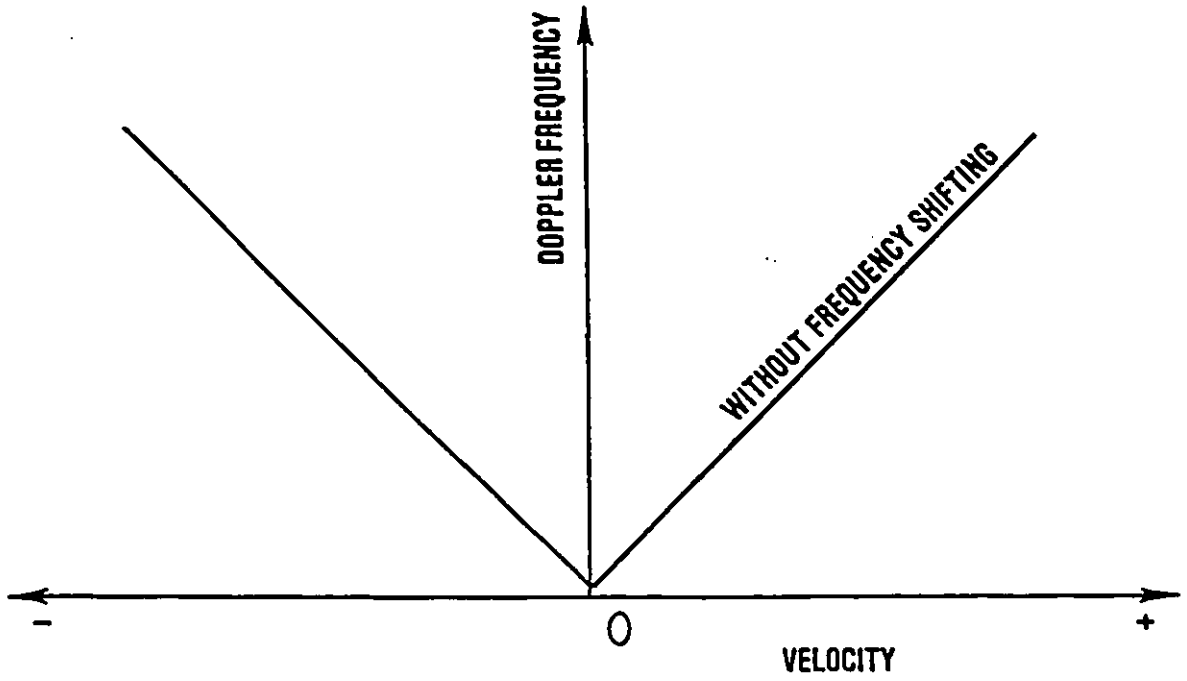

Figure 16: Frequency-velocity curve with no frequency shifting.

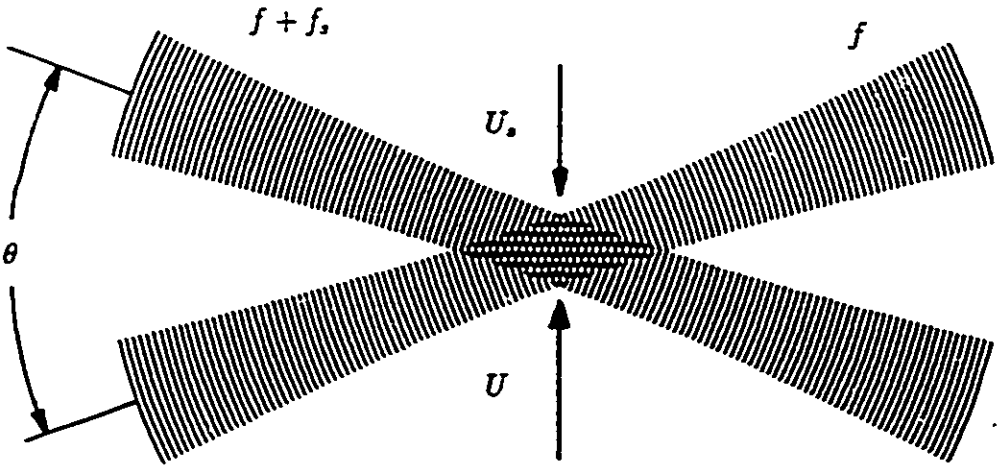

Figure 17: Fringes in beam intersection with frequency shifting

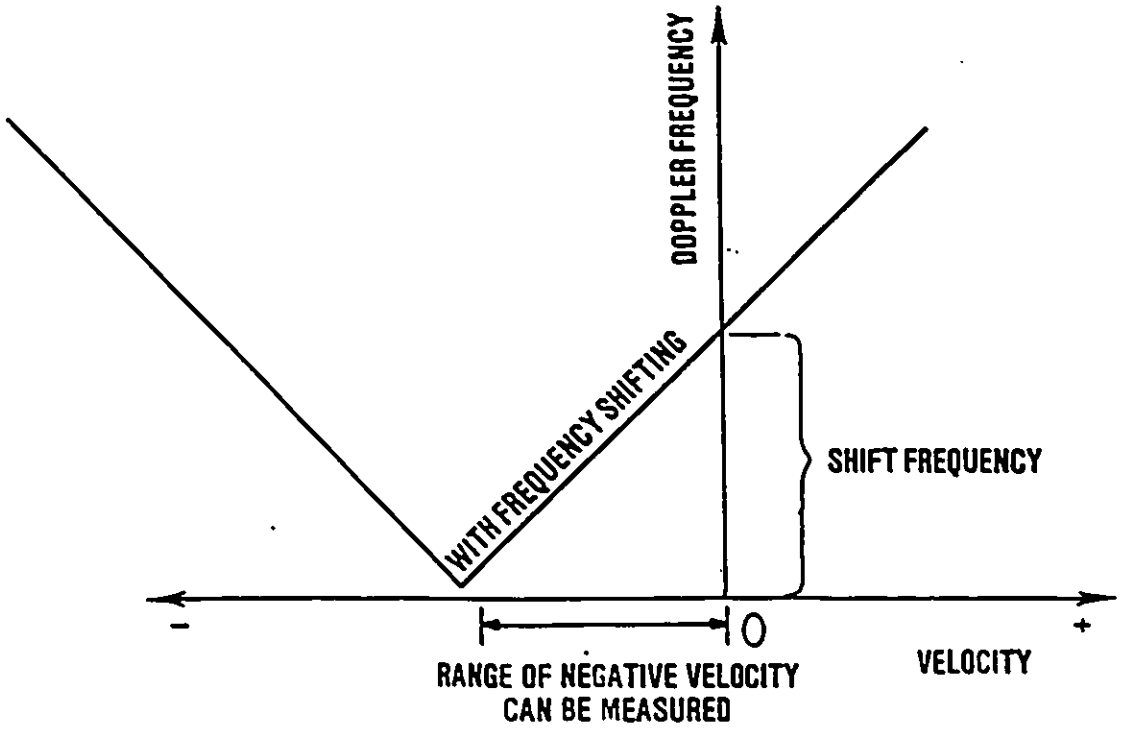

Figure 18: Frequency-velocity curve with frequency shifting.

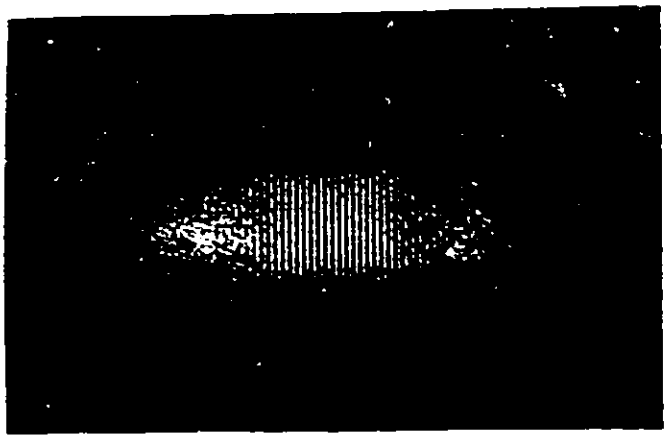

Figure 19: Beam intersection interference stripes.

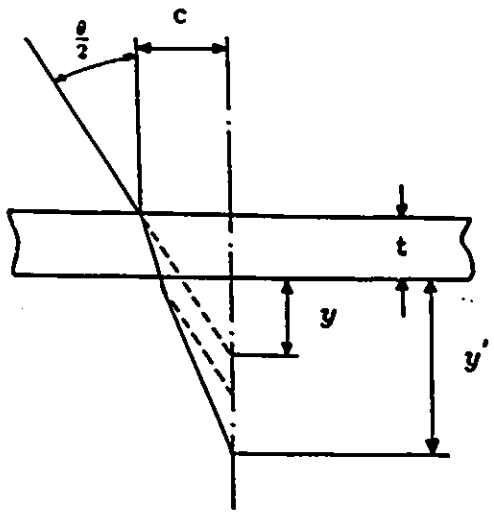

Figure 20: Position change of laser beam intersection.

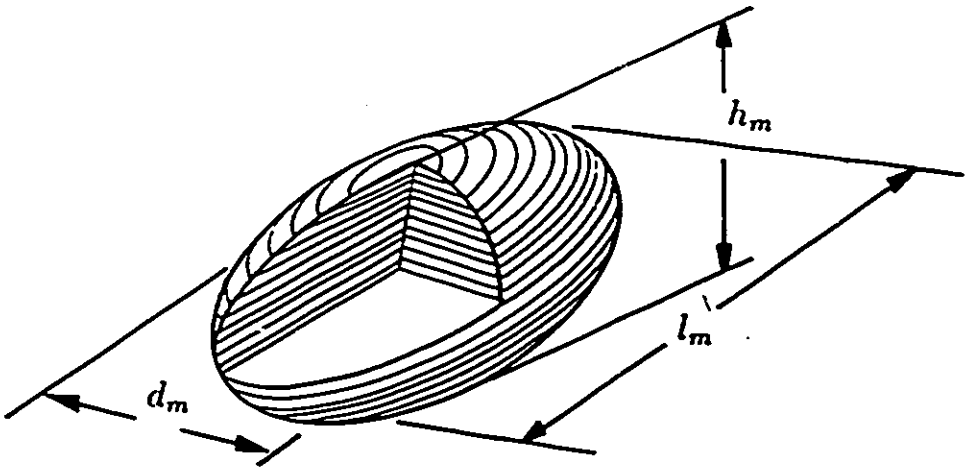

Figure 21: Probe volume.

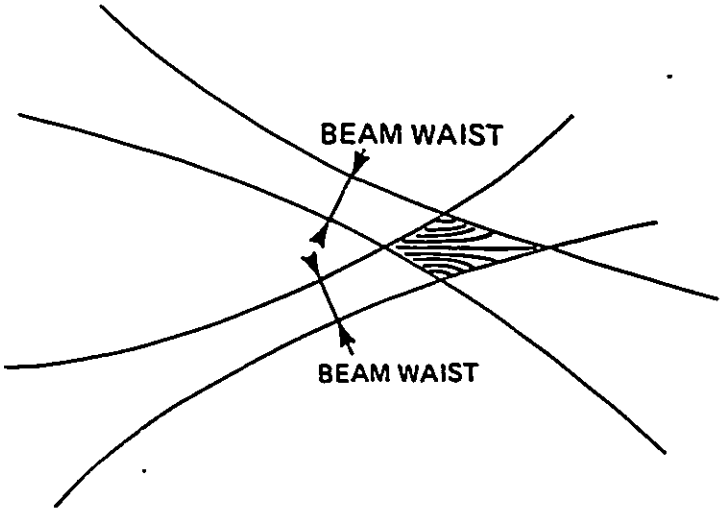

Figure 22: Imperfect beam intersection.

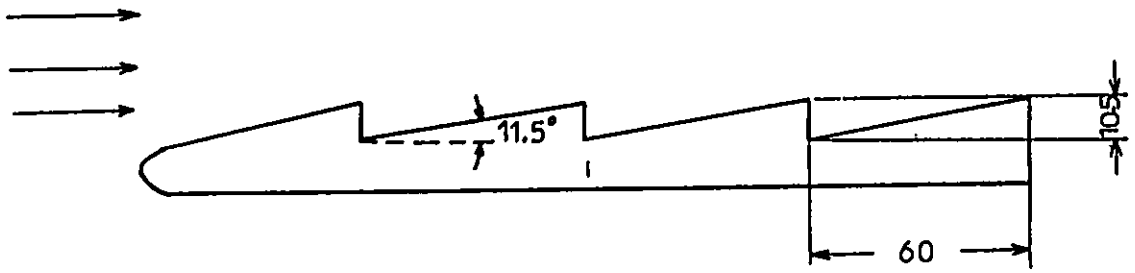

Figure 23: Sketch of experimental model for scales on butterfly's wing.

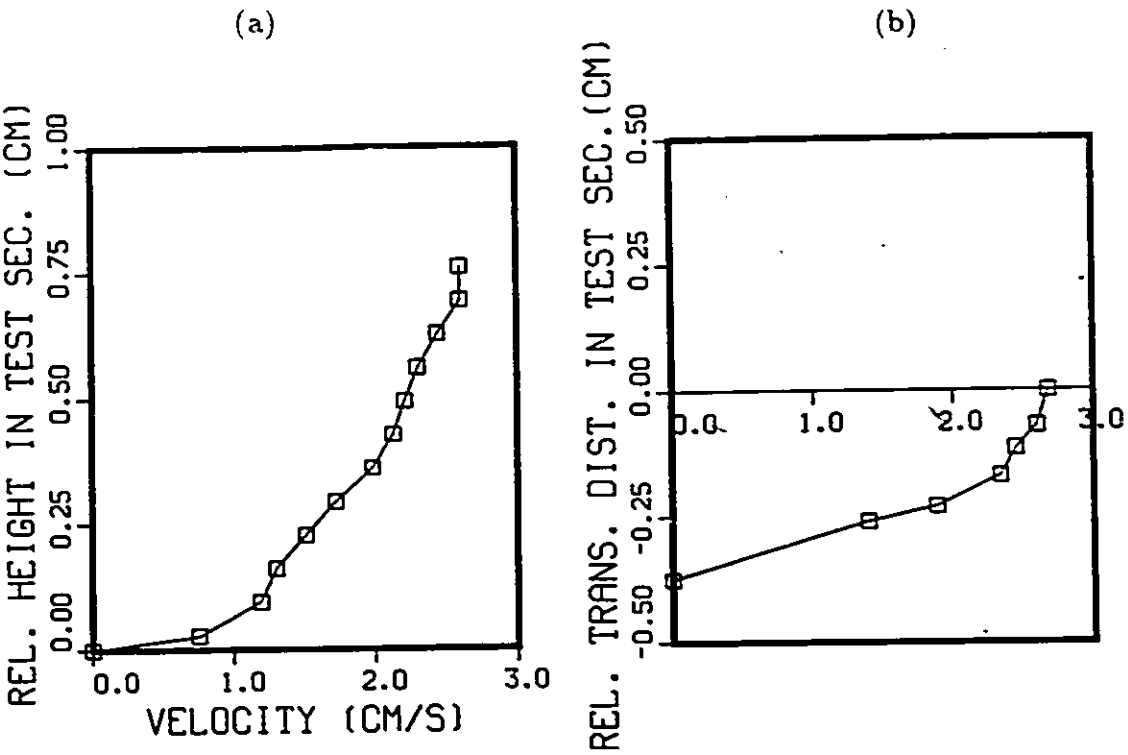

Figure 24: (a)-Vertical velocity profile inside test section for glycerine flow. (b)-Transverse velocity profile inside test section for glycerine flow.

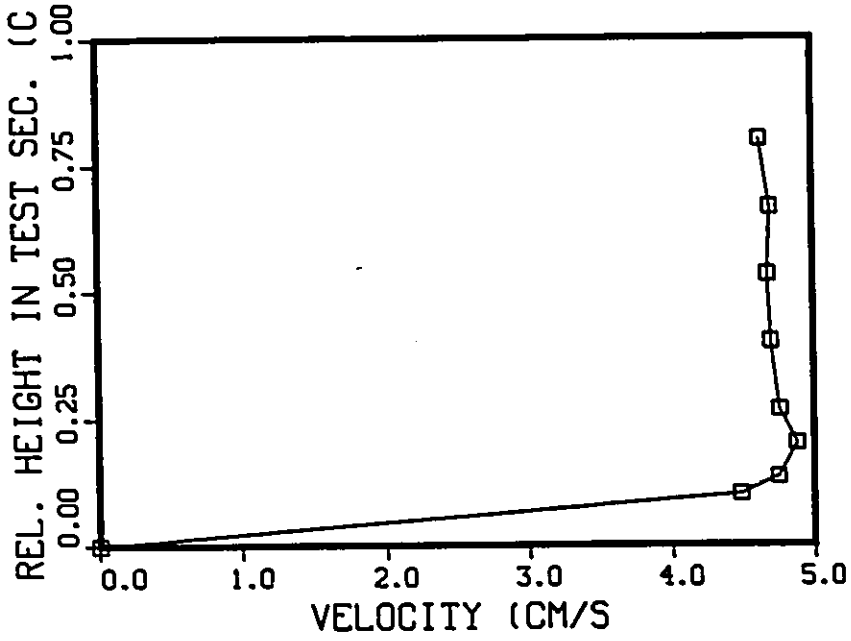

Figure 25: Vertical velocity profile inside test section for water flow.

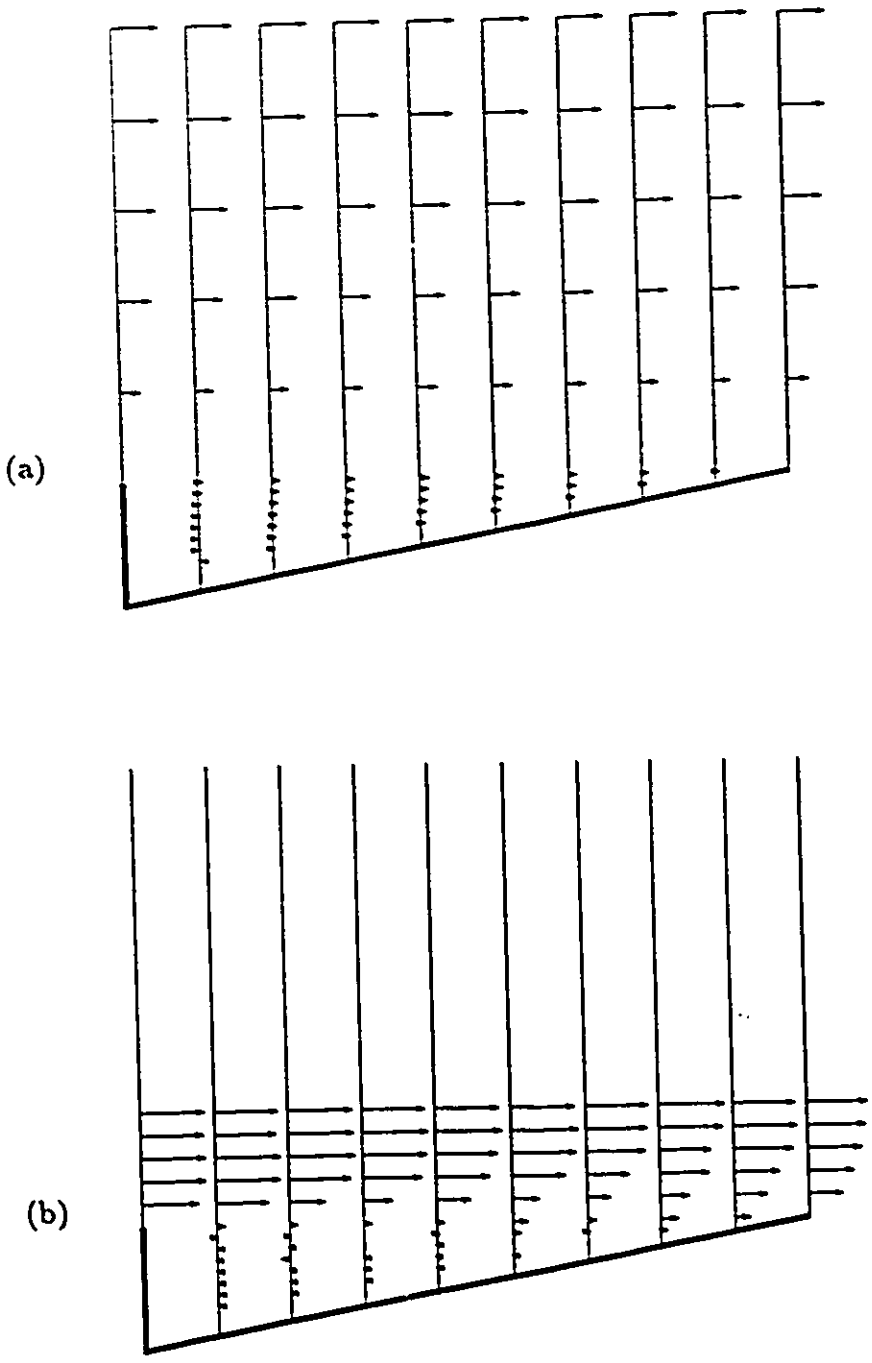

Figure 26: Horizontal velocity vectors for cavity 1. (a)-Re=0.62. (b)-Re=624.

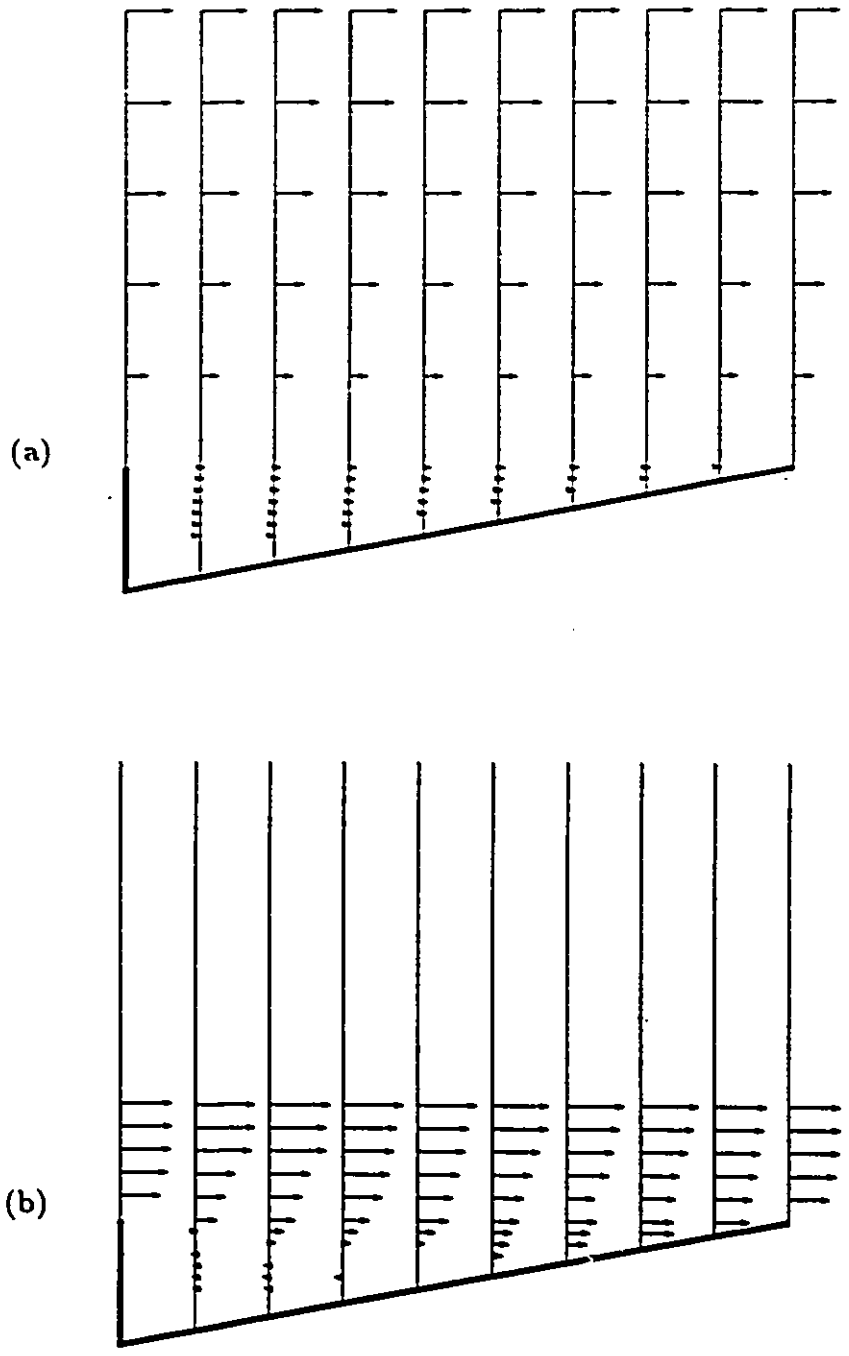

Figure 27: Horizontal velocity vectors for cavity 2. (a)-Re=0.62. (b)-Re=624.

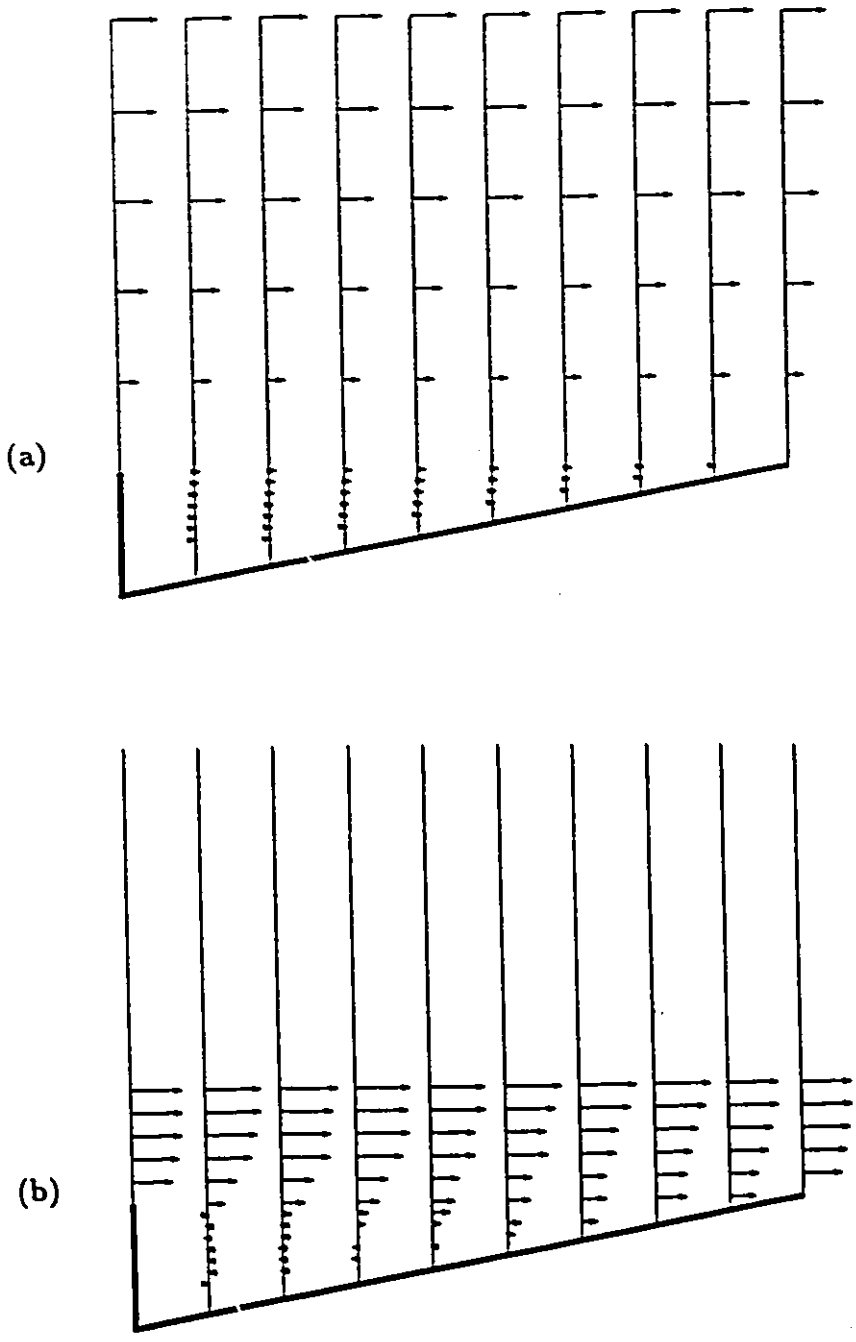

Figure 28: Horizontal velocity vectors for cavity 3. (a)-Re=0.62. (b)-Re=624.

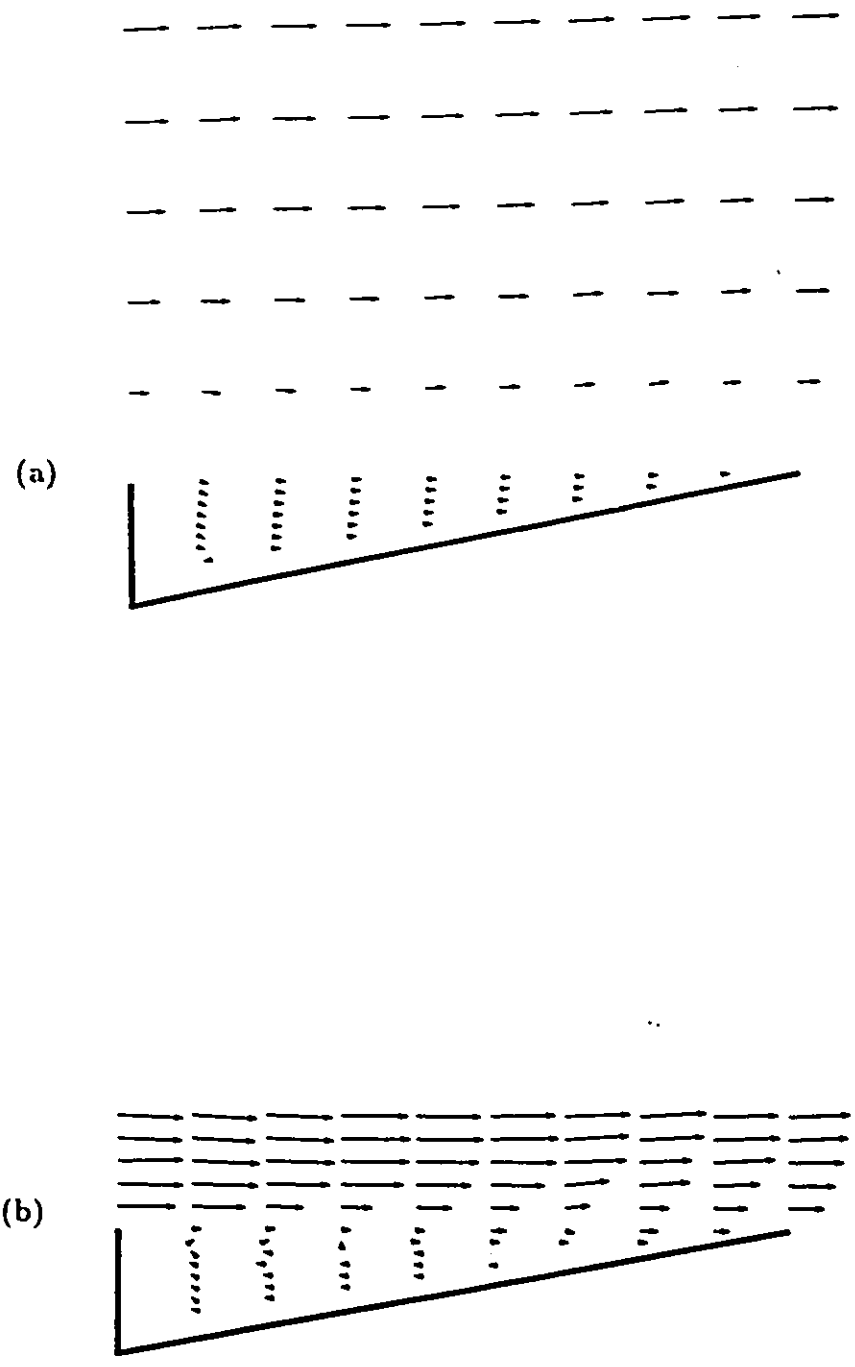

Figure 29: Total velocity vectors inside and above cavity 1. (a)-Re=0.62. (b)-Re=624.

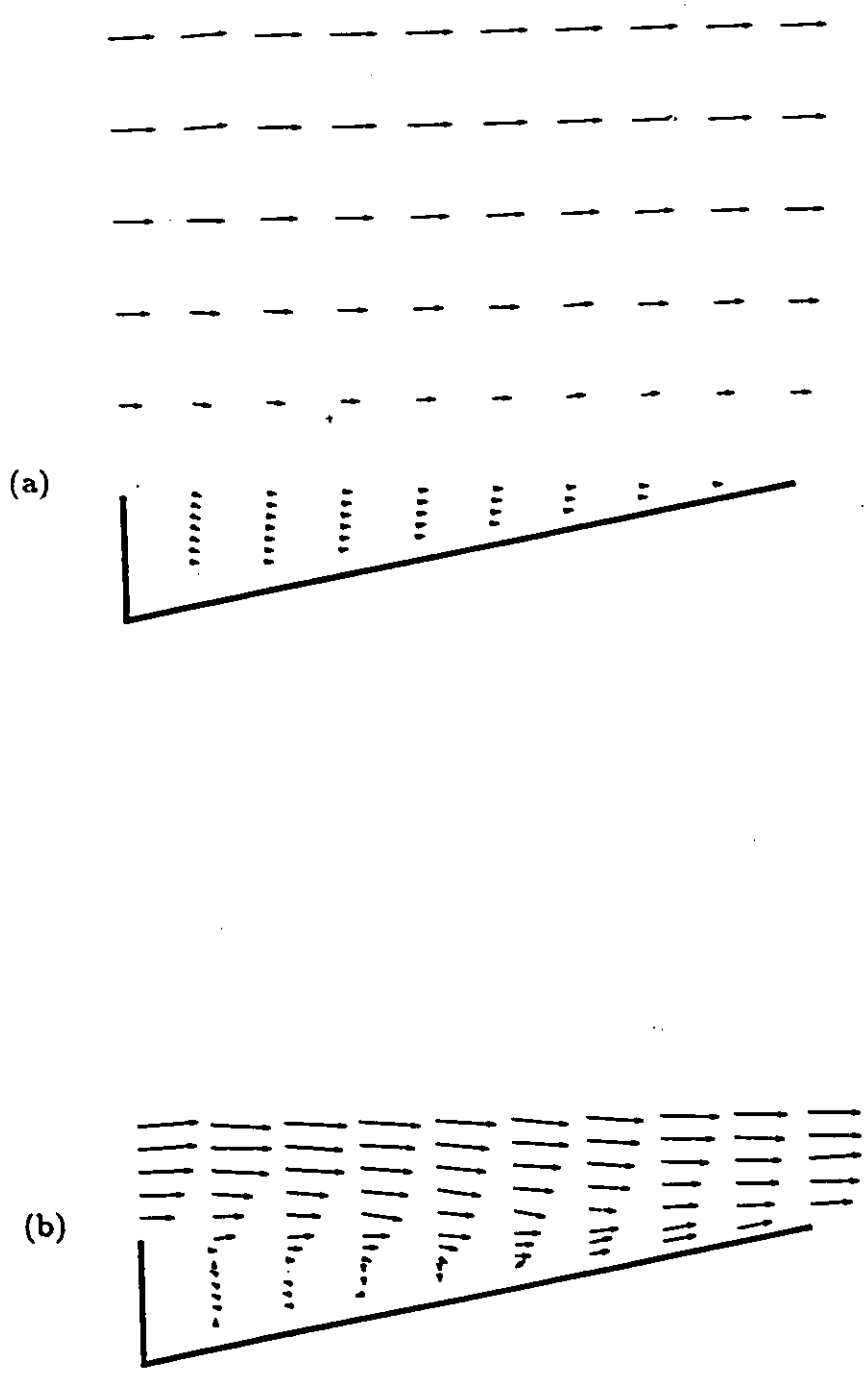

Figure 30: Total velocity vectors inside and above cavity 2. (a)-Re=0.62. (b)-Re=624.

(a)

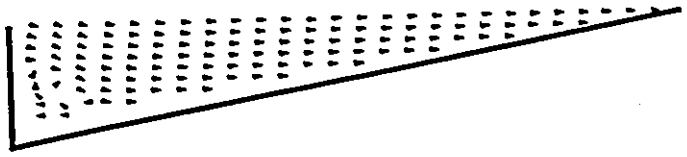

(b)

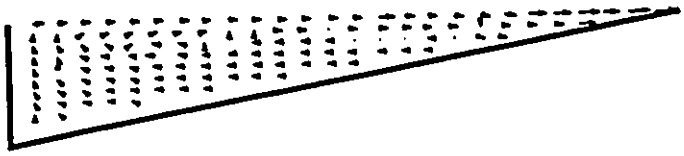

Figure 31: Detailed flow inside cavity 1. (a)-Re=0.62. (b)-Re=624.

(a)

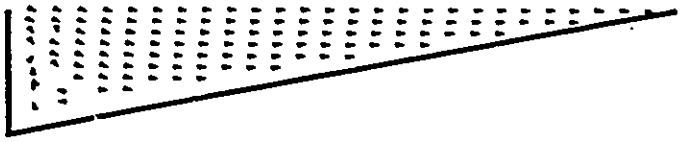

(b)

Figure 32: Detailed flow inside cavity 2. (a)-Re=0.62. (b)-Re=624.

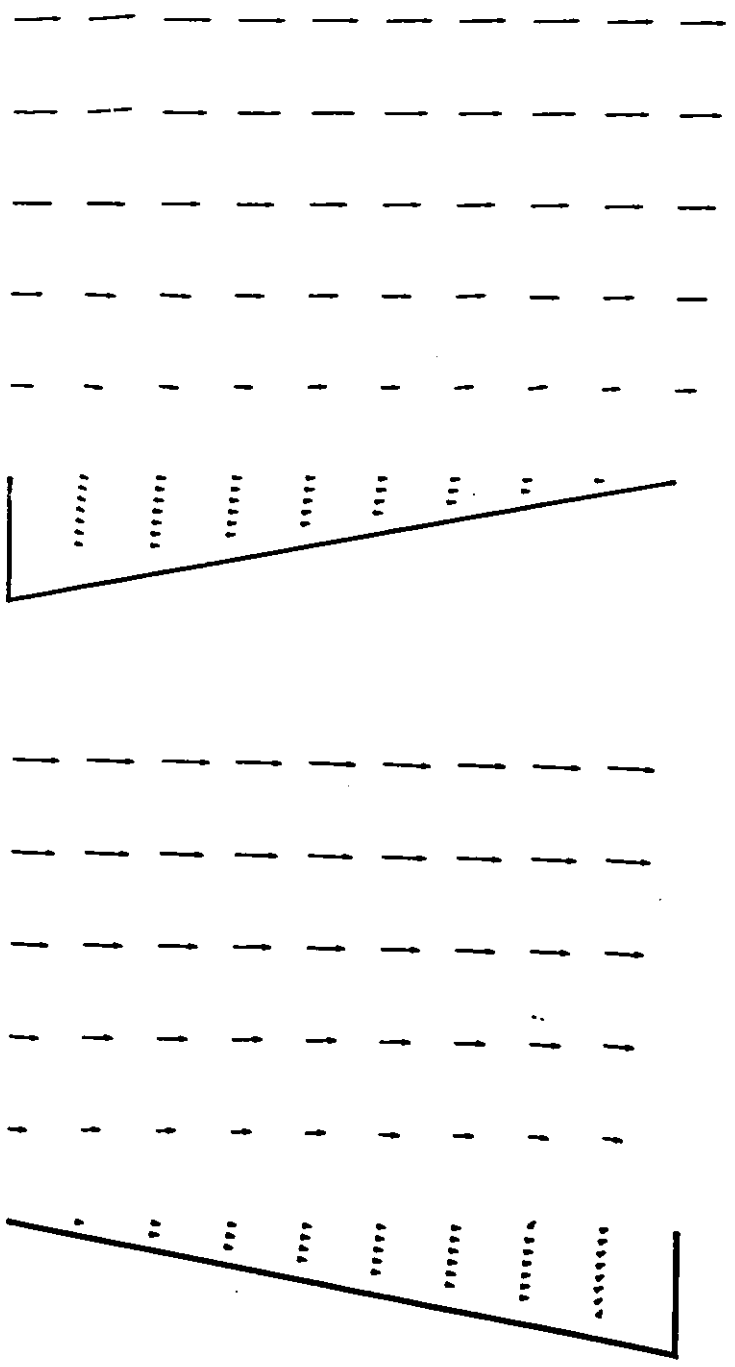

Figure 33: Reversibility of the flow. Total velocity vectors inside and above cavity 1 for both directions of the flow with respect to the cavity at Re=0.6.

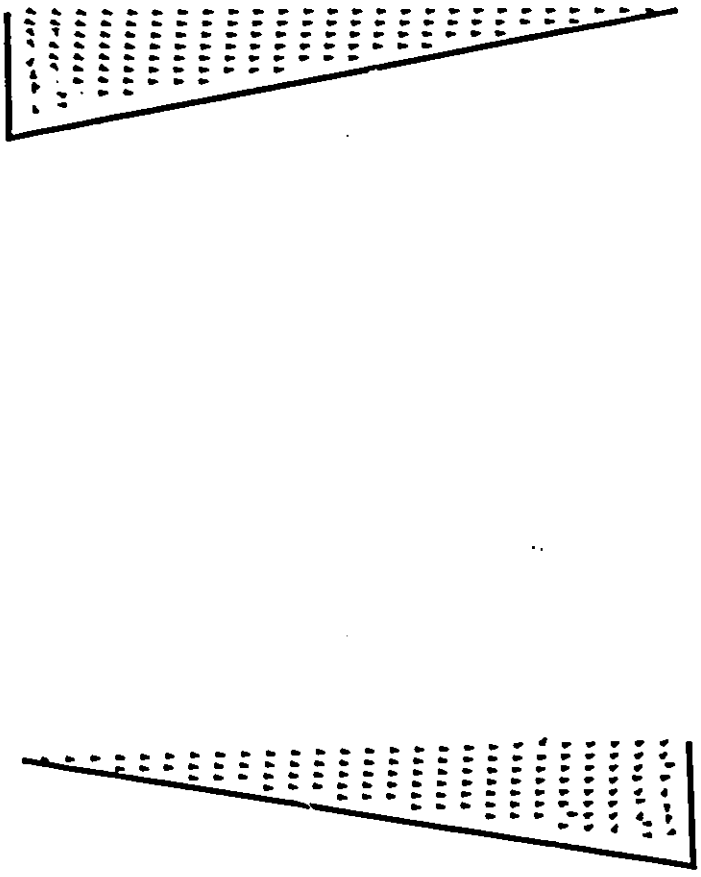

Figure 34: Reversibility of the flow. Detailed flow inside cavity 2 for both directions of the flow with respect to the cavity at Re=0.6.

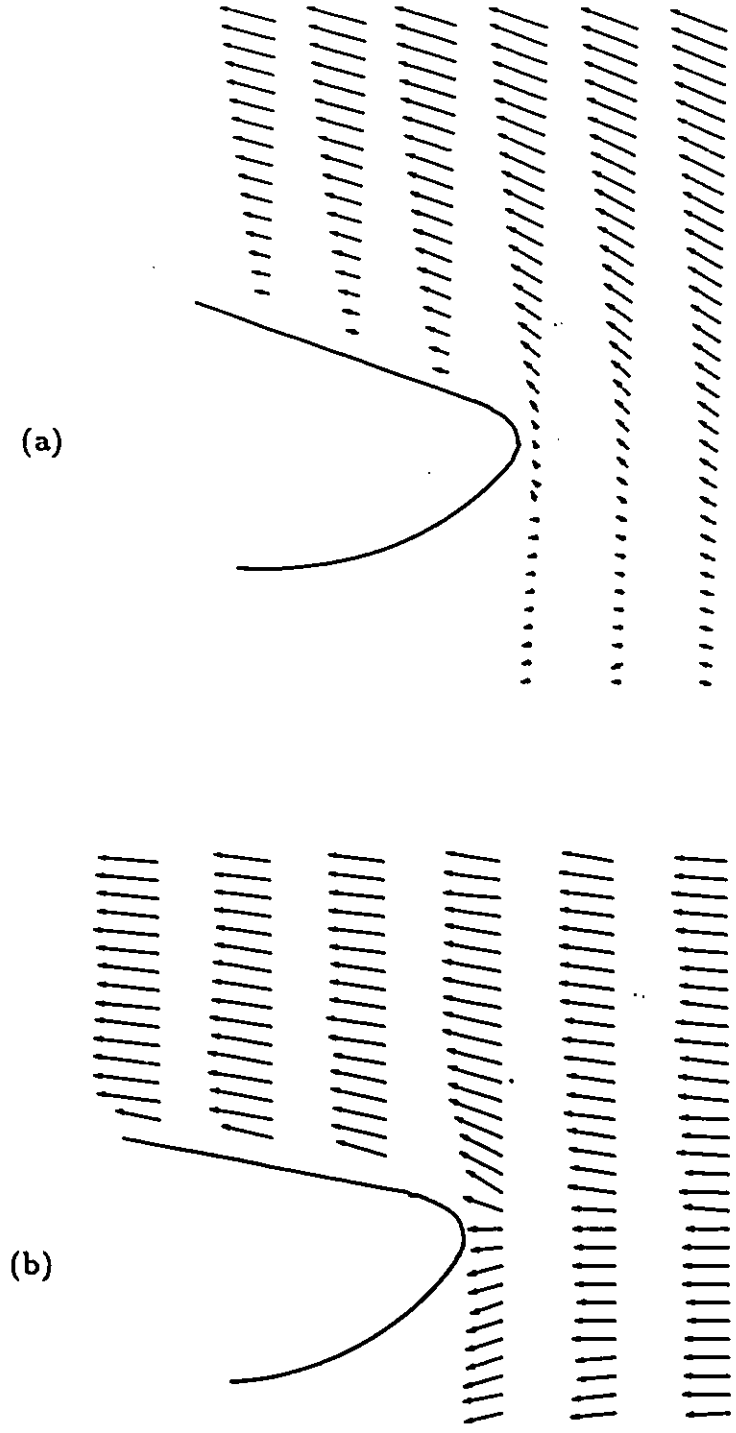

Figure 35: Flow around leading edge. (a)-Re=0.62. (b)-Re=624.

(a)

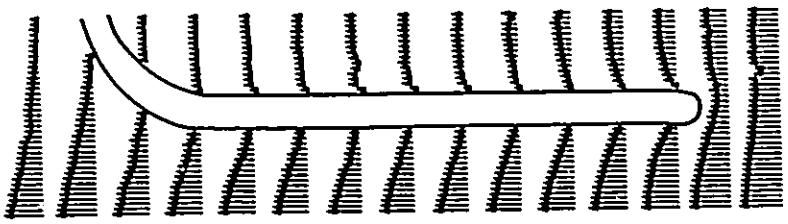

(b)

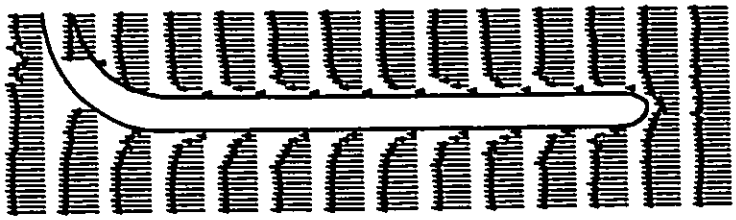

Figure 36: Horizontal velocity vectors for pitot tube 2. (a)-Re=0.124. (b)-Re=171.

(a)

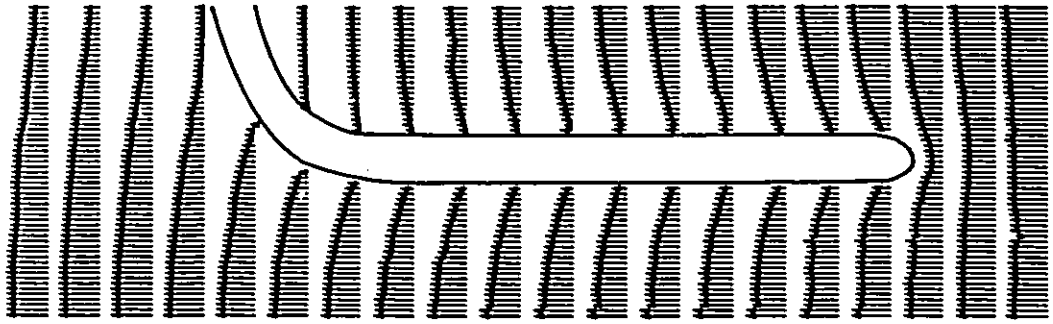

(b)

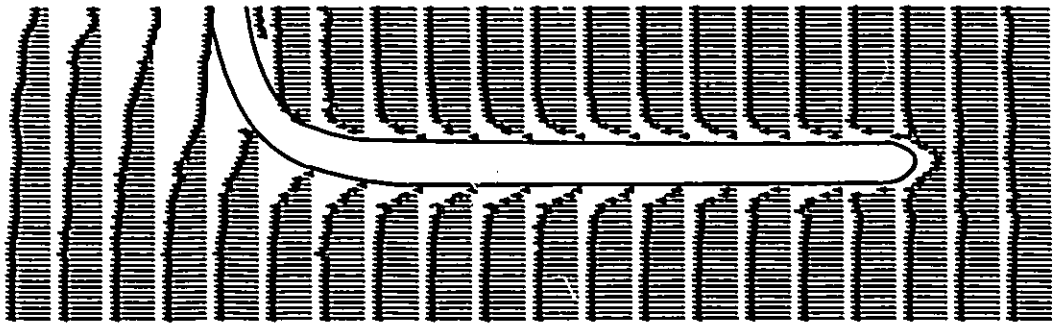

Figure 37: Horizontal velocity vectors for pitot tube 3. (a)-Re=0.147. (b)-Re=220.

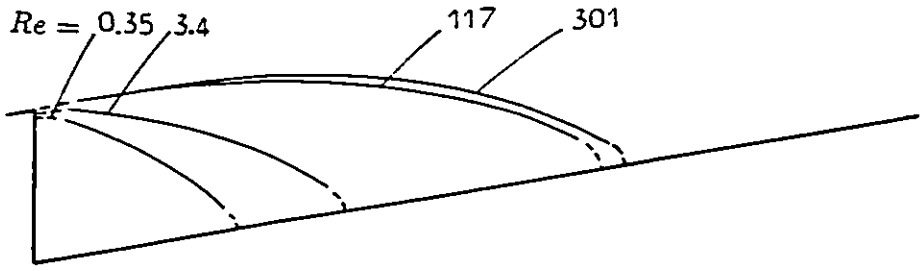

Figure 38: Separation streamlines for different Reynolds numbers.

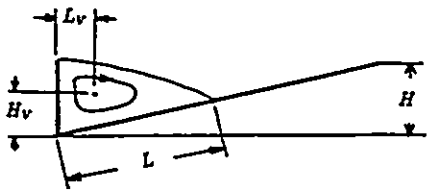

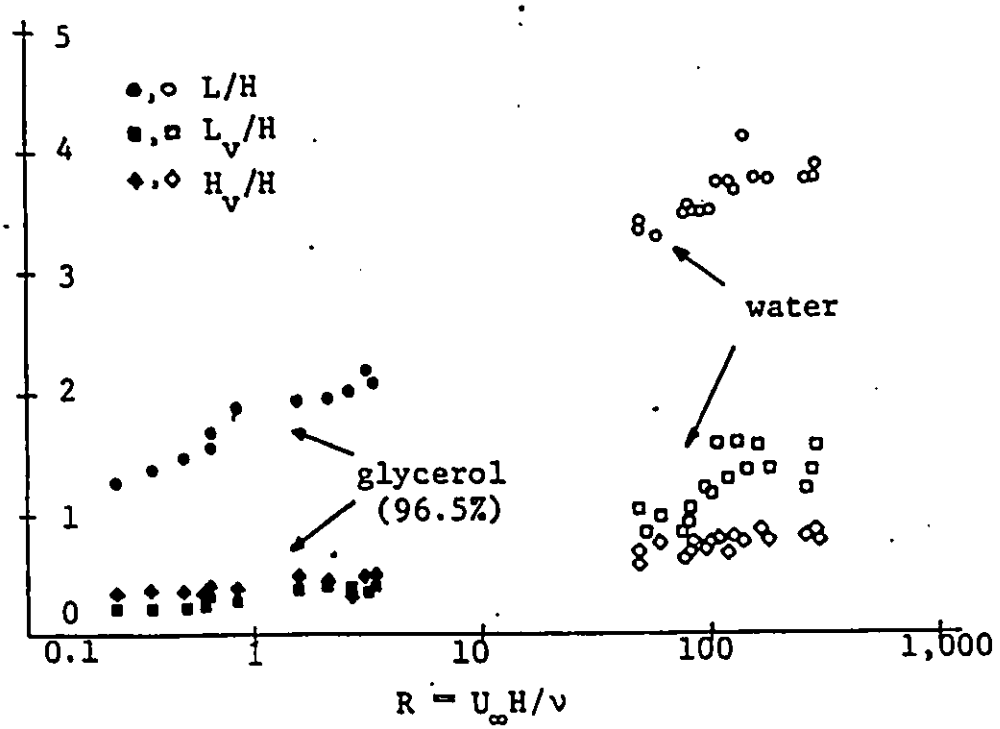

Figure 39: Variation of the reattachment point and vortex center locations vs Re. (From Tavoularis et al., 1985).

Figure 40: Separation streamlines for different angles of attack; Re=0.62.

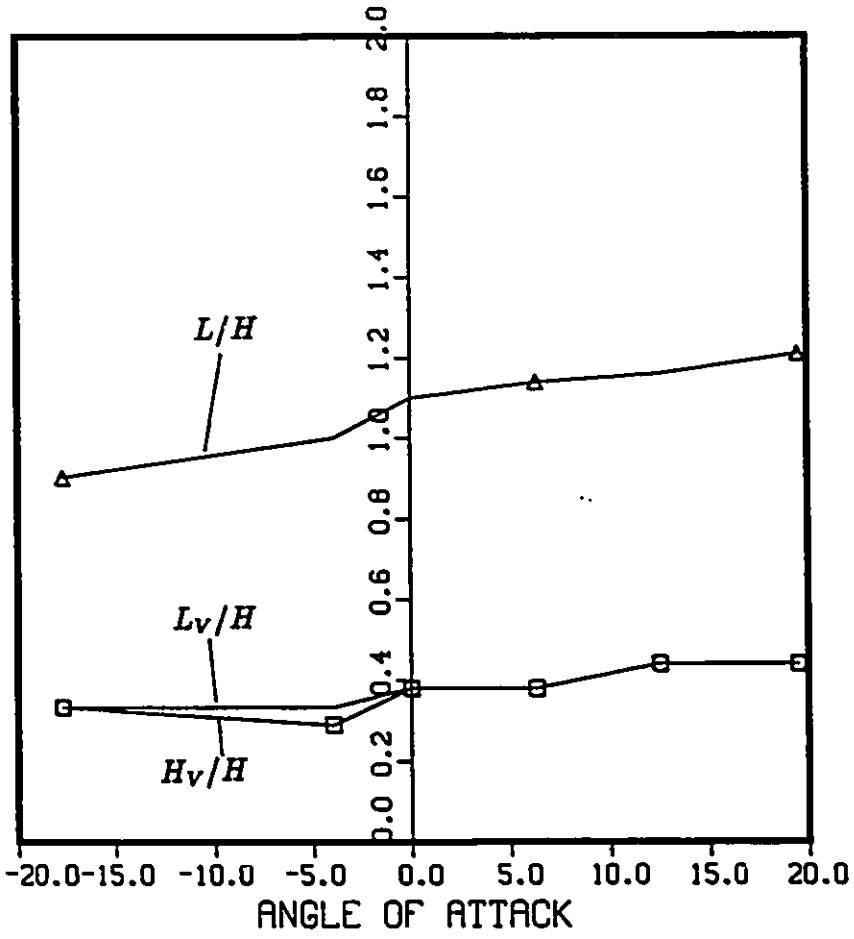

Figure 41: Variation of reattachment point and vortex center locations vs angle of attack.

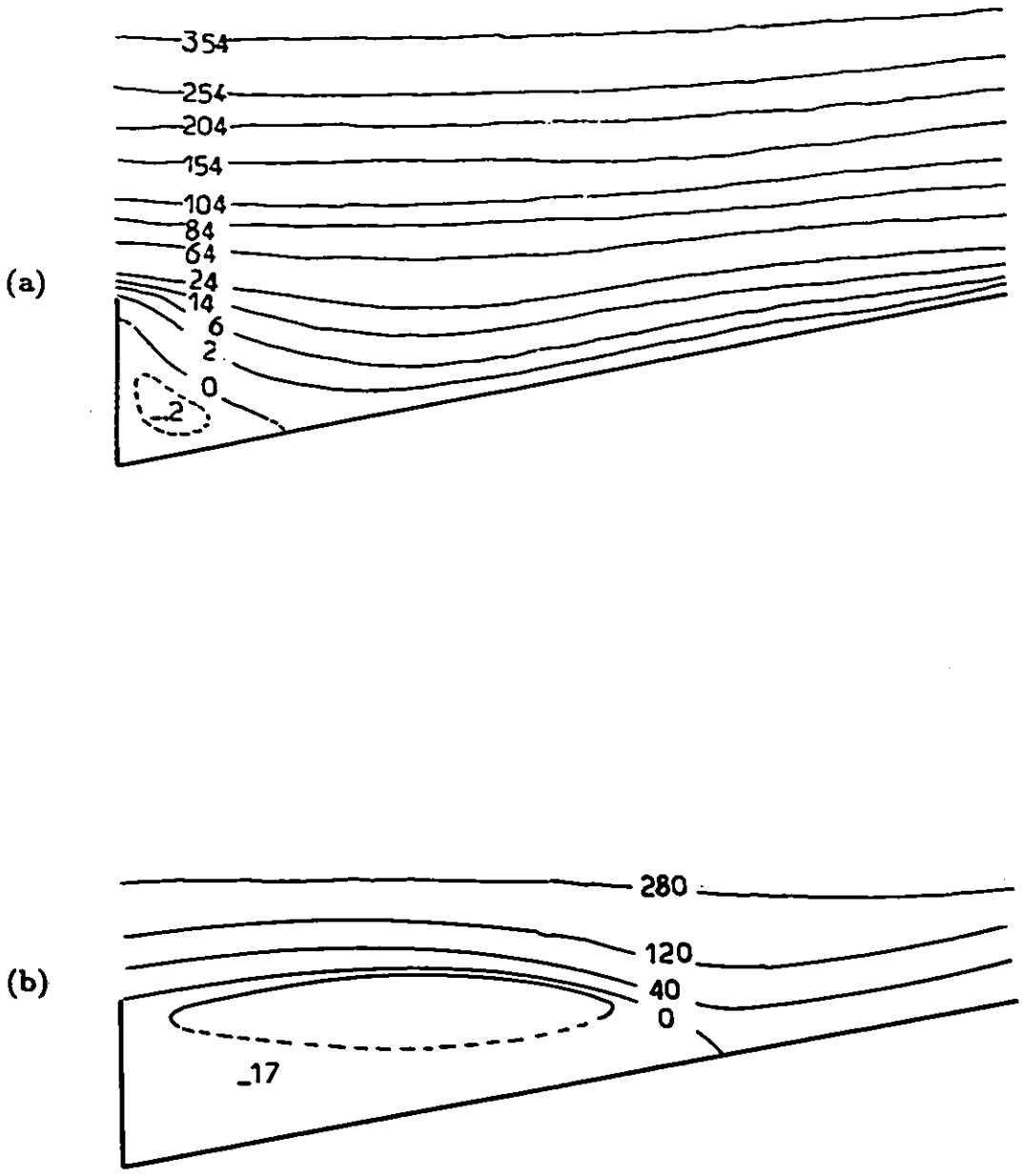

Figure 42: Streamlines for the flow over cavities. (a)- Re=0.62. (b)-Re=624.

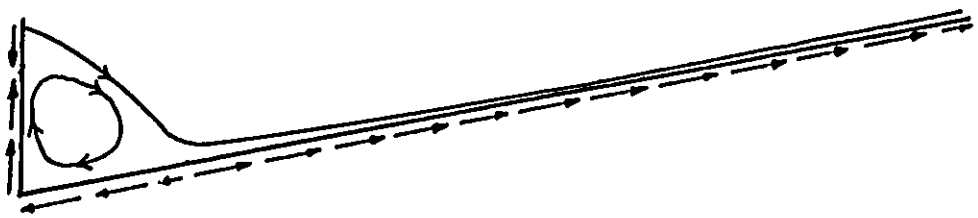

Figure 43: Shear stress distribution on the cavity at low Reynolds number.

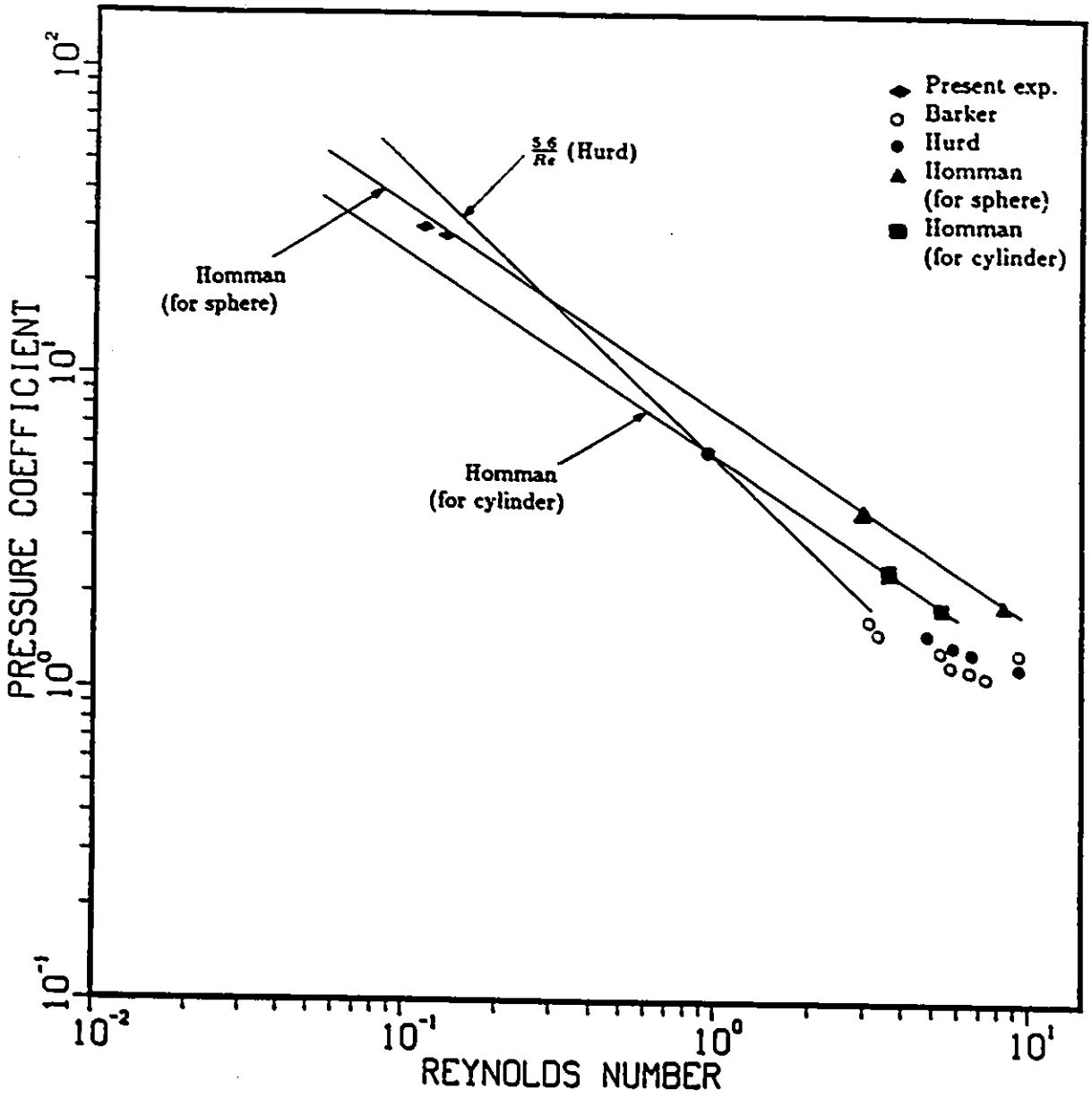

Figure 44: Variation of the pressure coefficient with the Reynolds number.

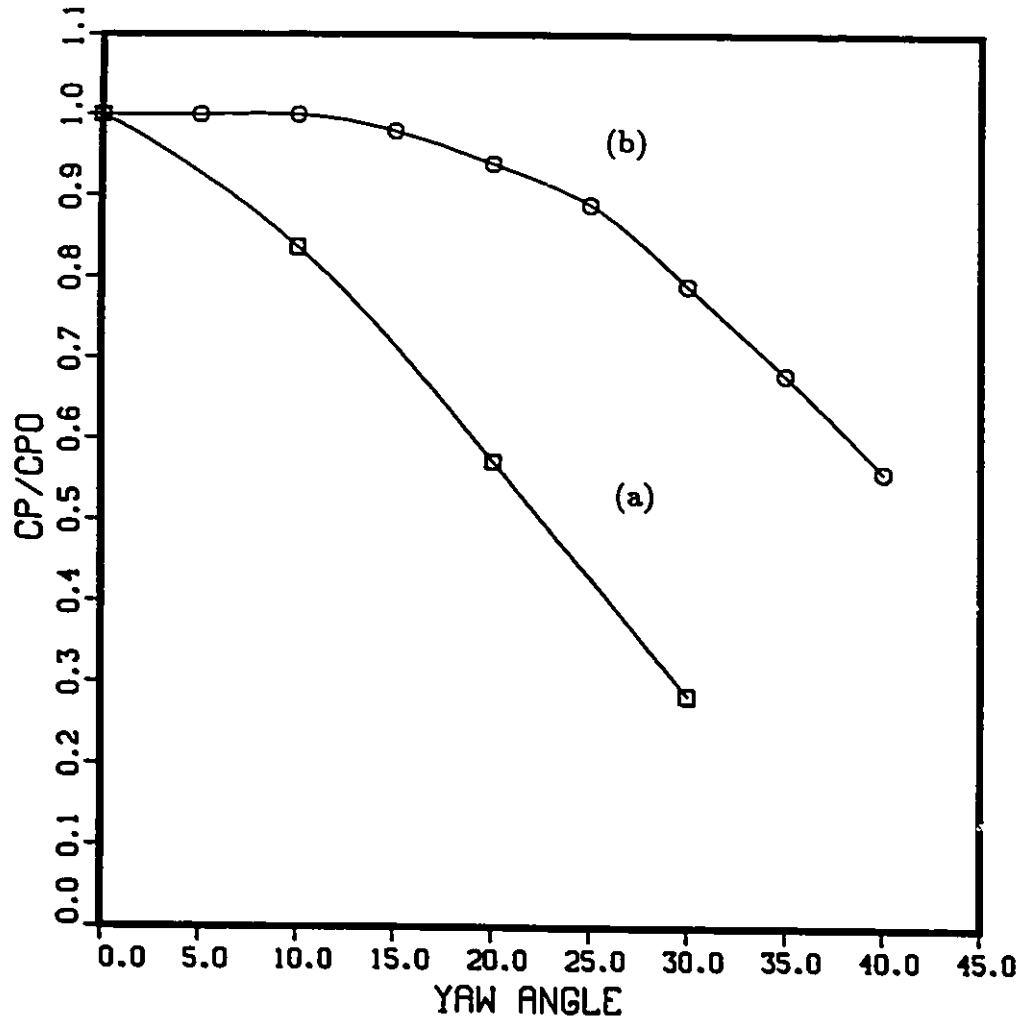

Figure 45: Variation of the pressure coefficient with yaw. (a)-Re=0.124. (b)-Re=4440.

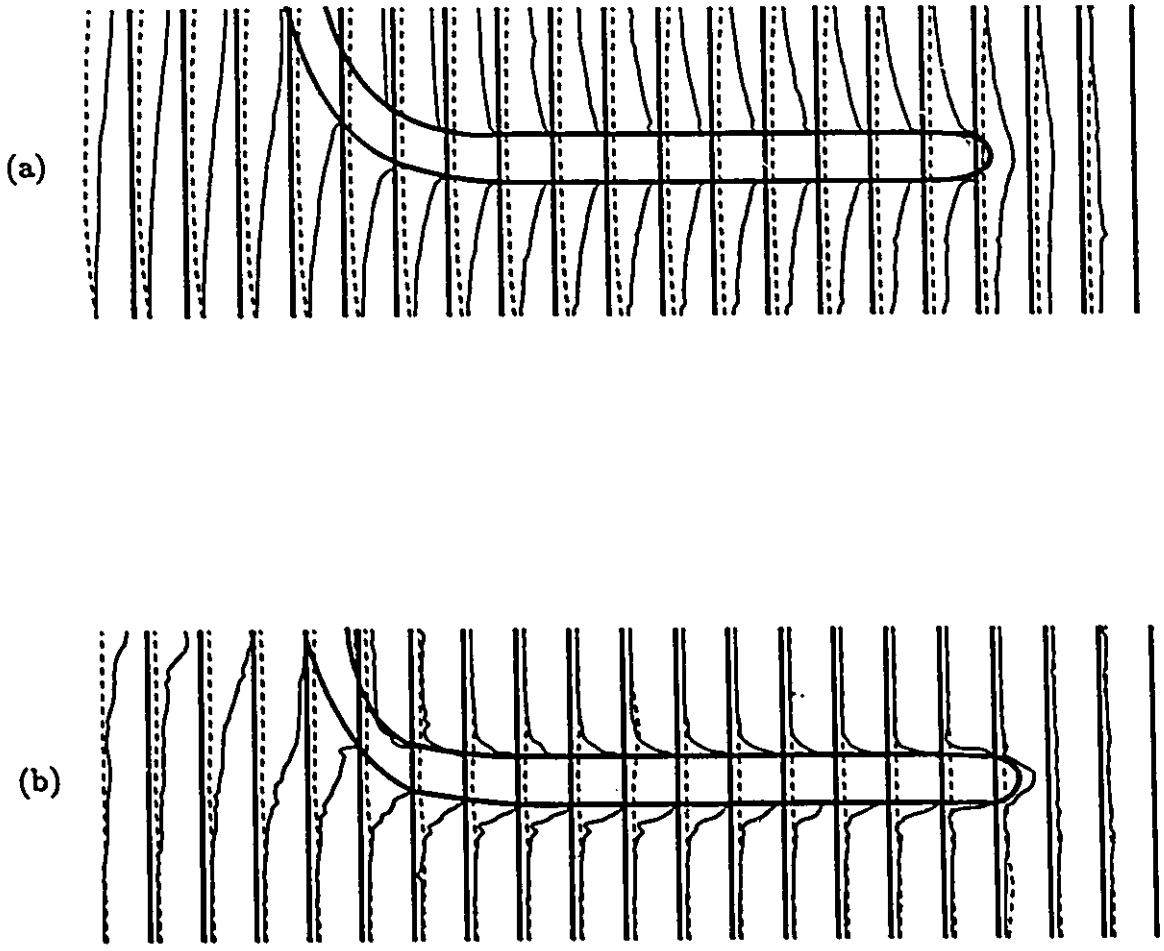

Figure 46: Disturbance of the flow due to the pitot tube insertion. (a)-Re=0.147. (b)-Re=220.

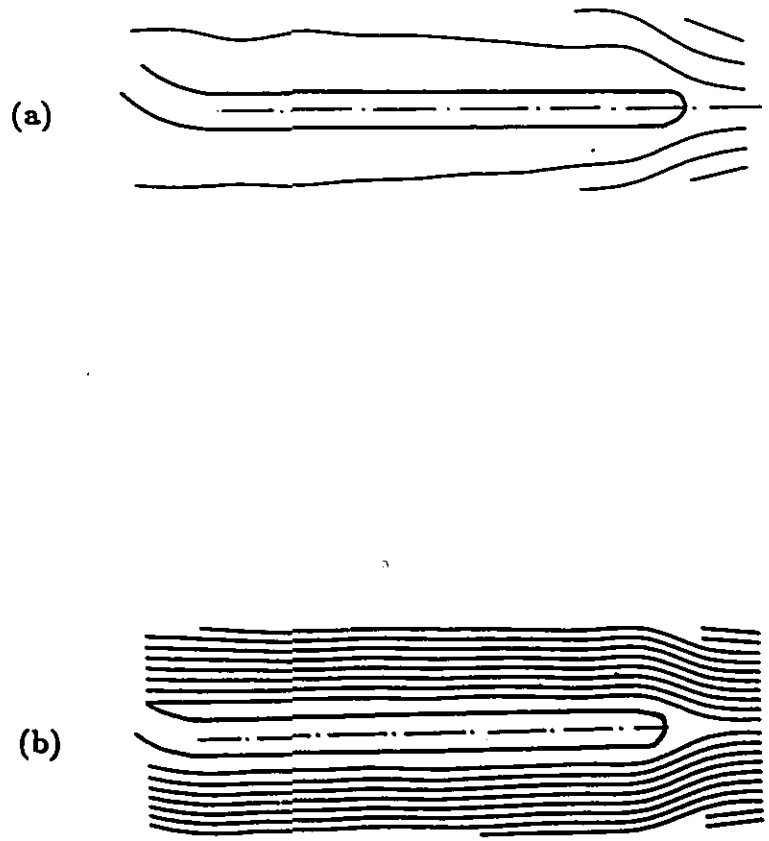

Figure 47: Streamlines for pitot tube 2. (a)-Re=0.124. (b)-Re=171.

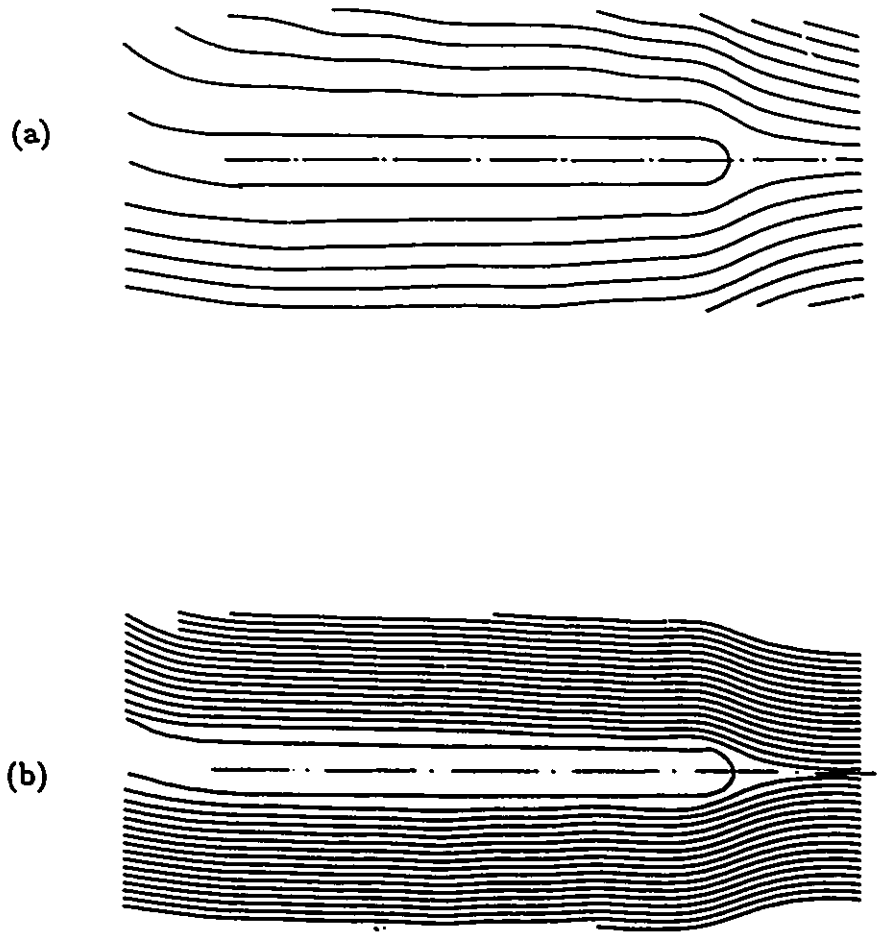

Figure 48: Streamlines for pitot tube 3. (a)-Re=0.147. (b)-Re=220.

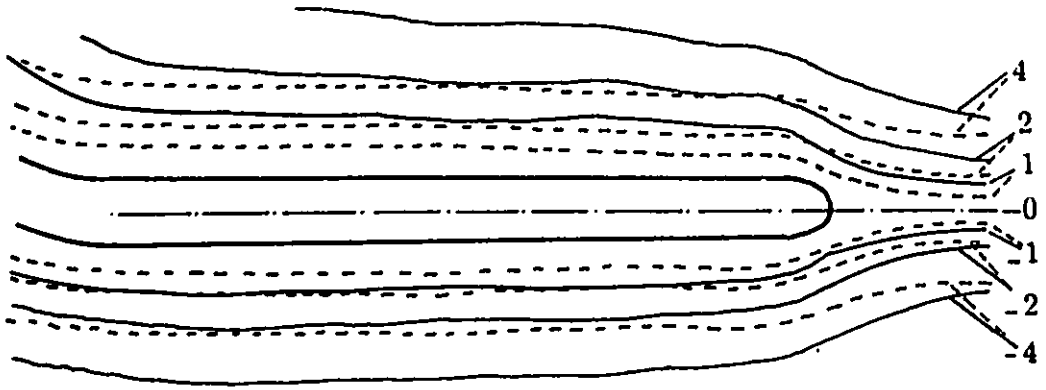

Figure 49: Comparison between streamlines for low and high Reynolds numbers. ___ Re=0.147; - - - Re=220.